The
University
Of
Sheffield.

Department of Mechanical Engineering

Doctor of Philosophy thesis

Effects of Wall Tangential Zero-mass Jets on Turbulent Drag Reduction

---

Author:
Jose Daniel Pérez Muñoz

Supervisors:
Prof. Ning Qin
Dr Pierre Ricco

This thesis is submitted to University of Sheffield in partial fulfilment of the requirement for the degree of Doctor of Philosophy

19th November 2019

To my family

Acknowledgements

Firstly, I would like to thank my supervisor, Professor Ning Qin, for all his support, advice and guidance. His experiences and knowledge helped me a lot, not only at a technical level but also at the way of addressing scientific problems. To my second supervisor, Dr Pierre Ricco, for his ideas and advice. He motivated me towards becoming a better researcher and improve my explanations.

I would like to thank Dr Feng Xie, who worked with me during my first year and helped me a lot. I would also like to thank the friends I made during my PhD, in and out of the office, especially Ian, Sheng, Julian, Samantha, Julián, Verna, Özgün, Alistair and many more.

I want to thank Miguel, who has supported me in the bad times and put up with me in the good ones.

To Coral, for brightening these last two years.

And last, but not least, I thank all the support that my family has given me all these years.

This project is funded by the project DRAGY (Drag Reduction via Turbulent Boundary Layer Flow Control) which is relevant to future large transport aircraft drag/emission reduction for greener aviation and it is part of the European Aerospace Vision 2050 project and the H2020 programme project involving major universities, institutions and aerospace industries in Europe and China.

Abstract

Skin friction drag accounts for 40-45% of the total drag for commercial flights. Drag reduction is one of the aims of the aeronautical industry, as it would increase the efficiency of the aircraft, reduce costs and make the air transportation greener.

The objective of this thesis is to study in detail the technique of the Wall Tangential Zero-Mass Jets (WT-ZMJ) for turbulent boundary layer drag reduction, which is a developing active flow control system. For that, the contributing components of the skin friction drag are identified by means of a novel extension of the method introduced by Fukagata et al. (2002). In this extension, the boundary condition of a jet is introduced and applied to the WT-ZMJ.

The mechanism proposed to operate the jets is studied as well as its power efficiency.

Different configurations and flow control parameters of the WT-ZMJ are explored and further analysed with the extended FIK (FIK-E). This is done to identify the contributions that are affected by each parameter.

The findings show that even though the Reynolds stress contribution increases the skin friction, the inhomogeneous contribution reduces it, which relates to the velocity gradient modification in the flow field.

Moreover, a turbulence model based on the one developed by Spalart and Allmaras (1992) is obtained to explore the potential benefits of WT-ZMJ for practical applications.

Contents

Nomenclature

α	Angle of attack
β	Jet incidence angle
$\mathbf{\Gamma}$	Preconditioning matrix
$\boldsymbol{F}$	Inviscid flux vector
$\boldsymbol{f}_m$	Mass forces
$\boldsymbol{G}$	Viscous flux
$\boldsymbol{Q}$	Primitive variables vector
$\boldsymbol{U}$	Variable vector
$\boldsymbol{v}$	Velocity vector
δ_{jet}	Height from the jet wall to the top of the jet
δ_{step}	Height from the jet wall to the step wall
δ_{ij}	Kronecker delta
κ	Von Kármán constant
κ_x	Streamwise wavenumber
κ_T	Thermal conductivity
λ	Eigenvalue
μ^*	Dynamic viscosity

ν^*	Kinematic viscosity
ω	Frequency of oscillation, $\omega = \frac{2\pi}{f}$
$\overline{\overline{\tau}}$	Friction forces tensor
ψ	Symbol used to represent a generic variable
ρ^*	Density
Σ_c	Surface boundary of a control volume V_c
τ_w^*	Wall friction force per unit area
c	Speed of sound
c_f	Friction coefficient
E	Energy
e	Internal energy
H	Enthalpy
h	Half-channel height
L_{jet}	Jet wall
L_{piston}	Length of the membrane/piston wall
L_{step}	Step wall
L_x^+	Normalized x length of the computational domain of the channel
L_y^+	Normalized y length of the channel
L_z^+	Normalized z length of the computational domain of the channel
M	Mach number
p	Pressure
Q_c	Heat release due to chemical reaction

Q_r	Heat release due to radiation
Re	Reynolds number
T	Temperature
t	Time
T_{osc}	Oscillation period
u_b^*	Bulk velocity
u_τ^*	Wall friction velocity or friction velocity
u^+	Velocity in wall units
$U_{\text{jet,max}}^*$	Maximum jet injection velocity
V_c	Control volume
y^+	Y coordinate in wall units
AFC	Active Flow Control
AGI	Airbus Group Innovations
CFD	Computational Fluid Dynamics
DES	Detached Eddie Simulations
DFT	Discrete Fourier Transform
DNS	Direct Numerical Simulations
DTS	Dual Time Step
FIK	Fukagata-Iwamoto-Kagasi original method
FIK-E	Extension of FIK proposed in this thesis
FIK-PS	Peet and Sagaut extension of the FIK method
FVM	Finite Volume Method

HW	Hot Wire
ISA	International Standard Atmosphere
LES	Large Eddy Simulations
MUSCL	Monotonic Upstream-Centered Scheme for Conservation Laws
PFC	Passive Flow Control
PIV	Particle Image Velocimetry
PSD	Power Spectral Density
RANS	Reynolds-Averaged Navier Stokes
RK	Runge-Kutta
S–A	Spalart–Allmaras Turbulence model
TBL	Turbulent Boundary Layer
TGV	Taylor-Green Vortex
WT-ZMJ	Wall Tangential Zero-Mass Jets
ZMJ	Shorter version of WT-ZMJ

List of Figures

List of Tables

Chapter 1

Introduction

> *"I learned very early the difference between knowing the name of something and knowing something"*
>
> - Richard Feynman, theoretical physicist

1.1 Motivation

In fluid mechanics, drag is the reaction force opposed to the movement of a body. Drag can be classified into four components:

Skin friction drag. This type of drag is present due to the friction of the fluid against the surface or skin of the body. As the air molecules flow past each other and the surface, i.e. shear stress, the viscous resistance opposes to forward motion. This viscosity acts tangentially on the surface of the body.

Pressure drag. This kind of drag depends on the object shape and acts normal to the surface. For aerodynamics applications, it is usually referred to as the pressure force component acting in the direction of the path. Pressure drag and skin friction drag are accounted together to form the *profile drag.*

Induced drag. When a 3D object is immersed in a flow field, 3D effects appear. One of the consequences in the case of a wing is the induced drag. The flow near the wing tips tends to curl around the tips due to the pressure difference, creating vortices that induce a

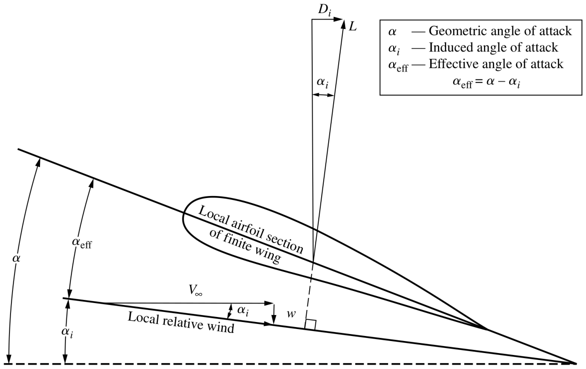

Figure 1.1: Effect of downwash on the local flow over a section of a finite wing. Source: Anderson (2007).

downwards force in the neighbourhood of the wing, called the downwash. This can be seen as a reduction in the effective angle of attack as in figure 1.1. Therefore, the lift is slightly tilted, contributing to the streamwise force.

Wave drag. This form of drag appears in the event of a shock wave. When an object moves at a speed near the speed of sound, pressure waves overlap producing high pressure in front of the moving object. This pressure is so pronounced that the concept of the *sound barrier* arose, prior to 1947, due to the belief that aircraft engines would be unable to overcome such pressure.

The objective of this project is to study the reduction of the **skin friction drag** for turbulent boundary layers (TBL), which accounts for a significant percentage of the total drag in aerospace applications (40-45% for commercial aircraft according to Roskam and Lan (1997)). For large aircraft, the Reynolds number is so high that most of the wing and fuselage surfaces are in the turbulent regime, increasing the skin friction drag.

Using flow control techniques (which will be discussed more in detail in section 1.4), Quadrio et al. (2009b) demonstrated that an oscillating wall in the spanwise direction can attenuate skin friction, obtaining a maximum skin friction drag reduction of around 40%. In this project, a new technique is used based on the concepts and results of the oscillating wall, making it more practical, which represents the next step toward application. This technique makes use of Wall Tangential Zero-Mass Jets (WT-ZMJ). It is conjectured that these jets can simulate the effects of the oscillating wall. With this approach, the surface of the aircraft/wing/channel does not move. A mechanism beneath the surface moves, like a piston or membrane, providing the zero-mass jet required for the drag reduction. These jets make the flow in the boundary layer oscillate tangential to the surface with a spanwise and streamwise component.

In order to study the benefits of the use of jets, the flow will be simulated by means of Direct Numerical Simulations (DNS).

This thesis is structured as follows:

- Chapter 1 introduces the topic of the work, basic concepts and gives a literature review to help to understand the importance of the research.
- Chapter 2 summarises the methodologies employed such as discretisation and numerical schemes. In section 2.5, validations of the code are shown to prove the capabilities of the solver. In section 2.7, the reference case with the WT-ZMJ is presented.
- In chapter 3, a novel methodology based on Fukagata et al. (2002) is extended and applied to the case of the jets to obtain the contributions to the skin friction reduction.
- In chapter 4, a power balance of the device that produces the jets and different configurations of the WT-ZMJ are analysed with the methodology derived in chapter 3.
- In chapter 5, the WT-ZMJ are modelled with a turbulence model as a proof of concept.
- Finally, in chapter 6, the conclusions of this study are gathered as well as future work of interest to continue to develop this technology.

1.2 Turbulent flow

Turbulence is present in the vast majority of flows, which makes it an interesting feature to understand and to take advantage of. The special characteristics of turbulence can be listed, according to different sources (Sagaut et al. (2006); Pope (2001); Tennekes and Lumley (1972)) as:

- *Unpredictability*: Since turbulent flows are highly non-linear, the change of properties of a single molecule in the fluid/gas has a great impact on the turbulence development, making turbulent flows chaotic. That is why statistical tools are often used to describe turbulence.

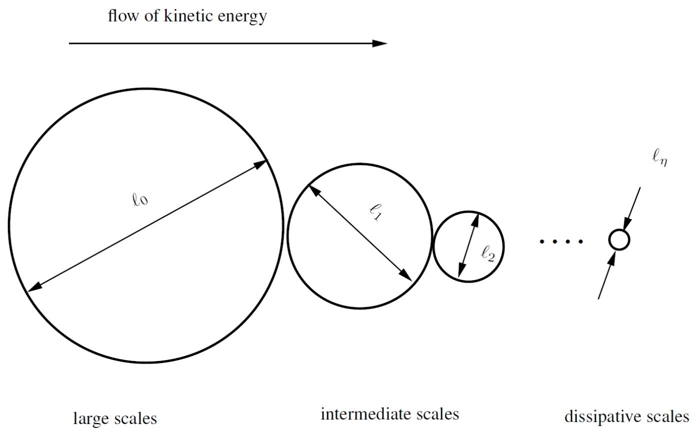

Figure 1.2: Cascade process Davidson (2017).

- *Three-dimensionality*: A turbulent flow cannot be developed if it is constrained in two dimensions. There is no consensus on this matter, but the most popular theory is the impossibility of having vortex stretching, as they increase the rate of mixing and dissipation when two orthogonal vortex collide.

- *Diffusivity*: This is one of the principal characteristics of turbulence. Velocity fluctuations spread strongly in a turbulent flow. Diffusivity enhances mixing, heat and mass transfer.

- *Variety of scales*: Turbulent flows present a wide range of scales, from the scale of the flow geometry, where convection has a larger effect than friction forces, to smaller ones, where viscous stresses overcome convection and dissipate energy into thermal energy. Energy is transferred from large scales to small scales via the cascade process, in which the kinetic energy from large scale eddies is distributed into smaller eddies. A visualisation of this process is sketched in figure 1.2.

- *Continuum*: The flow can still be considered as a continuum because even the small turbulent scales occur at a scale which is much larger than the distance between molecules.

1.3 Wall-bounded turbulent flows

Accurate simulations of flows near aircraft or airfoil are very expensive to perform. That is why this thesis is focused on the channel flow. With this simplification, one can obtain accurate information about the flow phenomena near the wall. The channel flow consists in an infinite space bounded by two walls. The velocity profile develops and it is maintained throughout the entirety of the channel (provided the driving mechanisms are in place), reaching a steady state. In the case of turbulent flow, the quantities are fluctuating at all times. However, it is statistically convergent, i.e. the mean and fluctuations tend to a constant value.

The other wall-bounded turbulent flow is the flow over a plate, or open boundary layer flow, which only features a wall with infinite space on top of the wall. In this case the velocity profile changes downstream, developing what it is called the boundary layer. The boundary layer is defined as the region where the velocity value goes from the free-stream velocity (99% of its value) to the one of the wall, which satisfies the non-slip condition. In the boundary layer, viscous effects have great effect on the flow.

In the case of a channel flow, the viscous effects govern the majority of the flow at low speeds.

One can define[1] the *wall friction velocity* or *friction velocity* as

$$u_\tau^* = \sqrt{\frac{\overline{\tau_w^*}}{\rho^*}} \tag{1.1}$$

where $\overline{\tau_w^*}$ is the spatial and temporal average shear force that the wall experiences due to air friction and ρ^* is the density of the air. The friction force can be calculated as

$$\tau_w^* = \mu^* \left.\frac{\partial u^*}{\partial y^*}\right|_{y=0} \tag{1.2}$$

where μ^* is the dynamic viscosity, u is the velocity in the direction of the force and y is the coordinate perpendicular to the wall. Combining (1.1), (1.2) and the definition of the kinematic viscosity, $\nu^* = \mu^*/\rho^*$, the following dimensionless quantities can be defined:

$$y^+ = \tfrac{y^* u_\tau^*}{\nu^*}; \quad u^+ = \tfrac{u^*}{u_\tau^*}; \quad c_f = \tfrac{2\tau_w^*}{\rho^* u_b^{*2}} \tag{1.3}$$

---

[1] In this project, variables with the superscript ψ^* use metric system units, variables with the superscript ψ^+ are non-dimensionalised with viscous units and variables without superscript are non-dimensionalised with outer variables.

where u_b^* is the bulk velocity, which is the spatial average velocity in the case of a channel flow.

According to several sources (Pope (2001); Schlichting (1979)), the velocity profile for turbulent flows can be divided into different regions. The most important ones are the viscous sublayer $(y^+ < 5)$, the log-law region $(y^+ > 30)$ and the buffer layer $(5 < y^+ < 30)$ where the first two follow closely the following equations.

$$\begin{cases} u^+ = y^+ & \text{if } \; y^+ < 5 \\ u^+ = \frac{1}{\kappa} \ln \, y^+ + C & \text{if } \; y^+ > 30 \end{cases} \tag{1.4}$$

where $\kappa = 0.40 - 0.41$ is the Von Kármán constant and C is a constant that is generally around 5.0–5.2 depending on the source. For channel flows at low Reynolds numbers, according to Kim et al. (1987), it takes a value of 5.5. For the buffer layer, there are a wide range of complex approximations. To have an idea of the kind of approximations for the buffer layer, the one provided by Gersten and Herwig (1992) is

$$u^+ = \frac{1}{\Lambda}\left[\frac{1}{3}\ln\frac{\Lambda y^+ + 1}{\sqrt{(\Lambda y^+)^2 - \Lambda y^+ + 1}} + \frac{1}{\sqrt{3}}\left(\arctan\frac{2\Lambda y^+ - 1}{\sqrt{3}} + \frac{\pi}{6}\right)\right] + \frac{1}{4\kappa} ln \left(1 + \kappa B y^{+4}\right) \tag{1.5}$$

where $B = 1.43 \times 10^{-3}$ and $\Lambda = 0.127$.

1.4 Literature review on turbulent skin friction reduction using passive and active open-loop flow control

Flow control devices can be used to delay separation of the boundary layer, trigger or postpone turbulence in the flow, enhance heat transfer, reduce skin friction, suppress noise, and many other applications (Jahanmiri (2010); Gad-el Hak (2000)).

Flow control devices can be grouped into two categories: Passive Flow Control (PFC) and Active Flow Control (AFC). PFC devices do not require any external energy input to work whereas AFC devices do.

Regarding the actuation of AFC, they can be split into predetermined or interactive AFC devices. If the device is set beforehand and the configuration is not changed during operation or it is changed manually it is considered predetermined, because it is not dependent on the

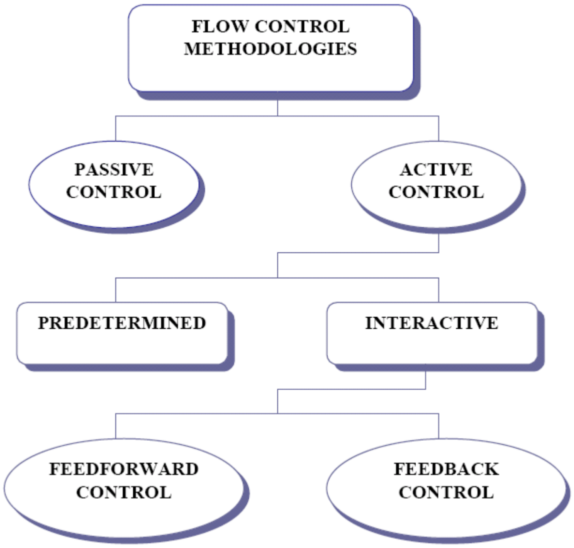

Figure 1.3: Flow control classification. Source: Jahanmiri (2010).

flow field. On the other hand, if the device behaviour is adjusted depending on the information from sensors or other sources it is considered interactive. Finally, interactive AFC devices can be feed-forward control (open loop systems) or feed-back control (closed loop systems). A flowchart of the different types of flow control devices is presented in figure 1.3.

1.4.1 Passive flow control

These devices do not require any kind of energy input to operate. Passive vortex generators and riblets fall into this category. Drag reduction using riblets or micro-textures has been shown to give good results in several fields (Saravi and Cheng (2013)). These devices act mainly in the viscous sublayer and in the buffer layer. Bechert carried out an exhaustive study on the topic as seen in (Bechert and Bertenwerfer (1989); Bechert et al. (1997, 2000)), focusing on what can be found in the nature and making experiments trying to replicate it. The riblets (figure 1.4) can be of different shapes and orientations and they provide around 4% of drag reduction. Under ideal conditions, a 9.9% drag reduction can be achieved as reported in Bechert et al. (1997).

Min and Kim (2004) and Aljallis et al. (2013) achieved flow control without altering the geometry of the wall by applying a coating to the surface. Superhydrophobic surfaces have been proven to obtain skin friction reduction in a wide range of operation, as proven by

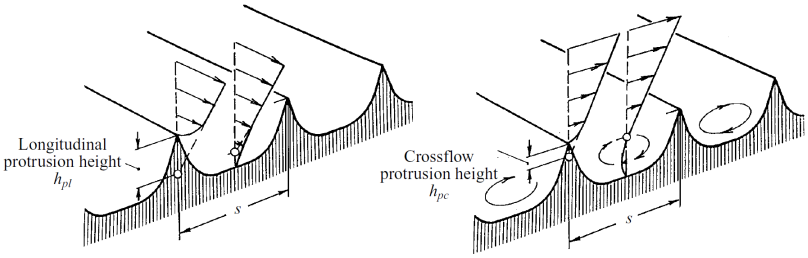

Figure 1.4: Longitudinal and crossflow riblets (Bechert et al. (1997)).

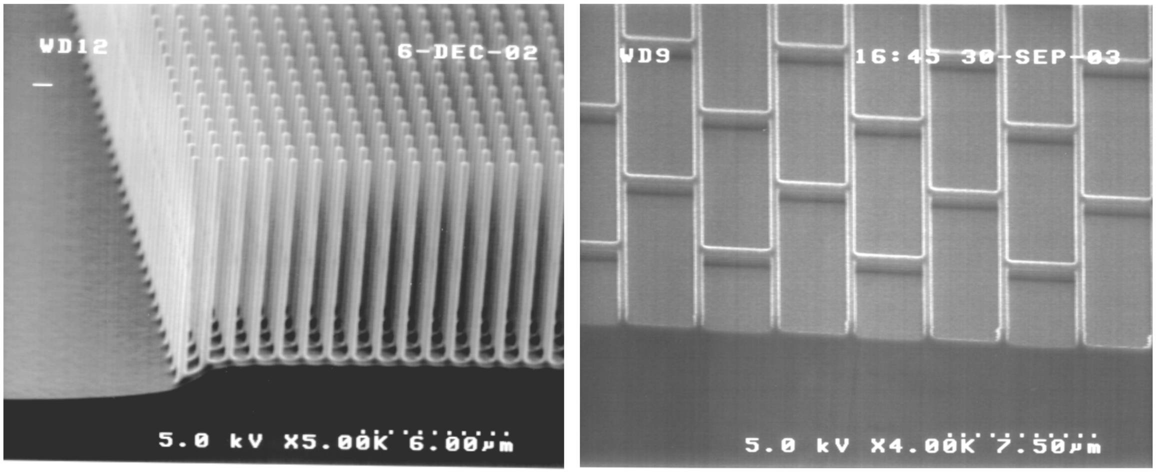

Figure 1.5: Scanning Electron Microscope image of two different superhydrophobic surfaces. Source: Henoch et al. (2006)

Henoch et al. (2006) and Daniello et al. (2009).

1.4.2 Active flow control

Even though passive flow control can achieve drag reduction, it is usually limited by the shape of the device. On the other hand, spending some energy or power on the flow could lead to more options to drag reduction.

One of the ways is by using plasma to affect the flow field. Yao et al. (2018) calculated a reduction of friction coefficient with spanwise jets using plasma actuators, therefore, creating a body forcing to create these *jets*. The flow field generated with this technique can be seen in figure 1.6.

Another way, the one which this thesis is built upon is the wall movement active flow

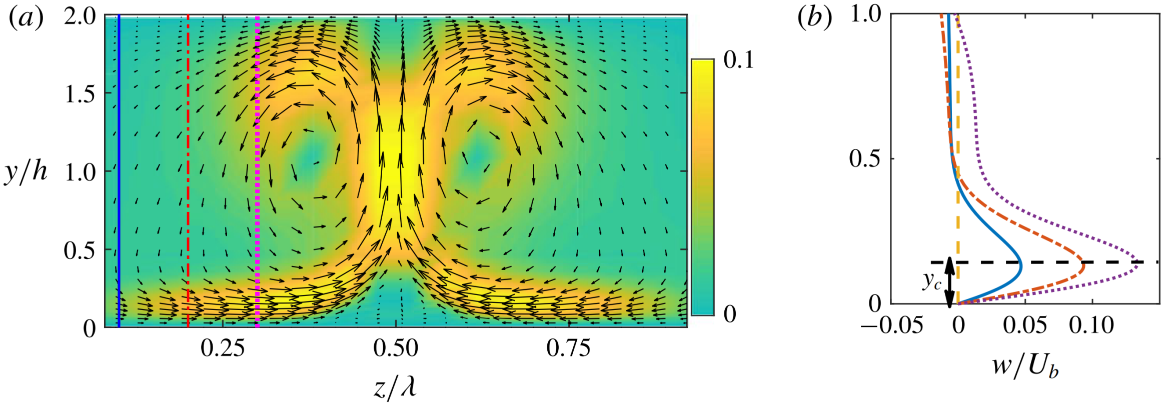

Figure 1.6: (a) Flow field of velocity magnitude at a cross section in the $y - z$ plane. (b) profile of the spanwise velocity at vertical lines of (a). Source: Yao et al. (2018).

control. Wall movement in a channel has been studied to reduce drag in several ways. The main wall movements mechanisms that have been covered are the spanwise oscillating wall, the streamwise travelling waves in a spanwise oscillating wall and the rotating disks.

1.4.2.1 The spanwise oscillating wall

The moving wall mechanism is a type of active flow control that consists in oscillating the wall spanwise to reduce the skin friction. The moving wall problem has been studied through the years. The driven turbulent flow with spanwise moving wall concept was firstly introduced by Jung et al. (1992), based on experimental and numerical studies that suppressed the production of turbulence when subjected to a spanwise pressure gradient (Bradshaw and Pontikos (1985); Driver and Hebbar (1987); Moin et al. (1990)). Experiments by Laadhari et al. (1994) also proved that the moving wall mechanism is valid for the reduction of Reynolds stresses.

Baron and Quadrio (1996) showed that the moving wall is an effective method to have a sustained friction drag reduction at low Reynolds numbers. It seems that the effect of the moving wall movement creates vortices as high as $y^+ \approx 40$ as shown in figure 1.7.

Quadrio and Ricco dedicated several works on this topic. In Quadrio and Ricco (2003), the response due to sudden spanwise oscillations of the walls is studied for different oscillating periods. Later, in Quadrio and Ricco (2004), the drag reduction of this mechanism is addressed. In Ricco and Quadrio (2008), a parameter S is identified, which relates the drag

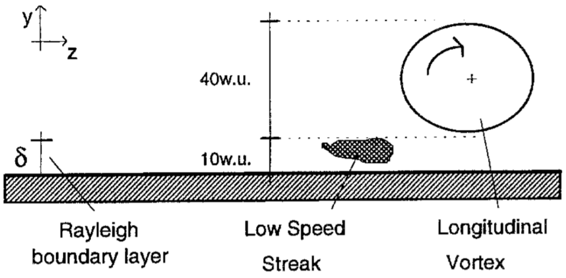

Figure 1.7: Conceptual model of the effect of spanwise oscillations (Baron and Quadrio (1996)).

reduction with both the maximum wall velocity and the period of oscillation. The energy balance and turbulence dissipation was studied more in detail in Ricco et al. (2012).

1.4.2.2 Streamwise travelling waves

Quadrio et al. (2009b) and later Quadrio and Ricco (2011) investigated a modification of the oscillating wall. Using streamwise travelling waves tuned by certain parameters, the skin friction drag can be reduced significantly, to around 40% of the original value. Figure 1.8 shows the setting of the streamwise travelling waves. The oscillations depend on time with the frequency of oscillation, ω, and on space with the streamwise wavenumber, κ_x.

In figure 1.9, the power saved with this technique is presented. The different combinations of ω and κ_x lead to different power savings and power consumption. These have to be evaluated together to assess its efficiency. The thick line corresponds to the boundary where the net power is 0 and therefore, all power saved in the forcing of the flow is used entirely by the flow control itself. Inside the boundary, the power saved from drag reduction is higher than the input power to the oscillating wall, which is the objective of these kind of devices.

It is interesting to see how the expenditure on power limits the usefulness of the flow control. A trade off between reduction of drag and power spent has to be taken into account for active flow control systems.

1.4.2.3 Rotating discs

In order to simulate the oscillating wall, Ricco and Hahn (2013) studied the benefits of the use of rotating discs. A maximum drag reduction of 23% was computed and the net power saved was 10%. Later, Wise et al. (2014) studied the complex and unexpected effect of disks

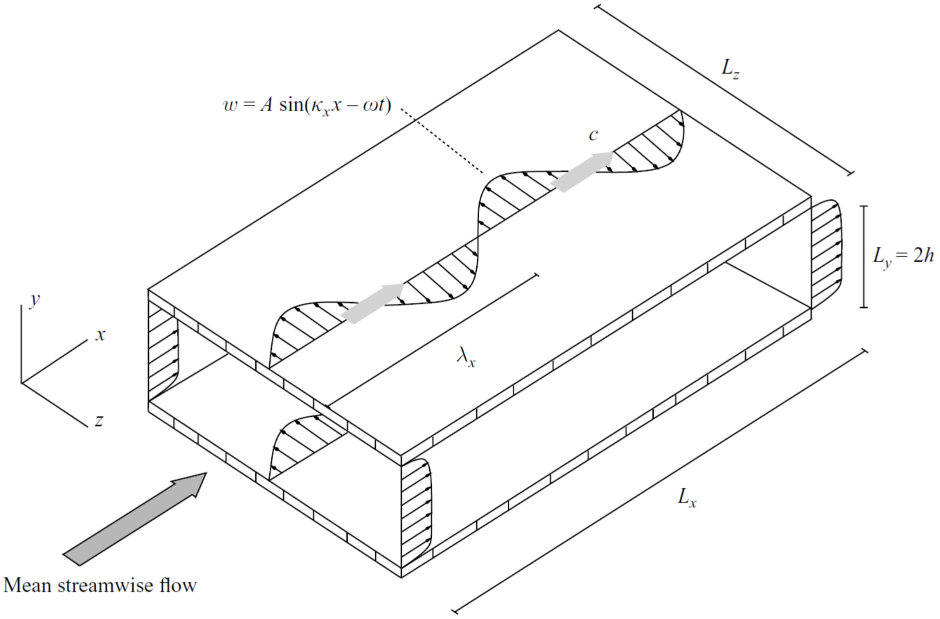

Figure 1.8: Schematic of the streamwise travelling waves for a channel flow. Source: Quadrio et al. (2009b).

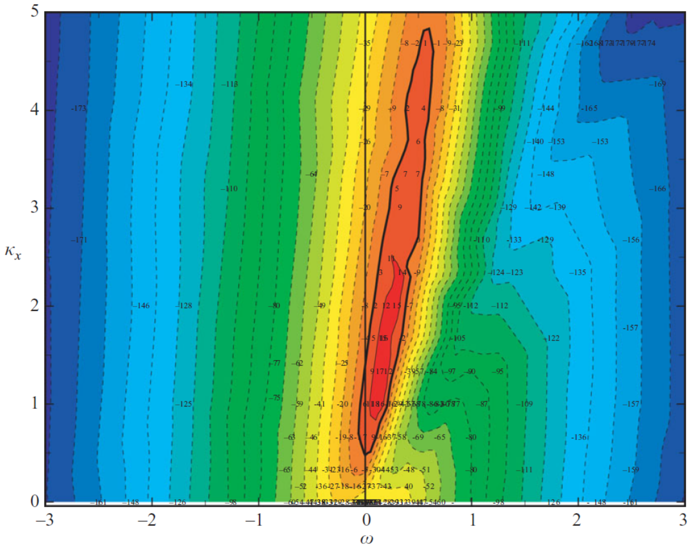

Figure 1.9: Map of net power saving in the $\omega - \kappa_x$ plane for an amplitude parameter of A=0.5 and Re=4760. Source: Quadrio et al. (2009b).

with different tip velocities as well as different discs configurations such as half disc or annular disc. They used the Fukagata-Iwamoto-Kasagi (FIK) identity in Fukagata et al. (2002) and flow visualizations to provide further insight into the dynamics of the streamwise elongated structures appearing between discs. This identity was also used by Wise and Ricco (2014) for analysis, who did a parametric study on the disc diameter and contributed to show some of the future applicability of the oscillating-disc technique.

1.4.2.4 Jets

The techniques mentioned above require direct contact of the moving wall with the fluid to produce drag reduction. However, at the end of last century, a lot of research started regarding jets. A good review of the work is made by Glezer and Amitay (2002).

The first ones using this idea were Bradshaw and Pontikos (1985). They did not produce a jet per se, but the idea of introducing a spanwise component to the streamwise velocity. This was performed by introducing a pressure gradient in the spanwise direction of a wing in a wind tunnel.

Then, Coe et al. (1995), and later Smith and Glezer (1998) kept developing the idea, which was to inject air (or any fluid) into the main stream perpendicularly to the wall to manipulate the flow. However, this injection does not require any fluid to be stored, as a membrane is vibrating inside the cavity, which recycles the air from the main stream. They showed that the jet flow is dominated by the interaction of vortical structures and it was periodic in time.

Meanwhile, Kral et al. (1997) made the first numerical simulation of the jets. This simulation was a two-dimensional incompressible simulation. Rizzetta et al. (1999) also carried out numerical simulations of the flow using jets. Figure 1.10 shows the set up of such jets.

An experimental study of the effects of large streamwise vortices was carried out by Iuso et al. (2002). They used vortex generator jets distributed along a wall as it can be seen in figure 1.11.

Xia and Qin (2005) and Qin and Xia (2008) made numerical simulations using Detached Eddy Simulation (DES). They used a similar device to obtain the synthetic jet, as seen in figure 1.12.

They compared the results with those of Particle Image Velocimetry (PIV) and hot wire (HW), obtaining good agreement between as shown in figure 1.13.

Jets have been used for a variety of cases like separation control (Amitay et al. (2001); Abe et al. (2015)), noise reduction (Sansone et al. (2016)) among others but all of these works

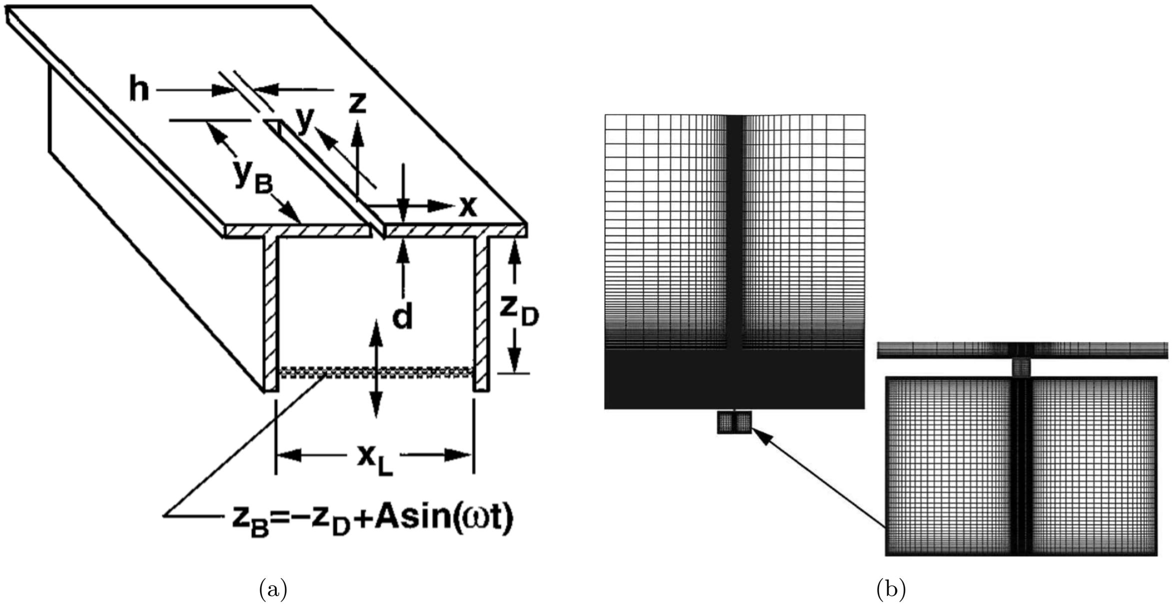

(a)

(b)

Figure 1.10: Schematic of the jet and mesh used in the numerical simulation of Rizzetta et al. (1999).

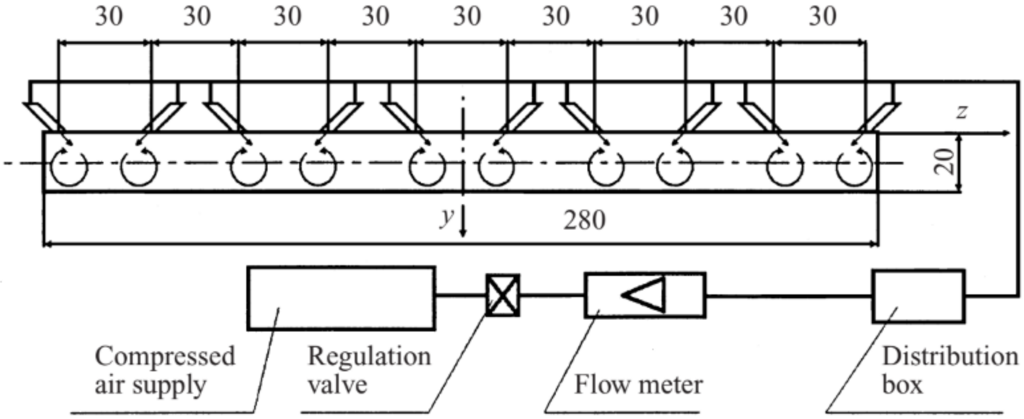

Figure 1.11: Jets of the vortex generation system by Iuso et al. (2002)

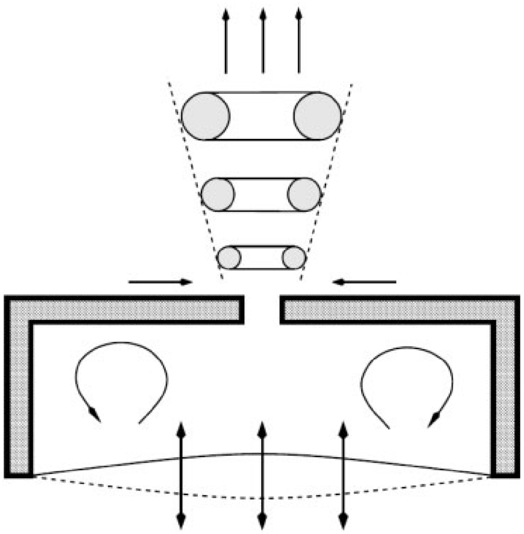

Figure 1.12: Schematic of the synthetic jet from Qin and Xia (2008)

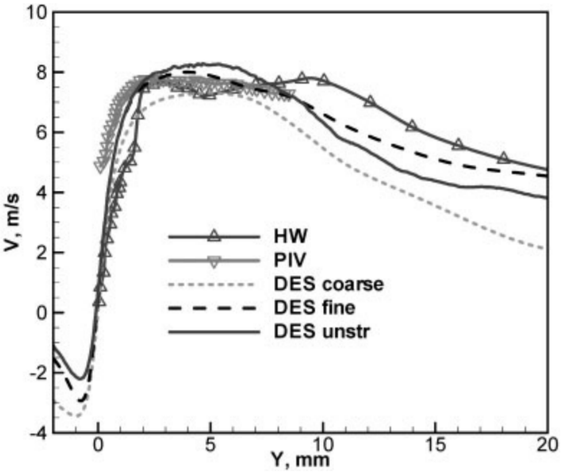

Figure 1.13: Time-averaged jet velocity along the centreline (Qin and Xia (2008)).

are developed with the air being blown perpendicular to the wall.

Even though there is an ongoing research of jets, none of the works previously mentioned in this section aimed to reduce skin friction. Amitay et al. (2001) found that airfoils where the jets are placed experienced a reduction of 45% in pressure drag, but it is as a consequence of the separation control, not the friction reduction.

Spinosa and Zhong (2017) are the only ones known to the author who have calculated a skin friction reduction percentage with normal jets. However, the results of their study are that in the most favourable conditions, they get a skin friction drag increase of 12%.

A similar simulation with spanwise sections of uniform blowing and suction was performed by Kim et al. (2003) on a developing turbulent boundary layer. They concluded that the blowing reduces skin friction but not as much as the suction increases it, which increases it by 10 times more than blowing.

In Xie (2019), wall tangential jets are used, achieving a skin friction drag reduction of 10.7%. This is the first time wall tangential ZMJ are used and the first time a reduction of skin friction drag is achieved with ZMJ. A summary of this active flow control system is found in section 2.7.

There is a need to understand how the jets affect the flow and specifically, the skin friction. For that, a method based on Fukagata et al. (2002) and its extension, Peet and Sagaut (2009), needs to be developed.

1.4.2.5 Effects of wall actuation in turbulent flow structures

Since the idea is to mimic the effects of the moving wall, the target area to be affected is the viscous sublayer. Of course, it is impossible not to affect the entire flow, but the main focus of the proposed device is the near-wall structures. In this study, since the Reynolds number is low, the near-wall dynamics are responsible for most of the friction at the wall (Ricco (2011)).

Several authors have investigated the suppression of turbulent activity due to the spanwise wall motion, which acts on the near wall turbulence, leading to a reduction in skin friction (Choi (2002), Quadrio (2011), Skote (2011), and Lardeau and Leschziner (2013)).

More specifically, Quadrio and Ricco (2004) demonstrated a relation between the forcing period and the drag reduction. There is an optimum frequency, around $T^+ = 100$ where the actuation relates to the characteristic temporal scale of the near-wall turbulent structures. As Ricco (2004) studied, this forcing period relates to the optimum thickness of the Stokes layer, interfering with the near-wall streaks.

There are other mechanisms that affect skin friction, like the one proposed by Agostini and Leschziner (2018). They claim that the large-scale outer structures have direct relation to the skin friction by translating the vortices formed far from the wall to the near-wall flow. In the study of synthetic jets of Yao et al. (2018), they suggested that opposite jets should affect the flow from the wall up to $y^+ = 30$ in order to obtain the maximum drag reduction. However, in the device studied in the thesis, energy consumption is high as demonstrated in section 4.2. Therefore, the WT-ZMJ is constrained to the near-wall flow actuation.

1.5 Objectives of the thesis

The objective of this thesis are the following:

- Analyse the contributions of the skin friction reduction from the WT-ZMJ, an extension of Xie (2019). This is achieved by the introduction of the jet boundary condition in the methodology proposed by Fukagata et al. (2002) and Peet and Sagaut (2009), generalising the use of the equation for this type of boundary condition.

- Carry out an extensive parametric study and apply the derived method to analyse the effect of the various key design parameters on the different contributions of the turbulent skin friction.

- Investigate the power required to produce the jets using a device underneath the channel and compare it with the power savings.

- As a proof of concept, model the WT-ZMJ by modifying the S–A turbulence model (Spalart and Allmaras (1992)) using RANS simulations to predict its effects.

Chapter 2

Methodology, validations and base case

"No man trusts a model except the man who wrote it;
everyone trusts an observation, except the man who made it"
- Harlow Shapley, astronomer

2.1 Introduction

For the study of wall tangential zero-net-mass jets, the use of Computational Fluid Dynamics (CFD) is employed. In this chapter, the fundamentals of the solver used, Shefflow, are going to be presented. Moreover, validations of the code are provided to prove the accuracy of the solver.

Finally, in section 2.7, the Wall Tangential Zero-Mass Jets are presented, which are going to be analysed with other tools and expanded in the following chapters.

2.2 Governing equations and discretisation

The governing equations are the 3-D compressible Navier-Stokes equations:

- Continuity:

$$\frac{\partial \rho}{\partial t} + \nabla \cdot (\rho \boldsymbol{v}) = 0. \tag{2.1}$$

- Momentum:

$$\frac{\partial \rho \boldsymbol{v}}{\partial t} + \nabla \cdot \left(\rho \boldsymbol{v} \otimes \boldsymbol{v} + p \overline{\overline{I}} - \overline{\overline{\tau}} \right) = \rho \boldsymbol{f}_m \tag{2.2}$$

- Energy:

$$\frac{\partial \rho E}{\partial t} + \nabla \cdot \left(\rho \boldsymbol{v} H - \kappa_T \nabla T - \overline{\overline{\tau}} \cdot \boldsymbol{v} \right) = Q_c + Q_r \tag{2.3}$$

where t is time, ρ is density, $\boldsymbol{v}$ is the velocity vector, $\otimes$ is the outer product operator, p is the pressure, $\boldsymbol{f}_m$ are external mass forces per unit mass such as gravity, $\overline{\overline{I}}$ is the identity matrix, E is the energy, which is the addition of the internal energy e and the kinetic energy $|\boldsymbol{v}|^2/2$, H is the enthalpy, which adds the energy E and pressure p, κ_T is the thermal conductivity coefficient, T is the temperature, Q_c and Q_r are the rates of heat release due to chemical reaction and radiation. $\overline{\overline{\tau}}$ is the friction forces tensor, which is defined as

$$\tau_{ij} = \mu \left[(\partial_i v_j + \partial_j v_i) - \frac{2}{3} (\nabla \cdot \boldsymbol{v}) \delta_{ij} \right]. \tag{2.4}$$

where $\partial_i = \partial / \partial x_i$ and δ_{ij} is the Kronecker delta, which is 1 if $i = j$ and 0 otherwise. Then, Navier-Stokes equations can be rearranged as

$$\frac{\partial}{\partial t} \int_{V_c} \boldsymbol{U} \mathrm{d}V + \int_{\Sigma_c} \left(\boldsymbol{F}(\boldsymbol{U}) - \boldsymbol{G}(\boldsymbol{U}) \right) \cdot \boldsymbol{n} \mathrm{d}\sigma = 0, \tag{2.5}$$

where V_c is the control volume with surface boundary Σ_c, $\boldsymbol{U}$ is the variables vector and $\boldsymbol{F}$ and $\boldsymbol{G}$ are the inviscid and viscous fluxes, respectively. The variables vector and the fluxes are

$$
\begin{aligned}
\boldsymbol{U} = \begin{bmatrix} \rho \\ \rho u \\ \rho v \\ \rho w \\ \rho E \end{bmatrix} \quad
\boldsymbol{F}(\boldsymbol{U})_x &= \begin{bmatrix} \rho u \\ \rho u^2 + p \\ \rho u v \\ \rho u w \\ u\left(\rho E + p\right) \end{bmatrix} \quad
\boldsymbol{G}(\boldsymbol{U})_x = \begin{bmatrix} 0 \\ \tau_{xx} \\ \tau_{xy} \\ \tau_{xz} \\ u\tau_{xx} + v\tau_{xy} + w\tau_{xz} + \kappa_T \frac{\partial T}{\partial x} \end{bmatrix}, \\
\boldsymbol{F}(\boldsymbol{U})_y &= \begin{bmatrix} \rho v \\ \rho v u \\ \rho v^2 + p \\ \rho v w \\ v\left(\rho E + p\right) \end{bmatrix} \quad
\boldsymbol{G}(\boldsymbol{U})_y = \begin{bmatrix} 0 \\ \tau_{yx} \\ \tau_{yy} \\ \tau_{yz} \\ u\tau_{yx} + v\tau_{yy} + w\tau_{yz} + \kappa_T \frac{\partial T}{\partial y} \end{bmatrix}, \\
\boldsymbol{F}(\boldsymbol{U})_z &= \begin{bmatrix} \rho w \\ \rho w u \\ \rho w v \\ \rho w^2 + p \\ w\left(\rho E + p\right) \end{bmatrix} \quad
\boldsymbol{G}(\boldsymbol{U})_z = \begin{bmatrix} 0 \\ \tau_{zx} \\ \tau_{zy} \\ \tau_{zz} \\ u\tau_{zx} + v\tau_{zy} + w\tau_{zz} + \kappa_T \frac{\partial T}{\partial z} \end{bmatrix},
\end{aligned}
\tag{2.6}
$$

where u, v and w are the velocity components in x, y and z, respectively. Note that the friction forces tensor is symmetric, i.e. $\tau_{yz} = \tau_{zy}$.

The viscous fluxes, $\boldsymbol{G}$, are obtained with a second order central scheme, whereas the inviscid fluxes, $\boldsymbol{F}$, are obtained using Roe scheme (Roe (1981)), which is developed in Section 2.3.1.

The software to be used in this project is Shefflow. Shefflow is an unstructured, cell-centred and compressible in-house solver. It is capable of carrying out Direct Numerical Simulations (DNS), Large Eddy Simulations (LES), Detached Eddy Simulations (DES) and Reynolds Averaged Navier-Stokes simulations (RANS). In this project, DNS is preferred because the turbulent structure in the near-wall region needs to be well resolved. In chapter 5, RANS is used to model the DNS results acquired in the previous sections.

Shefflow approximates the inviscid fluxes, making use of Monotonic Upstream-Centered Scheme for Conservation Laws (MUSCL) to approximate the values at the cells. In the following sections, the spatial and temporal scheme are discussed.

2.3 Direct Numerical Simulation

2.3.1 Spatial scheme

The spatial scheme used by Shefflow is the Roe scheme. It is important that the method used is precise enough to lead to accurate results but simple enough to be practical. This procedure can be seen in Toro (2013) in Section 11.2.1, particularly for Euler equations in 11.2.2. Euler equations can be written (assuming external sources to be non-existent) by removing $\boldsymbol{G}$ in (2.6).

For the x-component (for the sake of conciseness), instead of writing $\boldsymbol{F}(\boldsymbol{U})_x = \frac{\partial \boldsymbol{F}}{\partial \boldsymbol{X}}$, it can be substituted by $\frac{\partial \boldsymbol{F}}{\partial \boldsymbol{U}} \frac{\partial \boldsymbol{U}}{\partial \boldsymbol{X}} = \boldsymbol{A}(\boldsymbol{U}) \cdot \boldsymbol{U}_x$ applying the chain rule, where $\boldsymbol{A}(\boldsymbol{U})$ is

$$\boldsymbol{A}(\boldsymbol{U}) = \begin{bmatrix} 0 & 1 & 0 & 0 & 0 \\ \hat{\gamma} H - u^2 - c^2 & (3-\gamma)\, u & -\hat{\gamma} v & -\hat{\gamma} w & \hat{\gamma} \\ -uv & v & u & 0 & 0 \\ -uw & w & 0 & u & 0 \\ \frac{1}{2} u \left[(\gamma - 3)\, H - c^2 \right] & H - \hat{\gamma} u^2 & -\hat{\gamma} uv & -\hat{\gamma} uw & \gamma u \end{bmatrix}, \tag{2.7}$$

where $\hat{\gamma} = \gamma - 1$. The eigenvalues of this matrix are

$$\lambda_1 = u - c, \quad \lambda_2 = \lambda_3 = \lambda_4 = u, \quad \lambda_5 = u + c, \tag{2.8}$$

with the right eigenvectors matrix being

$$\boldsymbol{K} = \left[\boldsymbol{K}^{(1)} \boldsymbol{K}^{(2)} \boldsymbol{K}^{(3)} \boldsymbol{K}^{(4)} \boldsymbol{K}^{(5)} \right] = \begin{bmatrix} 1 & 1 & 0 & 0 & 1 \\ u - c & u & 0 & 0 & u + c \\ v & v & 1 & 0 & v \\ w & w & 0 & 1 & w \\ H - uc & \frac{1}{2} \boldsymbol{v}^2 & v & w & H + uc \end{bmatrix}. \tag{2.9}$$

This matrix and eigenvalues are dependent on the values of the flow. The idea is to particularise them to the jump between two values, known as the Riemann problem. The Riemann problem consist of a 1D tube where the quantity values in the negative x space are different and constant to those in the positive x space, i.e.

$$\begin{cases} \boldsymbol{U} = \boldsymbol{U}_L & \text{if } x \leq 0 \\ \boldsymbol{U} = \boldsymbol{U}_R & \text{if } x > 0 \end{cases}. \tag{2.10}$$

Therefore, there is a sudden jump in $x = 0$. The objective is to find the flux value at $x = 0$. The Riemann problem is always found in a Finite Volume Method (FVM) discretisation, because each cell has an averaged value of $\boldsymbol{U}$, and therefore, jumps between two cells are usually found. The Riemann problem can be solved exactly using Godunov method (Godunov (1959)) but it is rather expensive in terms of computational cost. To solve a less expensive computational problem, Roe (1981) proposed a simplified version. It consists in building a matrix $\boldsymbol{A}$ similar to (2.7) but using only left and right values of $\boldsymbol{U}$, therefore $\tilde{\boldsymbol{A}} = \tilde{\boldsymbol{A}}\left(\boldsymbol{U}_L, \boldsymbol{U}_R\right)$. First, a *parameter vector* has to be chosen.

The parameter vector to be chosen for Roe scheme is[1]

$$\boldsymbol{Q}_p = \begin{bmatrix} q_1 \\ q_2 \\ q_3 \\ q_4 \\ q_5 \end{bmatrix} = \sqrt{\rho} \begin{bmatrix} 1 \\ u \\ v \\ w \\ H \end{bmatrix}. \tag{2.11}$$

Then, $\boldsymbol{U}$ and $\boldsymbol{F}$ can be expressed as a function of $\boldsymbol{Q}_p$. Now, an averaged vector $\tilde{\boldsymbol{Q}}$ is found by arithmetic averaging as

$$\tilde{\boldsymbol{Q}} = \begin{bmatrix} \tilde{q_1} \\ \tilde{q_2} \\ \tilde{q_3} \\ \tilde{q_4} \\ \tilde{q_5} \end{bmatrix} = \frac{1}{2}\left(\boldsymbol{Q}_{pL} + \boldsymbol{Q}_{pR}\right). \tag{2.12}$$

With this components in mind, two matrices are to be found, $\tilde{\boldsymbol{B}}$ and $\tilde{\boldsymbol{C}}$, that can be

---

[1] Note that the fifth component of $\boldsymbol{Q}_p$, q_5 depends on H, not in E. Although they are related, it is important not to overlook this fact.

combined into the Roe averaged matrix, $\tilde{\boldsymbol{A}}$, such that

$$\Delta \boldsymbol{U} = \tilde{\boldsymbol{B}}\Delta \boldsymbol{Q}_p; \quad \Delta \boldsymbol{F} = \tilde{\boldsymbol{C}}\Delta \boldsymbol{Q}_p; \quad \Delta \boldsymbol{F} = \tilde{\boldsymbol{A}}\Delta \boldsymbol{U} = \left(\tilde{\boldsymbol{C}}\tilde{\boldsymbol{B}}^{-1}\right)\Delta \boldsymbol{U} \ , \tag{2.13}$$

where Δ means the jump from the right cell to the left cell, i.e. $\Delta q_1 = q_1^R - q_1^L = \sqrt{\rho_R} - \sqrt{\rho_L}$. In the case of Euler equations, these matrices are

$$\tilde{\boldsymbol{B}} = \begin{pmatrix} 2\tilde{q_1} & 0 & 0 & 0 & 0 \\ \tilde{q_2} & \tilde{q_1} & 0 & 0 & 0 \\ \tilde{q_3} & 0 & \tilde{q_1} & 0 & 0 \\ \tilde{q_4} & 0 & 0 & \tilde{q_1} & 0 \\ \frac{\tilde{q_5}}{\gamma} & \frac{\gamma-1}{\gamma}\tilde{q_2} & \frac{\gamma-1}{\gamma}\tilde{q_3} & \frac{\gamma-1}{\gamma}\tilde{q_4} & \frac{\tilde{q_1}}{\gamma} \end{pmatrix} \tag{2.14}$$

and

$$\tilde{\boldsymbol{C}} = \begin{pmatrix} \tilde{q_2} & \tilde{q_1} & 0 & 0 & 0 \\ \frac{\gamma-1}{\gamma}\tilde{q_5} & \frac{\gamma+1}{\gamma}\tilde{q_2} & \frac{\gamma-1}{\gamma}\tilde{q_3} & \frac{\gamma-1}{\gamma}\tilde{q_4} & \frac{\gamma-1}{\gamma}\tilde{q_1} \\ 0 & \tilde{q_3} & \tilde{q_2} & 0 & 0 \\ 0 & \tilde{q_4} & 0 & \tilde{q_2} & 0 \\ 0 & \tilde{q_5} & 0 & 0 & \tilde{q_2} \end{pmatrix}, \tag{2.15}$$

The eigenvalues of $\tilde{\boldsymbol{A}} = \tilde{\boldsymbol{C}}\tilde{\boldsymbol{B}}^{-1}$ and corresponding right eigenvectors matrix being

$$\tilde{\lambda}_1 = \tilde{u} - \tilde{c}, \quad \tilde{\lambda}_2 = \tilde{\lambda}_3 = \tilde{\lambda}_4 = \tilde{u}, \quad \tilde{\lambda}_5 = \tilde{u} + \tilde{c} \tag{2.16}$$

and

$$\tilde{\boldsymbol{K}} = \left[\tilde{\boldsymbol{K}}^{(1)}\tilde{\boldsymbol{K}}^{(2)}\tilde{\boldsymbol{K}}^{(3)}\tilde{\boldsymbol{K}}^{(4)}\tilde{\boldsymbol{K}}^{(5)}\right] = \begin{bmatrix} 1 & 1 & 0 & 0 & 1 \\ \tilde{u} - \tilde{c} & \tilde{u} & 0 & 0 & \tilde{u} + \tilde{c} \\ \tilde{v} & \tilde{v} & 1 & 0 & \tilde{v} \\ \tilde{w} & \tilde{w} & 0 & 1 & \tilde{w} \\ \tilde{H} - \tilde{u}\tilde{c} & \frac{1}{2}\tilde{\boldsymbol{v}}^2 & \tilde{v} & \tilde{w} & \tilde{H} + \tilde{u}\tilde{c} \end{bmatrix}, \tag{2.17}$$

where the averaged values are the following

$$\begin{cases} \tilde{u} = \frac{\sqrt{\rho_L}u_L+\sqrt{\rho_R}u_R}{\sqrt{\rho_L}+\sqrt{\rho_R}} \\ \tilde{v} = \frac{\sqrt{\rho_L}v_L+\sqrt{\rho_R}v_R}{\sqrt{\rho_L}+\sqrt{\rho_R}} \\ \tilde{w} = \frac{\sqrt{\rho_L}w_L+\sqrt{\rho_R}w_R}{\sqrt{\rho_L}+\sqrt{\rho_R}} \\ \tilde{H} = \frac{\sqrt{\rho_L}H_L+\sqrt{\rho_R}H_R}{\sqrt{\rho_L}+\sqrt{\rho_R}} \\ \tilde{c} = \sqrt{(\gamma-1)\left(\tilde{H}-\frac{1}{2}\tilde{\boldsymbol{v}}^2\right)} \end{cases} \tag{2.18}$$

where $\tilde{\boldsymbol{v}}^2 = \tilde{u}^2 + \tilde{v}^2 + \tilde{w}^2$. These are the Roe averages.

In order to find the flux at $x = 0$, the quantities $\boldsymbol{U}_L$ or $\boldsymbol{U}_R$ have to be propagated by means of the eigenvectors. However, the *wave strengths*, $\tilde{\alpha}_i$, have to be found in order to know the contributions from each wave. Projecting the data difference onto the right eigenvectors, it is possible to write

$$\Delta\boldsymbol{U} = \boldsymbol{U}_R - \boldsymbol{U}_L = \sum_{i=1}^{m} \tilde{\alpha}_i \tilde{\boldsymbol{K}}^{(i)} \tag{2.19}$$

and therefore, for the Euler equations,

$$\begin{gathered} \tilde{\alpha}_1 + \tilde{\alpha}_2 + \tilde{\alpha}_5 = \Delta u_1 \\ \tilde{\alpha}_1(\tilde{u}-\tilde{c}) + \tilde{\alpha}_2\tilde{u} + \tilde{\alpha}_5(\tilde{u}+\tilde{c}) = \Delta u_2 \\ \tilde{\alpha}_1\tilde{v} + \tilde{\alpha}_2\tilde{v} + \tilde{\alpha}_3 + \tilde{\alpha}_5\tilde{v} = \Delta u_3 \\ \tilde{\alpha}_1\tilde{w} + \tilde{\alpha}_2\tilde{w} + \tilde{\alpha}_4 + \tilde{\alpha}_5\tilde{w} = \Delta u_4 \\ \tilde{\alpha}_1\left(\tilde{H}-\tilde{u}\tilde{c}\right) + \frac{1}{2}\tilde{\boldsymbol{v}}^2\tilde{\alpha}_2 + \tilde{\alpha}_3\tilde{v} + \tilde{\alpha}_4\tilde{w} + \tilde{\alpha}_5\left(\tilde{H}+\tilde{u}\tilde{c}\right) = \Delta u_5 \end{gathered} \tag{2.20}$$

which leads to

$$\begin{cases} \tilde{\alpha}_3 = \Delta u_3 - \tilde{v}\Delta u_1 \\ \tilde{\alpha}_4 = \Delta u_4 - \tilde{w}\Delta u_1 \\ \tilde{\alpha}_2 = \frac{\gamma-1}{\tilde{c}^2}\left[\Delta u_1\left(\tilde{H}-\tilde{u}^2\right) + \tilde{u}\Delta u_2 - \Delta\hat{u}_5\right] \\ \tilde{\alpha}_1 = \frac{1}{2\tilde{c}}\left[\Delta u_1(\tilde{u}+\tilde{c}) - \Delta u_2 - \tilde{c}\tilde{\alpha}_2\right] \\ \tilde{\alpha}_5 = \Delta u_1 - (\tilde{\alpha}_1 + \tilde{\alpha}_2) \end{cases} \tag{2.21}$$

where $\Delta \hat{u}_5 = \Delta u_5 - (\Delta u_3 - \tilde{v}\Delta u_1)\, \tilde{v} - (\Delta u_4 - \tilde{w}\Delta u_1)\, \tilde{w}$.

Since $\Delta \boldsymbol{F} = \tilde{\boldsymbol{A}}\Delta \boldsymbol{U}$ and, from the definition of right eigenvectors, $\tilde{\boldsymbol{A}}\tilde{\boldsymbol{K}} = \tilde{\lambda}\tilde{\boldsymbol{K}}$, the jump in flux can be defined as

$$\Delta \boldsymbol{F} = \sum_{i=1}^{m} \tilde{\alpha}_i \tilde{\lambda}_i \tilde{\boldsymbol{K}}^{(i)}. \tag{2.22}$$

In the FVM, the flux at the interface has to be computed at the initial step of propagation, $\boldsymbol{F}_{i+\frac{1}{2}}(x/t = 0)$. In order to do that, values from the left and from the right can be used taking into account the physics of the problem. If the flux at the interface is calculated from values from the right cell, the wave speeds that are propagating from left to right (positive average eigenvalues) have to be substracted from the right flux. This is because the waves are propagating from the interface, as the average values are calculated using values at both sides of the interface. So, in order to return to the interface for the calculation of the flux, the wave propagation has to be removed, i.e.

$$\boldsymbol{F}_{i+\frac{1}{2}}(0) = \boldsymbol{F}_R - \sum_{\tilde{\lambda}_i > 0} \tilde{\alpha}_i \tilde{\lambda}_i \tilde{\boldsymbol{K}}^{(i)}. \tag{2.23}$$

If the flux at the interface is calculated from values from the left cell, the wave speeds that are propagating from right to left (negative average eigenvalues) have to be added to the left flux (because they are negative), so

$$\boldsymbol{F}_{i+\frac{1}{2}}(0) = \boldsymbol{F}_L + \sum_{\tilde{\lambda}_i < 0} \tilde{\alpha}_i \tilde{\lambda}_i \tilde{\boldsymbol{K}}^{(i)}. \tag{2.24}$$

Expressions (2.23) and (2.24) are equivalent for subsonic cases. However, in the case of both sides being supersonic (transonic[2] and supersonic cases can be reproduced with the in-house code as well), (2.24) cannot be computed, as $\tilde{\lambda}_i$ is always positive. An alternative form that deals with this problem could be written combining (2.23) and (2.24) as

$$\boldsymbol{F}_{i+\frac{1}{2}}(0) = \frac{1}{2}\left(\boldsymbol{F}_L + \boldsymbol{F}_R\right) - \frac{1}{2}\sum_{i=1}^{m} \tilde{\alpha}_i \left|\tilde{\lambda}_i\right| \tilde{\boldsymbol{K}}^{(i)}. \tag{2.25}$$

This is the equation for the Roe scheme, which can be seen as a central scheme part, $\boldsymbol{F}_c = \frac{1}{2}\left(\boldsymbol{F}_L + \boldsymbol{F}_R\right)$, which is unconditionally unstable in the case of Euler equations, as

---

[2] In this case, a rarefaction wave is created, creating a non-physical phenomena, which is fixed according to Toro (2013).

shown by Hirsch (2007), and a diffusive part, $\boldsymbol{F}_d = -\frac{1}{2}\sum_{i=1}^{m} \tilde{\alpha}_i \left|\tilde{\lambda}_i\right| \tilde{\boldsymbol{K}}^{(i)}$, which stabilises the central scheme because is the upwinding part of the Roe scheme, as it considers the direction of the wave speeds in the calculation of the flux.

To summarize, the steps that Shefflow follows to compute the Roe numerical flux $\boldsymbol{F}_{i+\frac{1}{2}}$ are the following:

1. Compute the average values from (2.18).
2. Compute the corresponding eigenvalues and right eigenvectors by (2.16) and (2.17).
3. Compute the wave strengths using (2.21).
4. Finally, with $\tilde{\alpha}_i$, $\tilde{\lambda}_i$ and $\tilde{\boldsymbol{K}}^{(i)}$ and the flux values at each cell, $\boldsymbol{F}_L$ and $\boldsymbol{F}_R$, compute $\boldsymbol{F}_{i+\frac{1}{2}}$.

High-order method

In order to obtain the quantities from the left and right cells, the MUSCL from Kim and Kim (2005) is coded. The third order MUSCL scheme is defined as follows and it uses the primitive variables, so $\boldsymbol{Q} = \begin{bmatrix} p & u & v & w & T \end{bmatrix}^\top$, not to be confused with the parameter vector of the Roe scheme procedure:

$$\boldsymbol{Q}^L_{i+\frac{1}{2}} = \frac{-\boldsymbol{Q}_{i-1} + 5\boldsymbol{Q}_i + 2\boldsymbol{Q}_{i+1}}{6}, \tag{2.26}$$

$$\boldsymbol{Q}^R_{i+\frac{1}{2}} = \frac{2\boldsymbol{Q}_i + 5\boldsymbol{Q}_{i+1} - \boldsymbol{Q}_{i+2}}{6}, \tag{2.27}$$

and the fifth order scheme,

$$\boldsymbol{Q}^L_{i+\frac{1}{2}} = \frac{2\boldsymbol{Q}_{i-2} - 13\boldsymbol{Q}_{i-1} + 47\boldsymbol{Q}_i + 27\boldsymbol{Q}_{i+1} - 3\boldsymbol{Q}_{i+2}}{60}, \tag{2.28}$$

$$\boldsymbol{Q}^R_{i+\frac{1}{2}} = \frac{-3\boldsymbol{Q}_{i-1} + 27\boldsymbol{Q}_i + 47\boldsymbol{Q}_{i+1} - 13\boldsymbol{Q}_{i+2} + 2\boldsymbol{Q}_{i+3}}{60}. \tag{2.29}$$

2.3.2 Temporal scheme

For the temporal discretisation, there are 2 options implemented: Explicit method and the Dual Time Step method (DTS). Both of them use the Runge-Kutta scheme (RK), which consist of obtaining the solution for the next step $(n+1)$ through a series of stages (k) as it can be seen in the following equation:

$$\begin{aligned}
\boldsymbol{U}^{(0)} &= \boldsymbol{U}^{n} \\
\boldsymbol{U}^{(1)} &= \boldsymbol{U}^{n} - \alpha_1 \Delta\tau\, R\left(\boldsymbol{U}^{(0)}\right) \\
\boldsymbol{U}^{(2)} &= \boldsymbol{U}^{n} - \alpha_2 \Delta\tau\, R\left(\boldsymbol{U}^{(1)}\right) \\
&\vdots \\
\boldsymbol{U}^{(k-1)} &= \boldsymbol{U}^{n} - \alpha_{k-1} \Delta\tau\, R\left(\boldsymbol{U}^{(k-2)}\right) \\
\boldsymbol{U}^{(k)} &= \boldsymbol{U}^{n} - \alpha_{k} \Delta\tau\, R\left(\boldsymbol{U}^{(k-1)}\right) \\
\boldsymbol{U}^{n+1} &= \boldsymbol{U}^{(k)}
\end{aligned} \tag{2.30}$$

where α_k is the coefficient for that stage, $\Delta\tau$ is the temporal step and $R(\cdot)$ is the residual.

If the simulation is compressible, the Explicit option for Shefflow is preferred, as it consumes less memory. The procedure for this scheme is the following:

1. MUSCL scheme provides the quantities (Q_L and Q_R) from the primitive values of cells.
2. Roe scheme solves the reduced Riemann problem from the quantities provided by the MUSCL scheme to obtain the inviscid flux on the surface between left and right cells. A central scheme calculates the viscous flux.
3. The quantities for the next time step are calculated using a 3, 4 or 5 stages RK to solve the algebraic discretized Navier-Stokes equations. Then, the loop is started again with the new values.

This option is an explicit method, so the time step has to meet a requirement to be stable. The travelling waves, associated with the eigenvalues, have to travel a space that is less than the smallest grid in the simulation in each time step. Therefore, the time step is chosen according to the following formula:

$$\Delta t \leq \frac{\Delta x}{\max\left(u + c, u - c\right)}, \tag{2.31}$$

where Δt is the time step, Δx is the smallest length in a cell, u is the speed of the flow in that cell and c is the speed of sound.

In the case of the simulation being incompressible or at low Mach number, the density does not change or the change approaches to zero and therefore, the speed of sound approaches infinity, as $c = \partial p/\partial \rho$. The eigenvalues for the inviscid Navier-Stokes equations have very different values ($u + c$ and $u - c$) and therefore, the convergence to a solution is slow as $\Delta t \to 0$. To solve that, a preconditioning is used.

2.3.2.1 Preconditioning

Since the inviscid part of (2.5) has very different eigenvalues as c approaches to infinity, a preconditioning matrix, $\boldsymbol{\Gamma}$, is multiplied following Weiss and Smith (1995). First, the chain rule is applied so that $\frac{\partial \boldsymbol{U}}{\partial t} = \frac{\partial \boldsymbol{U}}{\partial \boldsymbol{Q}} \frac{\partial \boldsymbol{Q}}{\partial t}$. Then, $\frac{\partial \boldsymbol{U}}{\partial \boldsymbol{Q}}$ is brought outside the integral and the whole equation is premultiplied by the transformation matrix $\boldsymbol{K}_t$ as

$$\boldsymbol{K}_t \frac{\partial \boldsymbol{U}}{\partial \boldsymbol{Q}} \frac{\partial}{\partial t} \int_{V_c} \boldsymbol{Q} \mathrm{d}V + \boldsymbol{K}_t \int_{\Sigma_c} (\boldsymbol{F} - \boldsymbol{G}) \cdot \boldsymbol{n} \, \mathrm{d}\sigma = 0, \tag{2.32}$$

where

$$\boldsymbol{K}_t \frac{\partial \boldsymbol{U}}{\partial \boldsymbol{Q}} = \begin{bmatrix} \rho_p & 0 & 0 & 0 & \rho_T \\ 0 & \rho & 0 & 0 & 0 \\ 0 & 0 & \rho & 0 & 0 \\ 0 & 0 & 0 & \rho & 0 \\ -1 & 0 & 0 & 0 & \rho C_p \end{bmatrix}, \tag{2.33}$$

where ρ_p and ρ_T the pressure and temperature time derivatives in the continuity equation. The first one, ρ_p, is the one controlling the speed of the propagation waves in the system, so it is replaced by $\Theta = \left(\frac{1}{U_r^2} - \frac{\rho_T}{\rho C_p} \right)$, where U_r is the reference velocity. Then, the whole equation is premultiplied by $\boldsymbol{K}_t^{-1}$ obtaining

$$\boldsymbol{\Gamma} \frac{\partial}{\partial t} \int_{V_c} \boldsymbol{Q} \mathrm{d}V + \int_{\Sigma_c} (\boldsymbol{F} - \boldsymbol{G}) \cdot \boldsymbol{n} \, \mathrm{d}\sigma = 0, \tag{2.34}$$

where

$$\boldsymbol{\Gamma} = \boldsymbol{K}_t^{-1} \begin{bmatrix} \rho_p & 0 & 0 & 0 & \rho_T \\ 0 & \rho & 0 & 0 & 0 \\ 0 & 0 & \rho & 0 & 0 \\ 0 & 0 & 0 & \rho & 0 \\ -1 & 0 & 0 & 0 & \rho C_p \end{bmatrix} = \begin{bmatrix} \Theta & 0 & 0 & 0 & \rho_T \\ \Theta u & \rho & 0 & 0 & \rho_T u \\ \Theta v & 0 & \rho & 0 & \rho_T v \\ \Theta w & 0 & 0 & \rho & \rho_T w \\ \Theta H - 1 & \rho u & \rho u & \rho u & \rho_T H + \rho C_p \end{bmatrix}, \tag{2.35}$$

making the eigenvalues for the current system $\lambda_1 = u' - c', \lambda_2 = \lambda_3 = \lambda_4 = u, \lambda_5 = u' + c'$, being

$$\begin{aligned} u' &= u\left(1-\alpha\right), \\ c' &= \sqrt{\alpha^2 u^2 + U_r^2}, \\ \alpha &= \left(1 - \beta U_r^2\right)/2, \\ \beta &= \rho_p + \tfrac{\rho_T}{\rho C_p}, \end{aligned} \tag{2.36}$$

effectively increasing the convergence speed of the simulation by changing the speed of propagation of information. However, the side effect of this method is to destroy the time accuracy in the sense that it becomes a steady solution from an unsteady initial condition (the previous time step). In order to fix it and calculate unsteady problems, a pseudo time step can be substituted instead of the physical time in (2.34) and another temporal derivative (first term of (2.5)) is introduced. A steady state solution is calculated for every pseudo time step, reducing the residual at each iteration.

This process consists of 3 loops, the Runge-Kutta loop, the steady state loop and the unsteady loop.

1. The Runge-Kutta loop is based on either the three stage version, RK3 or the five stage version, RK5. In this loop, the inviscid solution is calculated using the RK scheme and the viscous solution is updated every other RK stage. Since the temporal accuracy is not important, RK3 is recommended as it is faster.

2. For every RK loop, fluxes are computed and introduced in the Navier-Stokes equations, which produce a closer spatial solution. However, the equations are unbalanced and a residual is obtained. This solution is introduced again into the RK loop to obtain an even closer solution, reducing the residual. When the residual is low enough, the steady state solution to the flow field from the previous step is achieved.

3. The unsteady loop is the simulation itself. When the previous loop has develop a good residual, the spatial solution is used along with the physical time term, which will calculate the next time step solution.

The following equation exposes the different loops of the DTS scheme,

$$\underbrace{\frac{\partial}{\partial t}\int_{V_c} \boldsymbol{U}\mathrm{d}V}_{\text{physical time term}} + \underbrace{\underbrace{\boldsymbol{\Gamma}\frac{\partial}{\partial \tau}\int_{V_c} \boldsymbol{Q}\mathrm{d}V}_{\text{pseudo time term}} + \int_{\Sigma_c} \left(\boldsymbol{F} - \boldsymbol{G}\right)\cdot \boldsymbol{n}\mathrm{d}\sigma = 0}_{\text{RK and steady loop}}, \tag{2.37}$$

where t and τ are the physical and pseudo times.

2.3.3 Dynamic grid movement

One of the features of Shefflow is the dynamic grid, this allows the computational domain to change every time step. This feature is used particularly in section 4.2. Since moving parts are to be modelled, the grid modification has to follow certain rules.

The grid movement algorithm has been developed with 2 objectives:

1. Maintain the same grid spacing near the wall in order to keep the same definition of the flow near the wall.

2. Provide a smooth grid compression or expansion between two points of the grid.

To achieve this, a third order polynomial is created, where the constants are chosen following the boundary conditions

$$\begin{cases} \Delta x(p(x_2, y)) = u_{wall} \\ \Delta x'(p(x_2, y)) = 0 \\ \Delta x(p(x_1, y)) = 0 \\ \Delta x'(p(x_1, y)) = 0 \end{cases} \tag{2.38}$$

where x_2 is the first grid that can be compressed or expanded near the wall, x_1 is the end of the compression or expansion domain and Δx is the maximum movement of the wall at a certain time step. With this function, all grid nodes between the wall coordinate and x_2 will move Δx to maintain the grid spacing near the wall, the nodes between x_1 and x_2 will be moved according to the polynomial, and the rest of the nodes will not be moved. Figure 2.1 shows the schematic and function that results from (2.38).

On top of that function, a slope control is used. This control relaxes the slope in the derivative conditions of (2.38) to make the deformation less abrupt at the middle of the grid as

$$\begin{cases} \Delta x(p(x_2, y)) = u_{wall} \\ \Delta x'(p(x_2, y)) = \xi \frac{u_{wall}}{x_2 - x_1} \\ \Delta x(p(x_1, y)) = 0 \\ \Delta x'(p(x_1, y)) = \xi \frac{u_{wall}}{x_2 - x_1} \end{cases} \tag{2.39}$$

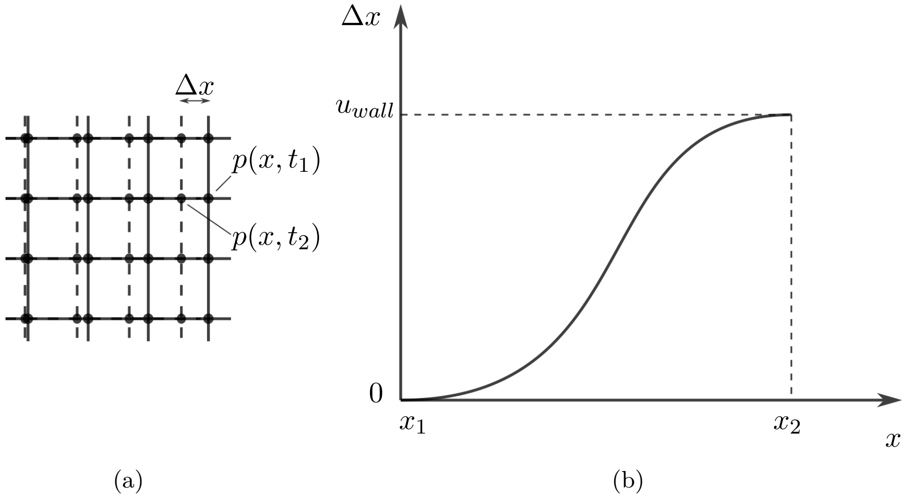

(a)

(b)

Figure 2.1: Schematic of the dynamic grid movement (a) and the dynamic grid movement function with $\xi = 0$ (b).

where ξ is a parameter from 0 to 1, where 0 recovers the original movement and 1 is a completely linear distribution of movement.

2.4 Turbulence models

DNS is the most accurate and precise method to solve the Navier-Stokes equations. It provides the exact solution of the flow field in space and time, only depending on the discretisation techniques, spatial resolution and boundary conditions treatment. However, DNS is restricted to low Reynolds number Re flows due to computational cost. The Reynolds number is defined as

$$Re = \frac{\rho U L}{\mu} \tag{2.40}$$

where U is the characteristic velocity, L is the characteristic length and μ is the dynamic viscosity. The values of U and L can be chosen according to the flow features or geometry of the problem, i.e. U can be the bulk velocity, the friction velocity, the Poiseuille's velocity, etc. and L can be the chord of an airfoil, length of a fuselage, boundary layer thickness or the coordinate x along a wall among others. The higher the Reynolds number is, the finer the grid has to be, and therefore, the smaller the time step has to be to properly capture the smallest turbulent scales, also referred to as Kolmogorov scales. It can be shown (Davidson

(2017)) that the smallest turbulent length and time scales decrease with $Re^{-3/4}$ and $Re^{-1/2}$, respectively. As an example, if the Reynolds number is increased by a factor of 10, the number of cells has to be increased by a factor of $\left(\Delta Re^{3/4}\right)^3 \Delta Re^{1/2} \approx 562$.

Although for low Reynolds numbers cases DNS is feasible, another solution has to be found for high Reynolds numbers such as the ones in section B.1. There are different levels of approximation and different assumptions that can be made to solve a flow. The two most popular methods used in research and industry are: Reynolds-Averaged Navier Stokes (RANS) and Large Eddy Simulations (LES). The first one is the one studied in this thesis.

2.4.1 RANS Simulations

In a turbulent flow, the variables can be decomposed into a Favre[3] time averaged value as $\psi = \tilde{\psi} + \psi'$. Applying this kind of average to the equations, the Reynolds-Averaged Navier-Stokes compressible equations are obtained, in differential form using tensor notation[4],

$$\frac{\partial \bar{\rho}}{\partial t} + \frac{\partial \bar{\rho}\tilde{u}_i}{\partial x_i} = 0 \tag{2.41}$$

$$\frac{\partial \left(\bar{\rho}\tilde{u}_i\right)}{\partial t} + \frac{\partial \left(\bar{\rho}\tilde{u}_i\tilde{u}_j\right)}{\partial x_i} + \frac{\partial \left(\bar{\rho}\widetilde{u_i'u_j'}\right)}{\partial x_i} = -\frac{\partial \tilde{p}}{\partial x_j} - \frac{\partial \tilde{\tau}_{ij}}{\partial x_i} \tag{2.42}$$

where an extra term is found, generally referred as Reynolds stresses, $\bar{\tau}_{ij} = -\bar{\rho}\widetilde{u_i'u_j'}$. This symmetric tensor introduces 6 new variables (It introduces 9, but because of symmetry, only 6 are different) but does not provide for new equations, this is called the closure problem, as the number of unknowns (eleven: two state variables i.e. ρ and T, three velocity components and six stresses) is larger than the number of equations (five: continuity, momentum in each direction and energy equations). There are different methods to provide the needed equations modelling these stresses (which can be found in Davidson (2017)). The method studied in this thesis is the Spalart-Allmaras model. It uses the Boussinesq assumption, which introduces an eddy or turbulent viscosity ν_t, to model the Reynolds stresses that will be added to the natural viscosity of the problem. This method uses a time marching approach to solve a steady problem.

---

[3] Favre (1983) introduced this operation where $\tilde{\psi} = \overline{\rho\psi}/\bar{\rho}$ and the bar represents the Reynolds-averaged operation.

[4] Also known as Einstein notation, where i.e. $x_i x_j = \sum_{i=1}^{n}\sum_{j=1}^{m} x_i x_j$

2.4.1.1 Spalart-Allmaras turbulence model

This model was introduced by Spalart and Allmaras (1992) and modified in Allmaras et al. (2012) to prevent negative values of the modified vorticity $\tilde{S}$. This is a one-equation model that assumes that k in (2.43) is negligible.

$$\widetilde{u_i' u_j'} = -2\nu_t \bar{S}_{ij} + \frac{2}{3}\delta_{ij} k, \tag{2.43}$$

where $\bar{S}_{ij} = \frac{1}{2}\left(\frac{\partial \tilde{u}_i}{\partial x_j} + \frac{\partial \tilde{u}_j}{\partial x_i}\right)$.

Therefore, only ν_t has to be found, reducing the computational time considerably with respect to other models. The eddy viscosity ν_t is given by

$$\nu_t = \tilde{\nu} f_{\mathrm{v1}}, \qquad f_{\mathrm{v1}} = \tfrac{\chi^3}{\chi^3 + c_{\mathrm{v1}}^3}, \qquad \chi = \tfrac{\tilde{\nu}}{\nu} \tag{2.44}$$

and $\tilde{\nu}$ is given by the model equation

$$\frac{D\tilde{\nu}}{Dt} = P - D + \frac{1}{\sigma}\left[\nabla \cdot \left(\left(\nu + \nu_t\right) \nabla \tilde{\nu}\right) + c_{\mathrm{b2}} \left(\nabla \tilde{\nu}\right)^2\right], \tag{2.45}$$

where $\frac{D}{Dt}$ is the material derivative[5] and P and D are the production and wall destruction terms, respectively, which are

$$P = c_{\mathrm{b1}} \tilde{S} \tilde{\nu}, \qquad D = c_{\mathrm{w1}} f_{\mathrm{w}} \left(\tfrac{\tilde{\nu}}{d}\right)^2 \tag{2.47}$$

with

$$\tilde{S} = S + \frac{\tilde{\nu}}{\kappa^2 d^2} f_{\mathrm{v2}}, \qquad f_{\mathrm{v2}} = 1 - \frac{\chi}{1 + \chi f_{\mathrm{v1}}},$$
$$f_{\mathrm{w}} = g\left[\frac{1 + c_{\mathrm{w3}}^6}{g^6 + c_{\mathrm{w3}}^6}\right]^{1/6}, g = r + c_{\mathrm{w2}}\left(r^6 - r\right), \quad r = \min\left(\frac{\tilde{\nu}}{\tilde{S}\kappa^2 d^2}, \quad r_{\mathrm{lim}}\right) \tag{2.48}$$

where S is the magnitude of the vorticity and the empirical constants are gathered in table 2.1.

This model will be further studied in chapter 5.

---

[5] The material derivative operator

$$\frac{\mathrm{D}()}{\mathrm{D}t} = \frac{\partial()}{\partial t} + \boldsymbol{v} \cdot \nabla() \tag{2.46}$$

expresses the variation in time of any quantity following the fluid particle

Constant	Value
c_{b1}	0.1355
σ	2/3
c_{b2}	0.622
κ	0.41
c_{w1}	$\frac{c_{\mathrm{b1}}}{\kappa^2}+\frac{1+c_{\mathrm{b2}}}{\sigma}$
c_{w2}	0.3
c_{w3}	2
c_{v1}	7.1
r_{lim}	10
d	distance to the closest wall

Table 2.1: Spalart-Allmaras model constants.

2.5 Validation of Shefflow code

Although Shefflow has been used for around a decade, there are always improvements and changes. These have to be tested and the best way to do it is through well known problems that provide an idea of the degree of accuracy the solver offers.

In this case, three main problems have been reproduced. The first one is the 2D vortex, which will validate the inviscid part of the code and the boundary conditions (symmetric and periodic). The second case to be tested is the Taylor-Green vortex test-case, which is used to validate the numerical dissipation of the solver and the inviscid part. Finally, the last problem is the channel case, which will serve as a validation of the viscous part of the code and as a starting point for the main simulations.

So far, DNS has been used since it is of paramount importance to capture the physics correctly. Once they are captured, a RANS model could be derived.

2.5.1 2D vortex

The isentropic Euler vortex problem is a very popular case to test the numerical diffusion of solvers regarding the domain discretisation (Castonguay et al. (2011); Gao and Wang (2013); Williams and Jameson (2013); Witherden et al. (2014)). There are different ways of producing the vortex and the one followed by this thesis is the one from Wang et al. (2013).

The problem consists of setting a stable vortex in a resting fluid (or moving at a constant speed). Dynamic viscosity, μ, is set to zero, which means that if the inviscid part of the solver were perfect and the grid very fine, the vortex would be maintained forever, not changing in shape or intensity at all. Since this is not usually the case, the error has to be assessed, as the domain is discretised, not continuous. Moreover, two different boundary conditions are set: a symmetry boundary condition to make the problem a 2D problem and a couple of periodic boundary conditions to let the vortex move if the unperturbed flow speed is not zero.

The initial conditions to be kept at all times for a vortex of radius R and strength β at coordinates (X_0, Y_0) are the following:

$$\begin{aligned} u &= u_\infty + \delta u \\ v &= \delta v \\ T &= T_\infty + \delta T \end{aligned} \tag{2.49}$$

where

$$\begin{aligned} &(\delta u, \delta v) = \tfrac{u_\infty \beta}{R} e^{\frac{-r^2}{2}} \left(-\left(y - Y_0\right), x - X_0\right) \\ &\delta T = -\tfrac{(u_\infty \beta)^2}{2C_p} e^{\frac{-r^2}{2}} \\ &C_p = \tfrac{\gamma}{\gamma - 1} R_{gas} \\ &r = \tfrac{\sqrt{(x-X_0)^2 + (y-Y_0)^2}}{R} \\ &u_\infty = M_\infty \sqrt{\gamma R_{gas} T_\infty} \end{aligned} \tag{2.50}$$

Since it is an isentropic gas, $\rho = \rho_\infty \left(\frac{T}{T_\infty}\right)^{1/(\gamma-1)}$ and ρ_∞ can be calculated with the ideal gas equation provided p_∞ and T_∞. The values used for the validation are $M_\infty = 0.5$, $\beta = 1/5$, $R = 0.005$, $p_\infty = 105\, N/m^2$ and $T_\infty = 300K$ with a computational domain of $L_x = L_y = 0.1\, m$ and $X_0 = Y_0 = 0.05\, m$.

The grids employed had 32^2, 64^2, 128^2 and 256^2 cells and they are run for 4000 time steps with $\Delta t = 0.5 \times 10^{-4}\, s$ using both explicit and DTS methods (Section 2.3.2). Then, the least absolute deviation[6] (L1-norm) is calculated for i.e. the density and the results are gathered in table 2.2. The order is calculated as the base 10 logarithmic subtraction of the L1-norm over the base 10 logarithmic subtraction of the number of cells.

Both methods show similar results as expected, since both are using the same spatial

---

[6] $L_1 = \sum_{i=1}^{n} \left|\rho_i^0 - \rho_i\right|$ where ρ_i^0 is the initial density at cell i and ρ_i is the instantaneous density at cell i.

Explicit method				Dual Time Step method			
Grid	L1-norm	order	CPU time (h:mm:ss)	Grid	L1-norm	order	CPU time (h:mm:ss)
32^2	2.83514e-02		0:00:08	32^2	2.83514e-02		0:00:45
64^2	6.11611e-03	2.21	0:00:22	64^2	6.11584e-03	2.21	0:02:49
128^2	8.54563e-04	2.84	0:01:15	128^2	8.54545e-04	2.84	0:20:12
256^2	1.09803e-04	2.96	0:05:00	256^2	1.09799e-04	2.96	1:23:17

Table 2.2: Isentropic Euler Vortex results using third order MUSCL scheme.

Explicit method			
Grid	L1-norm	order	CPU time (h:mm:ss)
32^2	1.69364e-02		0:00:10
64^2	1.96372e-03	3.11	0:00:34
128^2	7.83765e-05	4.65	0:02:08
256^2	2.72698e-06	4.85	0:10:27

Table 2.3: Isentropic Euler Vortex results using fifth order MUSCL scheme.

scheme. However, DTS employs more time to do the calculations since it has to go through the additional loop of the pseudo time step, which in the case of a compressible problem, is unnecessary. It has to be noted that the third order accuracy is almost achieved as third order MUSCL scheme is employed. For the fifth order MUSCL scheme, only the explicit method is simulated, as the DTS is proven to achieve the same accuracy but in more time. The results can be seen in table 2.3 and the plots for least absolute deviation and time spent in figure 2.2.

2.5.2 Taylor-Green vortex test-case

The Taylor-Green Vortex (TGV) case is simulated to study the accuracy of different numerical schemes, more precisely, the numerical dissipation of the scheme. It was originally proposed by Taylor and Green (1937), and since then, many authors have used it to validate their numerical schemes such as Brachet et al. (1983), Brachet (1991), Drikakis et al. (2007), Neeteson et al. (2016), Asada and Kawai (2017), DeBonis (2013), among others. DeBonis (2013) is the one used in this work.

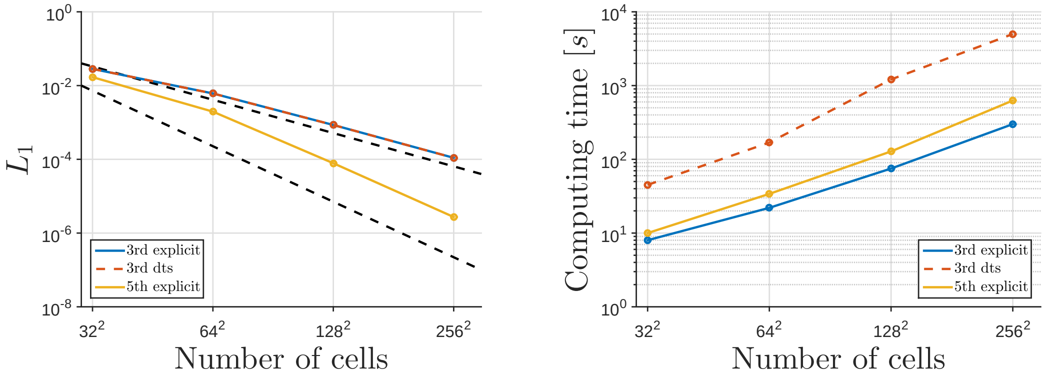

(a) (b)

Figure 2.2: L_1 norm and time spent in the simulation. Dashed black lines represent slope of third and fifth order decay.

Vortex quantities	Value
Reynolds number, Re	1600
Temperature, T_0	$300\,K$
Length, L	$1\,mm$
Kinematic viscosity, ν	$1.846 \times 10^{-5}\,\frac{m^2}{s}$
Density, ρ_0	$1.225\,\frac{Kg}{m^3}$

Table 2.4: Flow conditions.

The vortex initial conditions are the following for a $2\pi L$ side length cube:

$$
\begin{aligned}
u &= u_{\text{ref}} \sin\left(\frac{x}{L}\right)\cos\left(\frac{y}{L}\right)\cos\left(\frac{z}{L}\right) \\
v &= -u_{\text{ref}} \cos\left(\frac{x}{L}\right)\sin\left(\frac{y}{L}\right)\cos\left(\frac{z}{L}\right) \\
w &= 0 \\
p &= p_0 + \frac{\rho_0 u_{\text{ref}}^2}{16}\left(\cos\left(\frac{2x}{L}\right)+\cos\left(\frac{2y}{L}\right)\right)\left(\cos\left(\frac{2z}{L}\right)+2\right)
\end{aligned}
\tag{2.51}
$$

Since the solver works in dimensional units, table 2.4 is provided.

The previous simulations have been carried out with different mesh sizes and schemes.

The reference solution of Wang et al. (2013), used a 512^3 cells mesh to compute the DNS simulation. A 128^3 cells mesh has been used with the third order and fifth order MUSCL scheme; and a 256^3 cells mesh has been used with the fifth order MUSCL scheme. Figure 2.3 shows four instants of time for the simulation using 256^3 cells.

Note that $t = t_{\text{physical}} \frac{u_{\text{ref}}}{L}$, where t_{physical} is the physical time step of the simulation.

To assess the validation of the simulation, the energy and energy dissipation rate are compared. The energy is calculated as

$$E_k = \frac{1}{\rho_0 V} \int_V \rho \frac{\boldsymbol{v} \cdot \boldsymbol{v}}{2} \mathrm{d}V, \tag{2.52}$$

where V is volume. The energy dissipation rate is defined as $\epsilon = -\frac{dE_k}{dt}$. Plotting the results for all simulations mentioned above, figure 2.4 is obtained.

The improvement from third order to fifth order MUSCL scheme is clearly visible. If the number of cells is doubled in every axis, the curve is reproduced closely until $t \approx 8-9$, where the peak is almost reproduced, but not exactly. After the peak, the 256^3 simulation is close enough to consider it as a good result, but it could be improved. However, the more the time passes, the more difficult is to obtain the curve, as the smallest scale vortices are dissipating, requiring a finer mesh to capture the physics involved.

Another way to see the evolution of the solution is through a Power Spectral Density (PSD) of the energy. A Discrete Fourier Transform (DFT) is applied to all rows and columns of the mesh, and then averaged to obtain the energy of the eddies as a function of the spatial frequency (or wave number). Then, the PSD is obtained using the following formula:

$$\text{PSD} = \frac{1}{N^2} \left| X_k \right|^2, \tag{2.53}$$

where N is the number of samples and X_k are the result from the DFT. Since the PSD is periodic (with period equal to the number of samples N) and symmetric with respect to the wave number $k = N/2$, the one-sided PSD is obtained by multiplying the above expression by 2 and representing it in the range $k = 0, 1, ...N/2$.

A typical spectrum for turbulent kinetic energy is divided into 3 parts (Figure 2.5). Zone I is containing the eddies that extract energy from the main flow, in this case, there is no production of energy apart from the initial conditions. Zone II is the inertial subrange, where, when the flow is fully turbulent, there is a decay of -5/3 with the wave number. Zone III is called the dissipation range, where the eddies are small and isotropic. In this zone, the

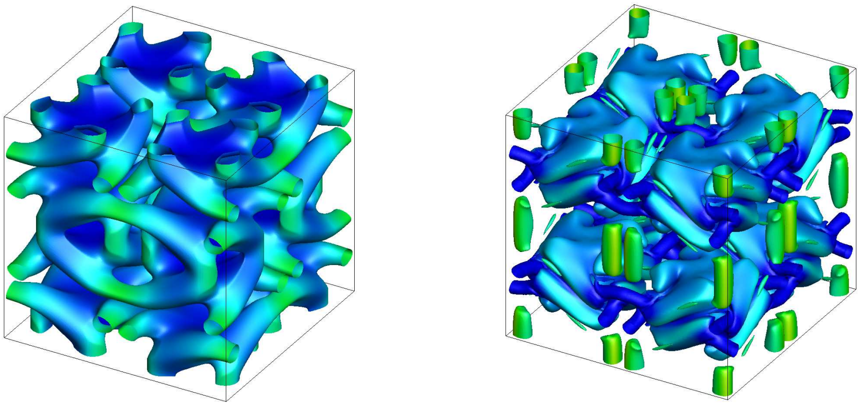

(a) $t = 2.5$ (b) $t = 5$

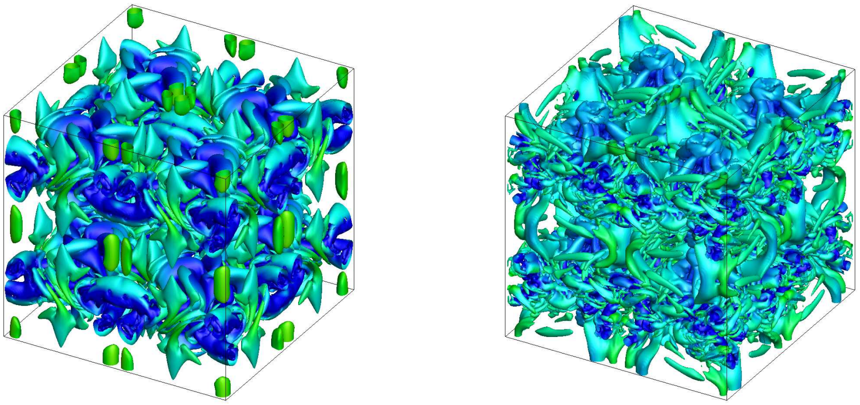

(c) $t = 7.5$ (d) $t = 15$

Figure 2.3: Taylor-Green vortices at different instants of time. It shows the isosurface of λ_2 (Jeong and Hussain (1995)) and coloured by pressure.

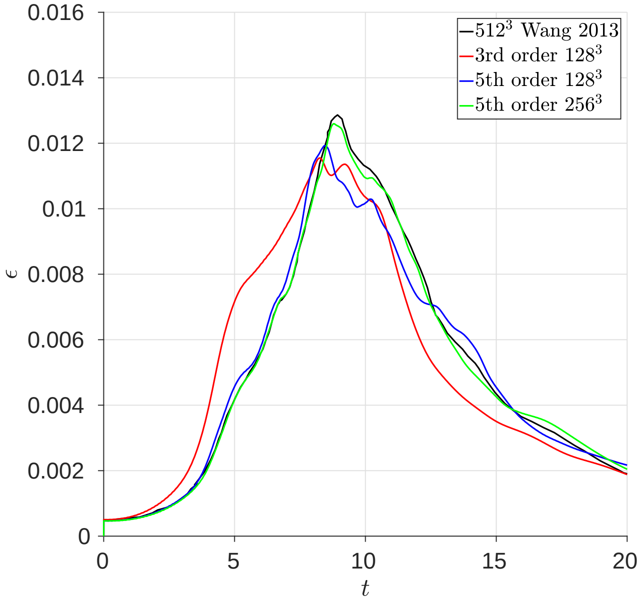

Figure 2.4: Energy dissipation rate.

dissipation of the eddies into thermal energy occurs.

The PSD for several time steps as a function of the wave number is shown in Figure 2.6.

For the first steps, the vortices are developing and one cannot find too many breaking eddies, that is why all the energy is found in the smaller wave numbers. As time increases, the energy decreases for the small wave numbers and increases for the large wave number eddies as it is expected. Comparing with Wang et al. (2013), it could be said that the inviscid part of the code and the numerical dissipation are validated to continue onwards.

2.5.3 Channel flow

The last validation step is to prove that the viscous section of the solver is accurate. It is achieved with the results from a turbulent channel case. Besides validation, this test case will provide a starting point for the jets case.

The channel is defined as a box of dimensions $L_x^+ = 4\pi h^+$, $L_y^+ = 2h^+$ and $L_z^+ = \frac{4}{3}\pi h^+$ with air flowing in the x-direction as seen in figure 2.7.

L_x^+ and L_z^+ are the computational boundaries for the channel, as it is impossible to simulate

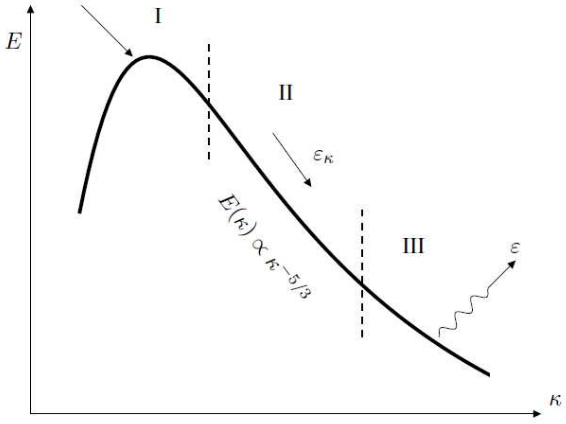

Figure 2.5: Spectrum for turbulent kinetic energy. Source: Davidson (2017).

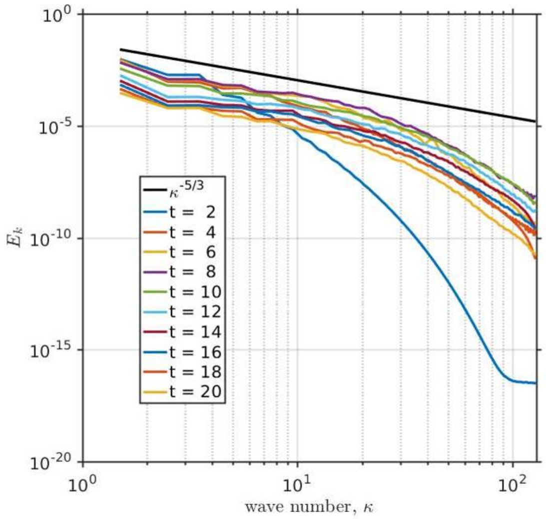

Figure 2.6: Energy PSD for 256^3 cells. The black line represents the Kolmogorov spectrum law or $-5/3$ law (Davidson (2017)).

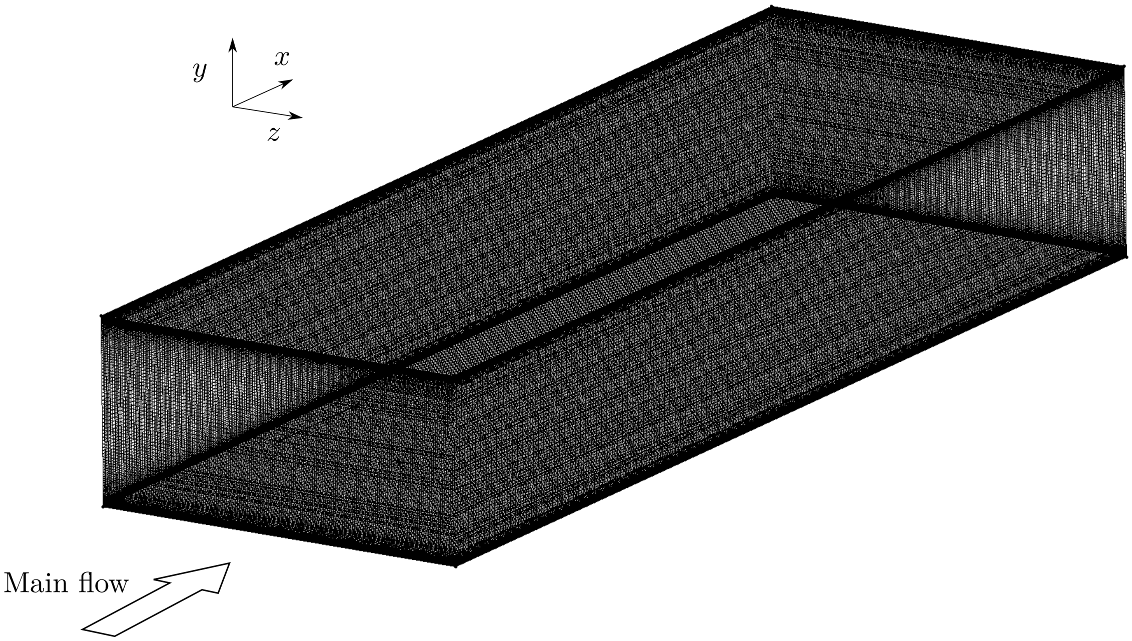

Figure 2.7: Smooth channel mesh.

an infinite domain. For this, a periodic condition is set for the x and z boundaries. In order to make the channel air flow continuously, the local pressure gradient $\partial p/\partial x$ in (2.6) can be divided into two parts in the momentum equation. One is the mean pressure p_{mean} which mainly drives the flow, and the fluctuating pressure gradient $\partial p_f/\partial x$ is variable as

$$\frac{\partial p}{\partial x} = \frac{\partial p_{\text{mean}}}{\partial x} + \frac{\partial p_f}{\partial x}. \tag{2.54}$$

Let $\beta_m = \partial p_{\text{mean}}/\partial x$ and $\dot{m}^n$ is the mass flow rate at time step n, so

$$\beta_m^{n+1} = \beta_m^n - \frac{1}{\Delta t}\left(\dot{m}^0 - 2\dot{m}^n + \dot{m}^{n-1}\right). \tag{2.55}$$

Expression (2.55) is used to keep the mass flow rate constant during computation. For the initial condition, a parabolic velocity profile is applied with random fluctuations. The parabolic velocity profile obeys

$$u^* = \frac{3}{2}u_b^*\left[1.0 - \left(\frac{y}{h}\right)^2\right]. \tag{2.56}$$

The case to be reproduced has the following conditions:

$$\begin{aligned} p^* &= 16065.05\text{Pa} \\ u_b^* &= 42.0\text{m/s} \\ T^* &= 110.0\text{K} \\ h^* &= 0.001\text{m}. \end{aligned} \tag{2.57}$$

These conditions are chosen so they coincide with the database of (Kim et al. (1987)), with the Reynolds number depending on friction velocity (Re_τ) and bulk velocity (Re_b) of

$$Re_\tau = \frac{u_\tau^* h^*}{\nu^*} = 180, \; Re_b = \frac{u_b^* h^*}{\nu^*} = 2800. \tag{2.58}$$

In the study of (Kim et al. (1987)), the velocity profile in the turbulent near-wall region is known and the friction coefficient is $c_f = 8.18 \times 10^{-3}$.

The channel flow mesh built to reproduce this case has a grid spacing of $\Delta x^+ = 8.84$, $\Delta z^+ = 4.49$ and Δy^+ varies from 0.2 at the wall to 4.13 at the channel centre. These magnitudes are scaled to be non-dimensional with viscous units i.e. friction velocity u_τ^* and

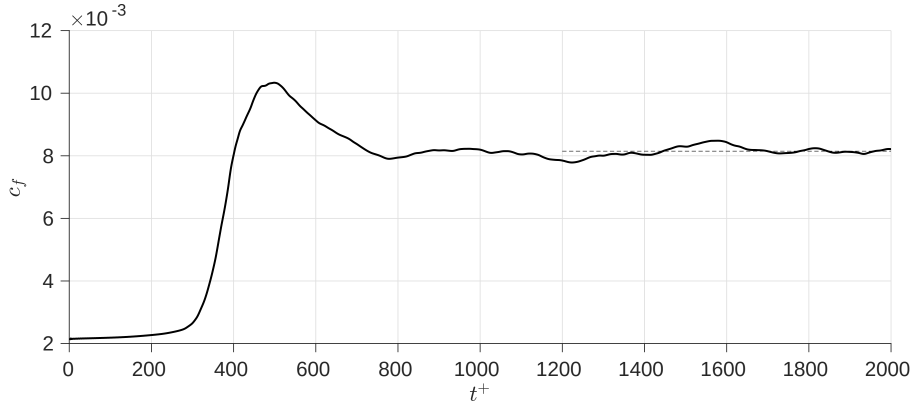

Figure 2.8: History of spatial-averaged c_f. The dashed line represents the mean between $t^+ = 1200 - 2000$.

kinematic viscosity $\nu^* = 1.5 \times 10^{-5}\, m^2/s$. This friction velocity is the result of the slope of the velocity at the wall and the value resulting from this simulation, $u^*_\tau = 2.7\, m/s$ is the one used to scale with respect to viscous units for this thesis[7]. The physical time step for the simulation is

$$\begin{aligned} \Delta t^* =& 5.144 \times 10^{-7}\text{s}, \\ \Delta t^+ =& \Delta t^* \times \rho^* u^{*2}_\tau / \mu^* = 0.25. \end{aligned} \tag{2.59}$$

The value of the time step is chosen according to the simulations with jets, which are explained in section 2.7. The results from Shefflow are presented in figure 2.8. It shows the history of c_f, which is spatially averaged on the top and bottom walls. Assuming that the flow is statistically convergent (variation of average quantities of less than 0.5%) from $t^+ \approx 1200$, taking a time-averaged value of c_f from $t^+ \approx 1200$ to $t^+ \approx 2000$, $c_f = 8.20 \times 10^{-3}$ which is very similar to the designed value.

When the simulation starts, the friction coefficient is very low, as the flow is starting and the friction comes from the parabolic profile. When time advances, the channel flow starts to evolve to the turbulent state, overshooting and finally settling into the turbulent regime entirely.

Furthermore, the time and spatial averaged velocity profile, the root-mean-square values of fluctuation velocities and the turbulent shear stress $-\langle u'v' \rangle / u^2_\tau$ are shown in figure 2.9.

---

[7] Except in chapter 5, where the friction velocity of other cases are used, which is specified within the chapter.

They are compared with the data from the database of Kim et al. (1987).

The results from the channel flow are very similar to those of the very fine DNS data from Kim et al. (1987), which validates the code and sets the starting point for the simulation of the active flow control.

2.6 Methodology and validations conclusion

The basics of CFD have been summarised in this chapter, focusing in the ones that the in-house solver Shefflow uses. Being a compressible code opens a wide range of possibilities to solve, from low speed to high speed flows. In section 2.7 and chapter 4, the main focus is DNS for incompressible flow, except for the flow inside the chamber, which has compressibility effects associated.

On the other hand, in Appendix B, compressible effects are very important because the case to be simulated is a transonic flight of a fuselage. Also, DNS cannot be used due to restrictions previously addressed. RANS is the main form of simulation that is used in this section.

Finally, the foundation of section 2.7 is laid here, as the flow field of the channel flow studied in section 2.5.3 is the starting point for the simulations with jets.

2.7 Wall Tangential Zero-Mass Jets

2.7.1 Introduction

Once the code has been validated, the wall tangential zero-mass jet (WT-ZMJ or ZMJ for short) case can be investigated. First, a non-dimensionalisation study is carried out in order to identify the important parameters and how they could affect the outcome of the simulation. Then, the problem is split in two separate studies: a channel flow, which is addressed in the following sections, where the boundary conditions are altered so they simulate the effects of the jets; and a chambers flow, which is explained in section 4.2, which contains the air movement inside the chamber due to the piston or membrane movement. This separation is possible under the assumption that the jet flow velocity is greater than the mean wall fluctuations. Therefore, the channel flow does not affect the flow inside the chambers. This fact implies that a one-way configuration can be adopted from the chamber flow to the channel flow.

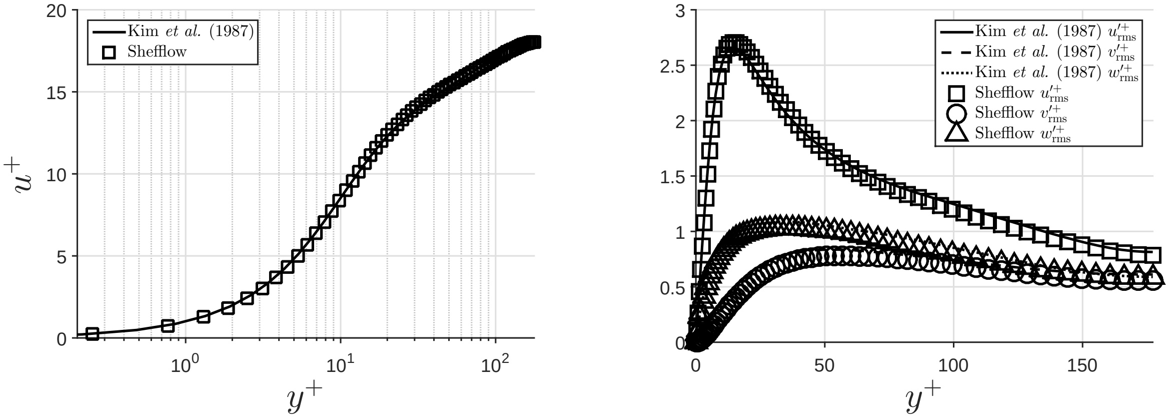

(a) Velocity profile in viscous units, u^+.

(b) Root-mean-square values of fluctuation velocities of $u'^+_{i,\mathrm{rms}}$.

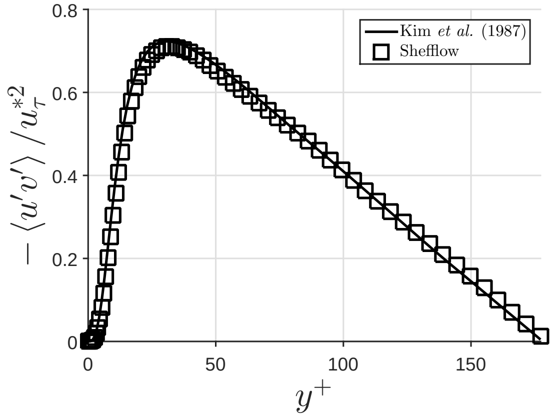

(c) Turbulent shear stress $- < u'v' > / u^{*2}_\tau$.

Figure 2.9: Values compared with the DNS database for a channel flow at $Re_\tau = 180$.

The problem was separated due to several implications. The first one was the computational resources, a large mesh is needed to properly simulate the DNS channel flow, and the exit velocity of the jet could be imposed as a boundary condition. Moreover, the channel mesh is a structured mesh whereas the chamber part is unstructured, which will make the solver even slower. The jet velocity can be simulated under the assumption of the exit flow from the jet being parabolic. This assumption will be studied further in section 4.2.

2.7.2 Non-dimensionalisation

Skin friction τ_w is the main concern of the analysis and therefore is the variable chosen for the Vaschy-Buckingham theorem (or Π theorem). The factors that play a role in the simulation are

$$\tau_w^* = \tau_w^* \left(\rho^*,\, u_b^*,\, h^*,\, \mu^*,\, \beta,\, U^*_{\text{jet,max}},\, T^*_{\text{osc}},\, L^*_{\text{step}},\, L^*_{\text{jet}},\, \delta^*_{\text{step}},\, \delta^*_{\text{jet}},\, L^*_{\text{piston}}\right) \tag{2.60}$$

where

- ρ^* is the density of the air,
- u_b^* is the bulk velocity, which is the spatial average velocity of the channel,
- h^* is the half-height of the channel,
- μ^* is the dynamic viscosity,
- β is the jet incidence angle,
- $U^*_{\text{jet,max}}$ is the maximum spatial average velocity at the jet[8] ,
- T^*_{osc} is the period of oscillation,
- L^*_{step} is the horizontal length of the step in the channel, hereinafter, the step wall,
- L^*_{jet} is the horizontal length of the channel that is at the bottom level of the jet, hereinafter, the jet wall,
- δ^*_{step} is the height from the jet wall to the step wall,
- δ^*_{jet} is the height from the jet wall to the top of the jet and,

---

[8] Although $U^*_{\text{jet,max}}$ is a parameter for the friction force, it is for the channel case in section 2.7.3. $U^*_{\text{jet,max}}$ is an outcome from section 4.2 since it is a function of the air displaced by the wall/membrane. First, the needed $U^*_{\text{jet,max}}$ has to be determined to tune the wall/membrane parameters.

- L^*_{piston} is the length of the membrane/piston wall (see figure 4.1).

All these magnitudes are sketched in figures 2.10 and 4.1 in their non-dimensional form.

The governing parameters chosen for the Π theorem are the density ρ^*, the bulk velocity u_b^* and the half-height of the channel h^*. Therefore, the parameters for the study are

$$\frac{\tau_w^*}{\frac{1}{2}\rho^* u_b^{*2}} = \frac{\tau_w^*}{\frac{1}{2}\rho^* u_b^{*2}}\left(\rho^*,\, u_b^*,\, h^*,\, \frac{\mu^*}{\rho^* u_b^* h^*},\, \beta,\, \frac{U^*_{\text{jet,max}}}{u_b^*},\, \frac{T^*_{\text{osc}}}{h^*/u_b^*},\, \frac{L^*_{\text{step}}}{h^*},\, \frac{L^*_{\text{jet}}}{h^*},\, \frac{\delta^*_{\text{step}}}{h^*},\, \frac{\delta^*_{\text{jet}}}{h^*},\, \frac{L^*_{\text{piston}}}{h^*}\right) \tag{2.61}$$

where the $\frac{1}{2}$ constant is added for historical reasons. The non-dimensional variables and parameters are

$$c_f = c_f\left(\rho^*,\, u_b^*,\, h^*, Re_b^{-1},\, \beta,\, U_{\text{jet,max}},\, T_{\text{osc}},\, L_{\text{step}},\, L_{\text{jet}},\, \delta_{\text{step}},\, \delta_{\text{jet}},\, L_{\text{piston}}\right) \tag{2.62}$$

In the literature (Jung et al. (1992); Quadrio and Ricco (2003, 2004)), some of these parameters are non-dimensionalised with respect to viscous units of the unperturbed channel case, i.e. $T^+_{\text{osc}} = \frac{T^*}{\nu^*/u_\tau^{*2}}$, $U^+_{\text{jet,max}} = \frac{U^*_{\text{jet,max}}}{u_\tau^*}$, $L^+_{\text{step}} = \frac{L^*_{\text{step}}}{\nu^*/u_\tau^*}$; in those cases, the superscript + will be written.

2.7.3 Channel case with Zero-Mass Jets

The oscillating wall (Quadrio et al. (2009b); Jung et al. (1992); Quadrio and Ricco (2003)) has been shown to obtain a considerable drag reduction. However, the implementation of an oscillating wall is very challenging for any vehicle surface. The idea of this new active flow control, the WT-ZMJ, is to blow air in the spanwise direction of the flow through slots, which are called jet exits. The direction of the jet flow could be altered to blow at a β angle from the perpendicular direction of the main flow.

With a slight modification of the model in section 2.5.3, slots are introduced in the channel to allocate the jets. The bottom and top wall have been modified so that the total volume of the channel is the same as the original channel, therefore, the distance from the centre to the jet wall L_{jet} is slightly larger than h^+ and the distance from the centre to the step wall L_{step} is slightly smaller than h^+, being the difference between the two δ^+_{step}.

Considering the air blown from the jets to the channel to be parabolic, the equation for the boundary condition of the jet flow entering or leaving the channel is

$$u_{\text{jet}} = -U_{\text{jet,max}} \sin\beta \sin\left(\frac{2\pi}{T_{\text{osc}}} t\right), \tag{2.63}$$

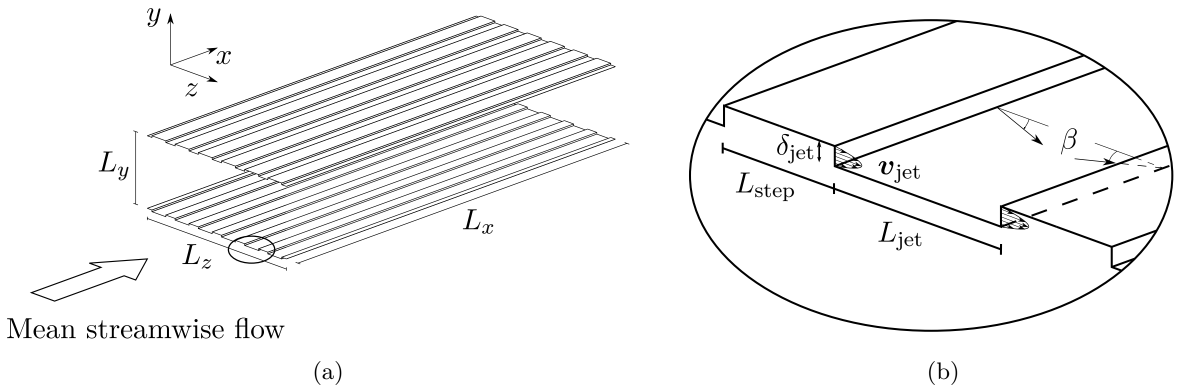

Figure 2.10: Sketch of the channel case and zoom of a pair of jets with some magnitudes and parameters from (2.62).

$$v_{\text{jet}} = 0, \tag{2.64}$$

$$w_{\text{jet}} = U_{\text{jet,max}} \cos\beta \sin\left(\frac{2\pi}{T_{\text{osc}}} t\right), \tag{2.65}$$

where $U_{\text{jet,max}}$ is the peak velocity at the centre throughout the period of oscillation T_{osc} at an angle β from the z-direction.

For the baseline simulation, there are 6 pair of jets on each wall with $L^+_{\text{jet}} = 90$ and $L^+_{\text{step}} = 36$ (or $L_{\text{jet}} = 0.5$ and $L_{\text{step}} = 0.2$). Figure 2.10 shows a schematic of the modified channel flow.

The model was created setting $\delta^+_{\text{jet}} = 2$. The wall area that has to be accounted for the friction force is the same as the one from the original channel case.

2.7.3.1 Modified channel with jets off

The introduction of new geometry instead of the smooth wall alters the behaviour of the flow in the channel. Before simulating the activation of the jets, it is interesting to obtain the modifications in the friction coefficient of this new geometry. For that, the boundary of the jets is set to symmetry conditions. After the mesh sensitivity[9], the parameters of this simulation are summarised in table 2.5. A cross section of a device is shown in figure 2.11 to visualise the mesh.

---

[9] This mesh sensitivity is performed for the modified channel of section 2.7.3.2, as the modified channel without jets converged earlier than with jets. Therefore, the finest mesh of the modified channel with jets on is used for jets off as well.

Parameter	Value	Parameter	Value
Re_b	2800	L_x^+	$4\pi h^+$
u_b	42 m/s	L_z^+	$4/3\pi h^+$
h^*	0.001 m	Δt^+	0.25
$U_{\text{jet,max}}$	0	Δx^+	8.84
δ_{jet}^+	2	Δy^+	$0.2 \sim 4.09$
L_{jet}^+	90	Δz^+	$0.5 \sim 3.80$
L_{step}^+	36	n_y	217
L_y^+	$2h^+$	n_z	504
T^*	110K		

Table 2.5: Simulation parameters. Left column gathers the parameters of the flow/channel and right column denotes numerical parameters of the simulation

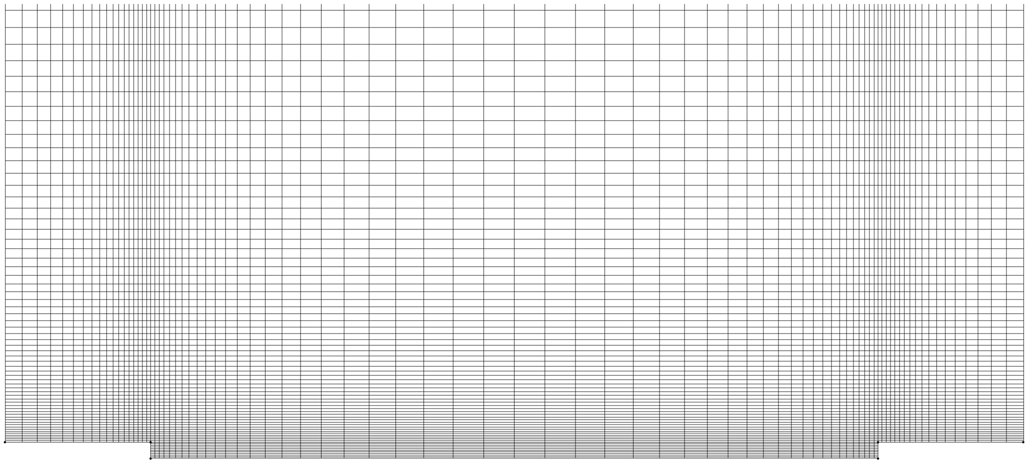

Figure 2.11: Rectilinear grid used to compute the Navier-Stokes equations. It corresponds to a cross section of one ZMJ device.

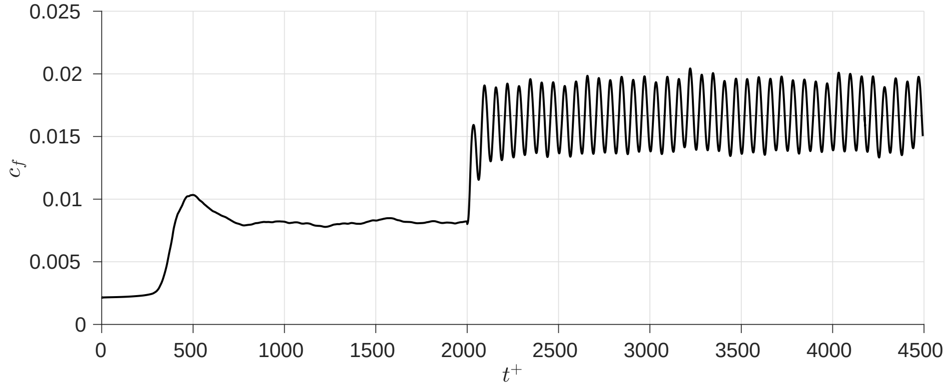

Figure 2.12: Evolution of friction coefficient before and after jet activation at $t^+ = 2000$ with $\beta = 0$.

The friction coefficient for the new geometry is 8.20×10^{-3}, which is similar to the simulation of the smooth channel case, only varying in less than 0.1%.

2.7.3.2 Baseline case with WT-ZMJ active

The jets are set to inject air at $\beta = 0\,\text{deg}$ at a mean parabolic velocity of $U^+_{\text{jet,max}} = 18$ at $T^+_{\text{osc}} = 125$. These values were chosen as a start following the literature from the oscillating wall (Jung et al. (1992); Quadrio and Ricco (2003, 2004)). The time step Δt chosen has to be fine enough to accurately represent an oscillation. For that, the period of oscillation is divided in 500 time steps, which leads to $\Delta t^+ = 0.25$. The history of the spatially averaged friction coefficient is shown in figure 2.12.

It can be seen that the jets stabilises very quickly as the momentum transfer is of the order of the main flow. For $\beta = 0$, the friction coefficient $c_f = 1.66 \times 10^{-2}$ which is more than the one produced by the channel without control. Since this is not the desired effect, some parameters should be changed.

There are four parameters that could drastically affect the friction coefficient: the incidence angle β, the maximum speed of the jets $U^+_{\text{jet,max}}$, the oscillation period T^+_{osc} and the jet wall L^+_{jet}. Although all parameters in (2.62) vary the friction coefficient, the four mentioned ones are thought to be the most influential.

The first parameter to be studied is the incidence angle β. A sweep between $\beta = 0$ and $\beta < 90\,\text{deg}$ is performed with all other parameters kept constant. This sweep was applied

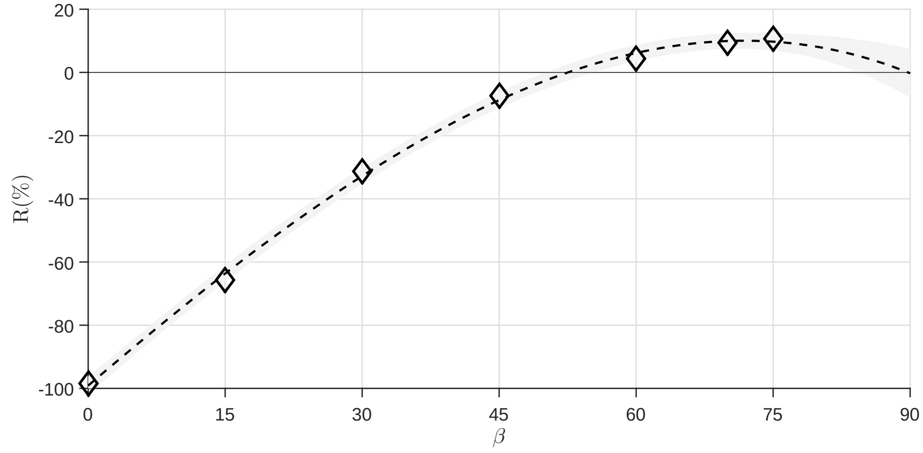

Figure 2.13: Sensitivity of reduction of c_f to changes in β. The dashed line corresponds to the third order trend line of the data and the shadowed area is an estimate of the standard deviation of the error in predicting a future value at another velocity.

in a coarser mesh and then refined for the mesh sensitivity analysis, which is reported in Appendix A. The results are shown in figure 2.13. A negative value in the reduction $R(\%) = \frac{c_f^{\text{unperturbed}} - c_f^{\text{jets}}}{c_f^{\text{unperturbed}}}$ means that the friction coefficient is increased.

The c_f reduction starts to be positive at around $\beta \approx 57\,\text{deg}$ and it tends to a maximum value around $\beta \approx 75\,\text{deg}$.

The case with maximum skin friction reduction from this study, when $\beta = 75\,\text{deg}$, is denoted as baseline. The evolution of friction coefficient for this case is shown in figure 2.14.

The mean friction coefficient with the jets with these parameters is $c_f = 7.32 \times 10^{-3}$, which is a 10.7% reduction from the unperturbed channel friction coefficient $c_f = 8.20 \times 10^{-3}$ in section 2.5.3.

The mean velocity profile of the two different walls of the channel are shown in figure 2.15. This non-conventional[10] way of representing the velocity profile is intended to show the twist Ω_z of the velocity profile that appears in figure 2.15b, which can be associated to the reduction in drag, as Choi et al. (1998) pointed out in figure 11. In figure 2.15a this twist is not shown, which means that there is no reduction coming from this wall. However, if an average of every wall surface is taken, there exists a reduction as can be seen in figure

---

[10] As opposed to the logarithmic x-axis for y^+ and regular y-axis for u^+, these figures are shown in the regular x-axis for the velocity scaled with outer units u and in the regular y-axis for y^+.

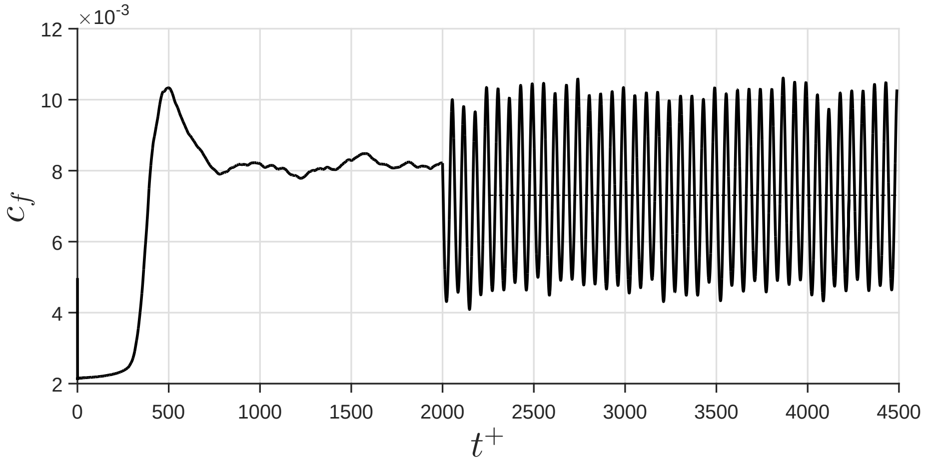

Figure 2.14: Evolution of friction coefficient before and after jet activation at $t^+ = 2000$ with $\beta = 75\,\mathrm{deg}$.

2.14. The air that travels slower from $y^+ = 0$ to $y^+ \approx 80$ in L_{jet} is displaced to higher y^+ positions due to conservation of mass. This is the reason why velocity is increased in higher y^+ positions above the jet wall and the entire step wall.

2.8 Conclusion

The baseline case of the Wall Tangential Zero-Mass Jets has been presented in this chapter. The case of section 2.7.3.2 is going to be further studied in the following chapters to understand where the friction reduction is coming from and what can be changed to increase the benefits the ZMJ provide. Most of the results reported in this chapter were obtained in collaboration with Xie (2019).

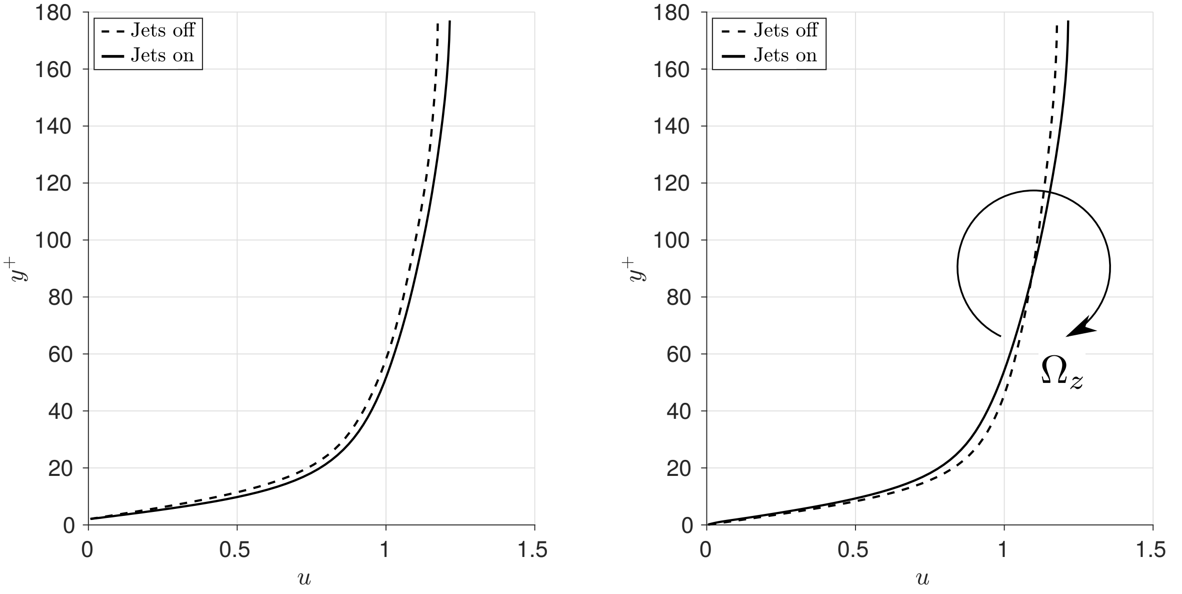

(a) Step wall, L_{step}.

(b) Jet wall, L_{jet}. The twist Ω_z of the velocity profile is highlighted.

Figure 2.15: Spatial and time averaged velocity profiles for the two different walls of the channel with jets on and off.

This page has been intentionally left blank.

Chapter 3

Extension of FIK analysis for flows with jet boundary conditions

3.1 Motivation

Fukagata et al. (2002) published a method to calculate the contributions to the skin friction coefficient for wall-bounded flows. This is referred as the FIK method. One of the main contributions is the Reynolds stress distribution, which is integrated prioritising the near-wall region with a linear weighting. They also used that method to calculate the friction with uniform blowing and suction perpendicular to the walls. However, the flow is uniform and a derivation is lacking for further research.

Since the analysis was limited to canonical cases, Peet and Sagaut (2009) extended it by allowing the inclusion of complex geometries like riblets. This is referred here as FIK-PS. The geometry could even change in the streamwise direction and be analysed with relative accuracy. This extension is only focused on flows with zero wall velocity and no transpiration like riblets. They studied different geometries of riblets obtaining good results when compared with those of Large Eddy Simulations (LES), with a difference of less than 4%.

The FIK technique has been used to study the potential reduction of skin friction in different scenarios such as riblets (Nakanishi et al. (2012)), super hydrophobic surfaces (Jelly et al. (2014) and Rastegari and Akhavan (2015)), oscillating wall (Hasegawa et al. (2014)), rotating discs (Ricco and Hahn (2013)) and steady jets (Yao et al. (2018)).

In Sumitani and Kasagi (1995), a similar simulation to that of Fukagata et al. (2002) was performed with uniform wall injection and suction to obtain a friction reduction. They found

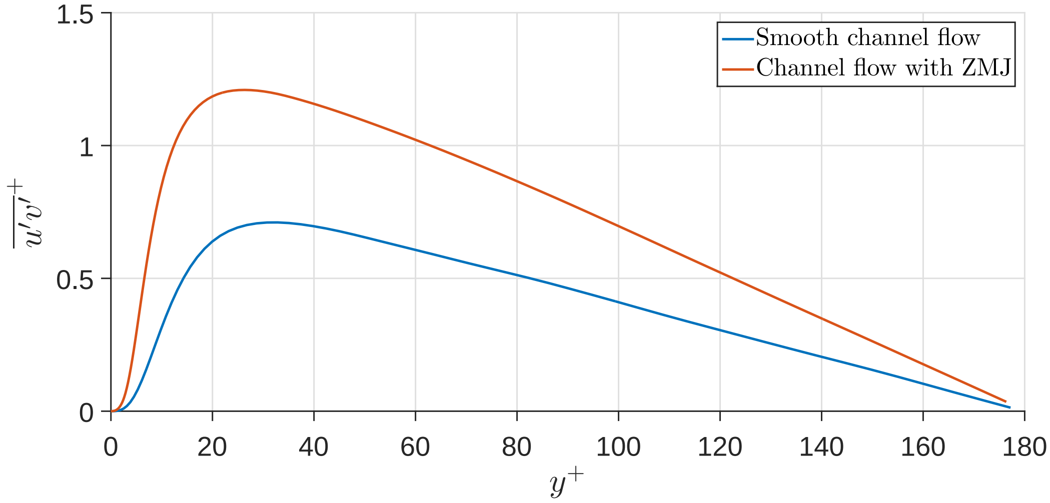

Figure 3.1: Reynolds stresses of the smooth channel flow and a temporal and spanwise average of the middle of the channel flow with ZMJ.

that the skin friction decreased by injection but increased by suction.

Opposition control was tested in DNS by Choi et al. (1994) in a channel flow and it was later adopted by Fukagata and Kasagi (2003) to a cylinder, applying the FIK to further investigate this active flow control system for canonical cases.

Later, Kametani and Fukagata (2011) performed simulations of a developing turbulent boundary layer with uniform injection and with uniform suction. They confirmed with the FIK that the former decreases the friction coefficient due to the convection term which includes the wall normal velocity.

In all cases, the reduction in drag was a consequence of the reduction in Reynolds stresses. However, for the case of the channel flow with ZMJ, even though a reduction in drag is achieved, the Reynolds stresses increase substantially. This difference in Reynolds stresses is represented in figure 3.1.

This is an unexpected result if only the Reynolds stresses are taken into account in the FIK method to calculate the friction coefficient. A further study on this counter-intuitive result is presented here.

3.1.1 Objective of the chapter

In this chapter, the contributions to the skin friction are extracted from flow field data by means of the FIK-E, an equation proposed in this thesis based on the original FIK. This equation deals with complex geometries as in the FIK-PS, and it adds the possibility to include boundary conditions such as jets, where the velocity can change in time. Moreover, the skin friction is analysed at every phase, to understand which mechanisms affect the skin friction at different moments.

In section 3.2, the equation with the inclusion of jets is derived, using the channel with jets cross section to visualise it better. However, the FIK-E can be applied to more general cases.

In section 3.3, the FIK-E is validated and tested with the baseline.

In section 3.4, all the contributions of the FIK-E are studied, focusing on their meaning to the skin friction.

3.1.2 Smooth channel flow friction decomposition

Fukagata et al. (2002) related the skin friction coefficient in a flat surface to the Reynolds stresses in the flow field. In this analysis, velocities are non-dimensionalised by the bulk velocity u_b^* (as opposed to $2u_b^*$ like in the original paper) and space is non-dimensionalised by h^*, the half channel height or boundary layer height. Superscript * refers to dimensional values, whereas its absence denotes values non-dimensionalised with respect to outer quantities (u_b^*, h^* and density ρ^*).

The starting point is to obtain the incompressible Reynolds averaged Navier-Stokes equations from the continuity and momentum equations:

$$\frac{\partial \rho^*}{\partial t^*} + \nabla \cdot (\rho^* \boldsymbol{v}^*) = 0, \tag{3.1}$$

$$\frac{\partial \rho^* \boldsymbol{v}^*}{\partial t^*} + \nabla \cdot \left(\rho^* \boldsymbol{v}^* \otimes \boldsymbol{v}^* + p^* \overline{\overline{I}} - \overline{\overline{\tau}} \right) = 0, \tag{3.2}$$

where $\boldsymbol{v}$ is the velocity vector, $\nabla \cdot$ is the divergence operator, $\otimes$ is the outer product, $\overline{\overline{I}}$ is the identity matrix and $\overline{\overline{\tau}}$ is the shear stress tensor. Assuming incompressible flow, the continuity equation (3.1) reduces to $\nabla \cdot \boldsymbol{v}^* = 0$ and the momentum equation in the x direction to

$$\frac{\partial u^*}{\partial t^*} + \frac{\partial u^* u^*}{\partial x^*} + \frac{\partial u^* v^*}{\partial y^*} + \frac{\partial u^* w^*}{\partial z^*} = -\frac{1}{\rho^*}\frac{\partial p^*}{\partial x^*} + \nu^* \left(\frac{\partial^2 u^*}{\partial x^{*2}} + \frac{\partial^2 u^*}{\partial y^{*2}} + \frac{\partial^2 u^*}{\partial z^{*2}} \right). \tag{3.3}$$

Again, the non-dimensionalisation is performed as $u = u^*/u_b^*$, $t = t^*/\left(h^*/u_b^*\right)$ and $x, y, z = x^*, y^*, z^*/h^*$, obtaining

$$\frac{\partial u}{\partial t} + \frac{\partial uu}{\partial x} + \frac{\partial uv}{\partial y} + \frac{\partial uw}{\partial z} = -\frac{\partial p}{\partial x} + \frac{1}{Re_b}\left(\frac{\partial^2 u}{\partial x^2} + \frac{\partial^2 u}{\partial y^2} + \frac{\partial^2 u}{\partial z^2} \right), \tag{3.4}$$

where p is pressure non-dimensionalised with $\rho^* u_b^{*^2}$ and $Re_b = u_b^* h^*/\nu^*$ is the Reynolds number. In order to obtain the Reynolds Averaged equations, one can divide the quantities in their ensemble average $\overline{()}$ in space and time and fluctuation $()'$; and average the result, leading to

$$-\frac{\partial \overline{p}}{\partial x} = \frac{\partial \overline{u'v'}}{\partial y} + \frac{\partial \overline{u'w'}}{\partial z} - \frac{1}{Re_b}\left(\frac{\partial^2 \overline{u}}{\partial y^2} + \frac{\partial^2 \overline{u}}{\partial z^2} \right) + \overline{I}_x + \frac{\partial \overline{u}}{\partial t}, \tag{3.5}$$

where t is time and the inhomogeneous terms are represented by

$$\overline{I}_x = \frac{\partial \bar{u}\bar{u}}{\partial x} + \frac{\partial \bar{u}\bar{v}}{\partial y} + \frac{\partial \bar{u}\bar{w}}{\partial z} + \frac{\partial \overline{u'u'}}{\partial x} - \frac{1}{Re_b}\frac{\partial^2 \overline{u}}{\partial x^2}. \tag{3.6}$$

Note that these averages are defined as ensemble averages, therefore they generally depend on time. The spanwise velocity w and derivatives with respect to z are zero in the original FIK as they worked with a smooth surface, statistically constant in the z direction. The steps to obtain the original FIK method are the following:

1. The first step is to integrate the x momentum equation, (3.5), over y to get the relation between the skin friction coefficient and other terms. Defining the skin friction coefficient as

$$C_f = \frac{2}{Re_b}\left.\frac{\partial \overline{u}}{\partial y}\right|_{y=0}, \tag{3.7}$$

the integration of (3.5) over y from the wall to the half height channel or boundary layer is

$$-\int_0^1 \frac{\partial \overline{p}}{\partial x}\mathrm{d}y = \int_0^1 \frac{\partial \overline{u'v'}}{\partial y}\mathrm{d}y - \frac{1}{Re_b}\int_0^1 \frac{\partial^2 \overline{u}}{\partial y^2}\mathrm{d}y + \int_0^1 \left(\overline{I}_x + \frac{\partial \overline{u}}{\partial t} \right)\mathrm{d}y,$$

$$-\int_0^1 \frac{\partial \overline{p}}{\partial x}\mathrm{d}y = \int_0^1 \mathrm{d}\overline{u'v'} - \frac{1}{Re_b}\int_0^1 \mathrm{d}\left(\frac{\partial \overline{u}}{\partial y}\right) + \int_0^1 \left(\overline{I}_x + \frac{\partial \overline{u}}{\partial t}\right)\mathrm{d}y, \tag{3.8}$$

with $\mathrm{d}\overline{u'v'}\Big|_{y=0} = \mathrm{d}\overline{u'v'}\Big|_{y=1} = 0$, $\frac{\partial \overline{u}}{\partial y}\Big|_{y=1} = 0$ and $\frac{\partial \overline{u}}{\partial y}\Big|_{y=0} = \frac{Re_b}{2}C_f$, one obtains

$$\frac{1}{2}C_f = -\int_0^1 \left(\frac{\partial \overline{p}}{\partial x} + \overline{I}_x + \frac{\partial \overline{u}}{\partial t}\right)\mathrm{d}y. \tag{3.9}$$

2. The resultant relation is merged with the x momentum equation in 3.5, obtaining

$$\frac{1}{2}C_f = \frac{\partial \overline{u'v'}}{\partial y} - \frac{1}{Re_b}\frac{\partial^2 \overline{u}}{\partial y^2} + \frac{\partial \overline{p}''}{\partial x} + \overline{I}_x'' + \frac{\partial \overline{u}''}{\partial t} \tag{3.10}$$

where the double prime on a quantity ψ represents that

$$\psi''(x,y,t) = \overline{\psi}(x,y,t) - \int_0^1 \overline{\psi}(x,y,t)\,\mathrm{d}y. \tag{3.11}$$

3. Then, a triple integration in the form $\int_0^{y_{\mathrm{top}}} \mathrm{d}y \int_0^y \mathrm{d}y \int_0^y \mathrm{d}y$ is applied to obtain with each integration: first, the force balance (as the first point, but as a function of y) in (3.12); second, the mean velocity profile; and third, the flow rate from the velocity profile. Note that $y_{\mathrm{top}} = h^*/h^* = 1$

First integration:

$$\int_0^y \frac{1}{2}C_f \mathrm{d}y = \int_0^y \frac{\partial \overline{u'v'}}{\partial y}\mathrm{d}y - \int_0^y \frac{1}{Re_b}\frac{\partial^2 \overline{u}}{\partial y^2}\mathrm{d}y + \int_0^y F''\mathrm{d}y$$

$$\frac{1}{2}C_f y = \overline{u'v'} - \left(\frac{1}{Re_b}\frac{\partial \overline{u}}{\partial y} - \frac{1}{2}C_f\right) + \int_0^y F''\mathrm{d}y$$

$$\frac{1}{2}C_f(y-1) = \overline{u'v'} - \frac{1}{Re_b}\frac{\partial \overline{u}}{\partial y} + \int_0^y F''\mathrm{d}y \tag{3.12}$$

Second integration:

$$\int_0^y \frac{1}{2}C_f(y-1)\,\mathrm{d}y = \int_0^y \overline{u'v'}\mathrm{d}y - \int_0^y \frac{1}{Re_b}\frac{\partial \overline{u}}{\partial y}\mathrm{d}y + \int_0^y\int_0^y F''\mathrm{d}y\mathrm{d}y$$

$$\frac{1}{2}C_f\left(\frac{y^2}{2} - y\right) = \int_0^y \overline{u'v'}\mathrm{d}y - \frac{1}{Re_b}\overline{u} + \int_0^y\int_0^y F''\mathrm{d}y\mathrm{d}y \tag{3.13}$$

Third integration:

$$\int_0^1 \frac{1}{2} C_f \left(\frac{y^2}{2} - y \right) \mathrm{d}y = \int_0^1 \int_0^y \overline{u'v'} \mathrm{d}y \mathrm{d}y - \int_0^1 \frac{1}{Re_b} \overline{u} \mathrm{d}y + \int_0^1 \int_0^y \int_0^y F'' \mathrm{d}y \mathrm{d}y \mathrm{d}y$$

$$C_f = \frac{6}{Re_b} - 6 \int_0^1 (1-y) \overline{u'v'} \mathrm{d}y + 6 \int_0^1 \int_0^y \int_0^y F'' \mathrm{d}y \mathrm{d}y \mathrm{d}y \tag{3.14}$$

where $F'' = \partial \overline{p}''/\partial x + \overline{I}_x'' + \partial \overline{u}''/\partial t$. The first term in the FIK equation is called in Fukagata et al. (2002) as laminar contribution, the second term is the turbulent contribution, and the third term is the sum of the pressure, inhomogeneous and transient contribution.

3.2 Derivation of the equation

In order to extend the FIK method for a complex surface, the procedure developed by Peet and Sagaut (2009) is used. For clarity, (3.5) is rewritten as

$$I_t + I_v = -\left(I_x + \frac{\partial \overline{p}}{\partial x} + \frac{\partial \overline{u}}{\partial t} \right), \tag{3.15}$$

where the crossflow turbulent and viscous terms I_t and I_v are

$$I_t = \frac{\partial \overline{u'v'}}{\partial y} + \frac{\partial \overline{u'w'}}{\partial z}, \tag{3.16}$$

$$I_v = -\frac{1}{Re_b} \left(\frac{\partial^2 \overline{u}}{\partial y^2} + \frac{\partial^2 \overline{u}}{\partial z^2} \right). \tag{3.17}$$

Contrary to the original FIK, in the FIK-PS and in the extension proposed in this thesis, FIK-E, the contributions from the spanwise velocities and derivatives are kept in the sum of the convective terms and streamwise turbulent and viscous stresses I_x in (3.6).

Step 1 in section 3.1.2 is applied for a complex shape with jets. To visualise it better and have an example of the procedure, the channel flow with jets is used (Figure 2.10).

A laminar parabolic jet is assumed for the boundary condition with a velocity at the centre which follows (2.63)–(2.65), repeated here for convenience,

$$u_{\text{jet}} = -U_{\text{jet,max}} \sin \beta \sin \left(\frac{2\pi}{T_{\text{osc}}} t \right), \tag{3.18}$$

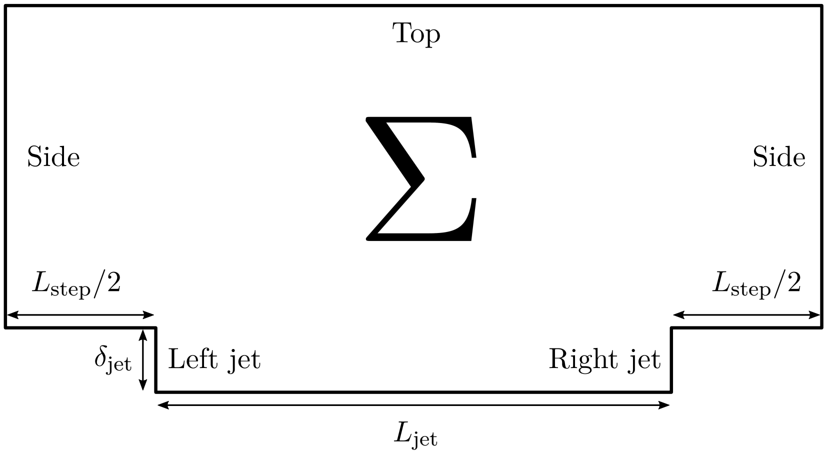

Figure 3.2: Schematic of the cross section of the channel (Not to scale).

$$v_{\text{jet}} = 0, \tag{3.19}$$

$$w_{\text{jet}} = U_{\text{jet,max}} \cos\beta \sin\left(\frac{2\pi}{T_{\text{osc}}} t\right), \tag{3.20}$$

where $U_{\text{jet,max}}$ is the peak velocity module at the centre of the jet throughout the period of oscillation T_{osc} and β is the angle at which the jet injects/extracts air to/from the channel.

The cross section of the channel to be studied with this analysis is the one in figure 3.2. The horizontal bottom surfaces are walls; the vertical bottom surfaces are jets that blow/suck air at an angle β such as $u_{\text{jet}_l} = -u_{\text{jet}_r}$ and $w_{\text{jet}_l} = w_{\text{jet}_r}$, where the subscript l and r are for the left and right jet, respectively; the left and right surfaces are periodic surfaces; and the top surface is an imaginary top surface where the flow is considered uniform, which in the case of the channel flow studied is the centre of the channel (in the case of an open boundary layer flow, this surface would be the end of the boundary layer).

In order to obtain the average skin friction coefficient for the cross section, the section average of (3.15) is taken as

$$\frac{1}{A_\Sigma} \iint_\Sigma \left(\underbrace{I_t}_{\text{(a)}} + \underbrace{I_v}_{\text{(b)}} \right) \mathrm{d}y \mathrm{d}z = -\frac{1}{A_\Sigma} \iint_\Sigma \left(\underbrace{I_x + \frac{\partial \overline{p}}{\partial x} + \frac{\partial \overline{u}}{\partial t}}_{\text{(c)}} \right) \mathrm{d}y \mathrm{d}z, \tag{3.21}$$

where A_Σ is the area of the cross section and the different parts (a-c) are developed next. The divergence theorem[1] is used to transform surface integrals in (a) and (b) into line integrals. As defined in FIK-PS, the variable use to traverse the line enclosing a surface is γ.

(a) Crossflow turbulent average.

$$\frac{1}{A_\Sigma}\iint_\Sigma I_t \mathrm{d}y\mathrm{d}z = \frac{1}{A_\Sigma}\iint_\Sigma \left(\frac{\partial \overline{u'v'}}{\partial y} + \frac{\partial \overline{u'w'}}{\partial z}\right)\mathrm{d}y\mathrm{d}z = \frac{1}{A_\Sigma}\oint_{\mathrm{d}\Sigma}\left(\overline{u'v'}\vec{\boldsymbol{j}} + \overline{u'w'}\vec{\boldsymbol{k}}\right)\cdot \boldsymbol{n}\mathrm{d}\gamma$$

$$= \frac{1}{A_\Sigma}\oint_{\mathrm{d}\Sigma}\overline{u'v'_{n_\Sigma}}\mathrm{d}\gamma = \oint_{\mathrm{d}\Sigma_w + \mathrm{d}\Sigma_{\mathrm{jets}} + \mathrm{d}\Sigma_{\mathrm{sides}} + \mathrm{d}\Sigma_{\mathrm{top}}}\overline{u'v'_{n_\Sigma}}\mathrm{d}\gamma = 0, \tag{3.23}$$

where n_Σ is the normal component to the domain Σ pointing outwards. All the components of the last integral are zero. Velocity at the walls is zero, the jets are assumed to be laminar (no fluctuations), the sides cancel each other out and velocity at the top surface is considered uniform.

(b) Viscous average.

$$\frac{1}{A_\Sigma}\iint_\Sigma I_v \mathrm{d}y\mathrm{d}z = -\frac{1}{A_\Sigma}\frac{1}{Re_b}\iint_\Sigma\left(\frac{\partial^2 \overline{u}}{\partial y^2} + \frac{\partial^2 \overline{u}}{\partial z^2}\right)\mathrm{d}y\mathrm{d}z$$

$$= -\frac{1}{A_\Sigma}\frac{1}{Re_b}\oint_{\mathrm{d}\Sigma}\left(\frac{\partial \overline{u}}{\partial y}\boldsymbol{j} + \frac{\partial \overline{u}}{\partial z}\boldsymbol{k}\right)\cdot \boldsymbol{n}\mathrm{d}\gamma = -\frac{1}{A_\Sigma}\frac{1}{Re_b}\oint_{\mathrm{d}\Sigma}\frac{\partial \overline{u}}{\partial \boldsymbol{n}_\Sigma}\mathrm{d}\gamma$$

$$= -\frac{1}{A_\Sigma}\frac{1}{Re_b}\left(\int_{\mathrm{d}\Sigma_w}\frac{\partial \overline{u}}{\partial \boldsymbol{n}_\Sigma}\mathrm{d}\gamma + \int_{\mathrm{d}\Sigma_{\mathrm{jet}_l}}\frac{\partial \overline{u}}{\partial \boldsymbol{n}_\Sigma}\mathrm{d}\gamma + \int_{\mathrm{d}\Sigma_{\mathrm{jet}_r}}\frac{\partial \overline{u}}{\partial \boldsymbol{n}_\Sigma}\mathrm{d}\gamma + \int_{\mathrm{d}\Sigma_{\mathrm{top}} + \mathrm{d}\Sigma_{\mathrm{sides}}}\frac{\partial \overline{u}}{\partial \boldsymbol{n}_\Sigma}\mathrm{d}\gamma\right)$$

$$= \frac{1}{A_\Sigma}\left(\frac{s_w}{2}C_f^z + \frac{s_{\mathrm{jet}}}{2}C_{\mathrm{jet}_l}^z + \frac{s_{\mathrm{jet}}}{2}C_{\mathrm{jet}_r}^z\right), \tag{3.24}$$

where $\boldsymbol{j}$ and $\boldsymbol{k}$ are the unit vectors in y and z directions; and the coefficients shown in the last step of (3.24) are defined in (3.25) and (3.26). The gradient of the top segment is zero due to uniformity of the flow and the sides cancel each other out. Note that

---

[1] The divergence theorem reads as

$$\iint_\Sigma \nabla\cdot \boldsymbol{F}\mathrm{d}\sigma = \oint_{\mathrm{d}\Sigma}\boldsymbol{F}\cdot \boldsymbol{n}\mathrm{d}\gamma, \tag{3.22}$$

where $\boldsymbol{F}$ is any vector, $\boldsymbol{n}$ is the normal vector pointing outwards from the surface Σ and $\mathrm{d}\gamma$ denotes the differential of the closed contour $\mathrm{d}\Sigma$.

$C^z_{\mathrm{jet}_l} \neq C^z_{\mathrm{jet}_r}$, which is explained in section 3.4.4 and

$$C^z_\psi = \frac{1}{s_\psi} \int_\psi C_\psi(\gamma) \mathrm{d}\gamma, \tag{3.25}$$

$$C_\psi = -\frac{2}{Re_b} \left. \frac{\partial \overline{u}}{\partial \boldsymbol{n}_\Sigma} \right|_\psi, \tag{3.26}$$

where the subscript ψ can be substituted by either f to represent the skin friction coefficient C_f or jet_l or jet_r to represent the left or right jet coefficient, C_{jet_l} or C_{jet_r}, respectively. The superscript z represents the ensemble average over the line s_ψ, which can be the wall line s_w in the case of the skin friction coefficient or the jet line s_{jet} in the case of either jet coefficients. A minus sign is introduced in (3.26) because the gradient direction of the skin friction coefficient is contrary to the normal surface vector $\boldsymbol{n}_\Sigma$. For the sake of consistency, the jet coefficients follow the same criteria.

(c) Convective terms, streamwise turbulent and viscous stresses terms; pressure gradient and temporal term. For now, these integrals are left as surface integrals.

After the derivations of the average of (3.21), (3.27) is obtained,

$$\begin{aligned}\frac{s_w}{2A_\Sigma} C^z_f = &-\frac{1}{A_\Sigma} \iint_\Sigma I_x \mathrm{d}y\mathrm{d}z - \frac{1}{A_\Sigma} \iint_\Sigma \frac{\partial \overline{p}}{\partial x} \mathrm{d}y\mathrm{d}z - \frac{1}{A_\Sigma} \iint_\Sigma \frac{\partial \overline{u}}{\partial t} \mathrm{d}y\mathrm{d}z \\ &- \frac{s_{\mathrm{jet}}}{2A_\Sigma} \left(C^z_{\mathrm{jet}_l} + C^z_{\mathrm{jet}_r} \right). \end{aligned} \tag{3.27}$$

This equation represents the balance of friction forces, momentum in/out due to jets, the pressure gradient and the jet actuation needed to move the flow.

Step 2 in section 3.1.2 is applied now. Equation (3.15) is subtracted from (3.27) resulting in

$$\frac{s_w}{2A_\Sigma} C^z_f = I_t + I_v + I''_x + \frac{\partial \overline{p}''}{\partial x} + \frac{\partial \overline{u}''}{\partial t} - \frac{s_{\mathrm{jet}}}{2A_\Sigma} \left(C^z_{\mathrm{jet}_l} + C^z_{\mathrm{jet}_r} \right), \tag{3.28}$$

where $\psi''(x,y,z,t) = \psi(x,y,z,t) - 1/A_\Sigma \iint_\Sigma \psi(x,y,z,t)\, \mathrm{d}y\mathrm{d}z$. Note that this last definition includes the z direction from the original definition in (3.10) and therefore, the integration is in A_Σ instead of only y.

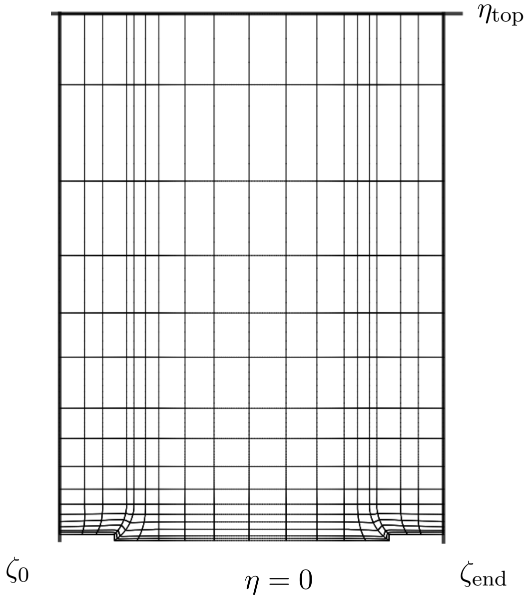

Figure 3.3: Body-fitted curvilinear coordinate system (η, ζ) of the channel with ZMJ cross section. This is a less condensed version of the one used.

3.2.1 Body fitted coordinates

In the original FIK analysis the simulation domain could be reduced to a single line, but it is not the case for a cross section of this geometry. For that, elementary surfaces $\sigma(\eta, \zeta)$ have to be integrated in η instead of over a line in y and then, integrated along ζ in the section. The elementary surfaces used by FIK-PS are adopted and are defined as

$$\sigma(\eta, \zeta) = \left\{(y, z) : \eta\left(y, z\right) \in \left(0, \eta\right), \zeta\left(y, z\right) \in \left(\zeta, \zeta + \mathrm{d}\zeta\right)\right\}. \tag{3.29}$$

It is assumed that $\mathrm{d}\zeta$ is infinitesimally small. For the example of the channel flow with jets, ζ travels from the leftmost wall in figure 3.2 to the rightmost wall along the jet lines and the bottom wall. The elementary surfaces for the cross section of figure 2.10 are shown in figure 3.3. A zoom of the jet exit elementary surfaces is shown in figure 3.4.

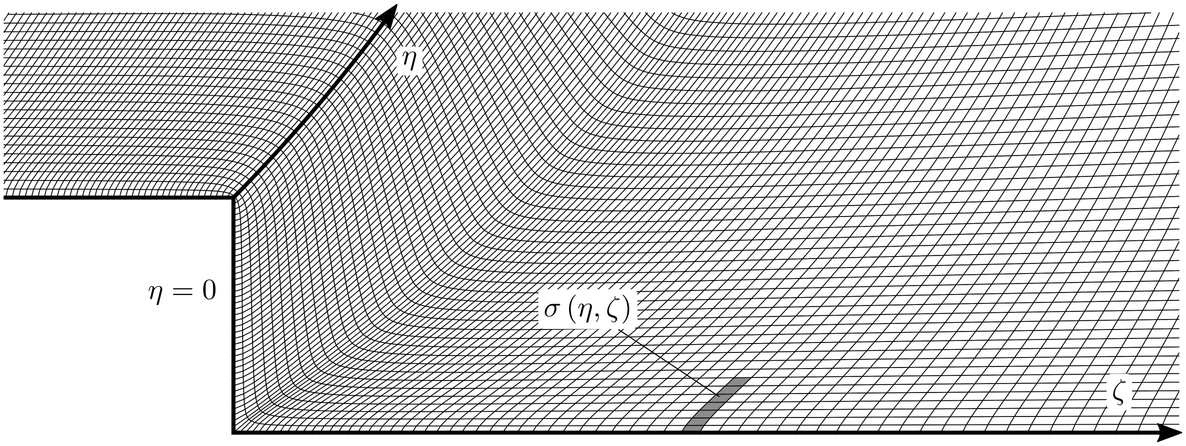

Figure 3.4: Zoom of the body-fitted curvilinear coordinate system (η, ζ) of the channel with ZMJ cross section. The shadowed area represents the elementary surface at a certain η and ζ.

3.2.2 FIK-E in body fitted coordinates

Once body fitted coordinates are defined, the first integral of step 3 can be applied, which in the case of a complex surface is an elementary surface integral as

$$\frac{s_w}{2A_\Sigma}\underbrace{\iint_\sigma C_f^z \mathrm{d}\eta\mathrm{d}\zeta}_{\text{(a)}} = \iint_\sigma \left(\underbrace{I_t}_{\text{(b)}} + \underbrace{I_v}_{\text{(c)}}\right)\mathrm{d}\eta\mathrm{d}\zeta + \iint_\sigma \left(\underbrace{I''_x}_{\text{(d)}} + \underbrace{\frac{\partial \overline{p}''}{\partial x}}_{\text{(e)}} + \underbrace{\frac{\partial \overline{u}''}{\partial t}}_{\text{(f)}}\right)\mathrm{d}\eta\mathrm{d}\zeta$$

$$- \frac{s_{\text{jet}}}{2A_\Sigma}\underbrace{\iint_\sigma \left(C^z_{\text{jet}_l} + C^z_{\text{jet}_r}\right)\mathrm{d}\eta\mathrm{d}\zeta}_{\text{(a)}}, \tag{3.30}$$

and the different parts (a-f) are developed next. Again, the divergence theorem is used to transform some surface integrals into line integrals.

(a) Friction and jet coefficients.

$$\iint_\sigma C^z_\psi \mathrm{d}\eta\mathrm{d}\zeta = C^z_\psi dA_\sigma, \tag{3.31}$$

where ψ is either f, jet_l or jet_r, corresponding to the wall or either of the jets. Note that integrals of either coefficient over elements which do not correspond to their boundary are zero, and they are constant over the elements which correspond to their boundary ($C^z_{\mathrm{jet}_l}$ over a wall or the right jet is zero but it has a constant value over the left jet as it only appears in integrals of elements with the left jet at $\eta = 0$).

(b) Crossflow turbulent component.

$$\iint_\sigma I_t \mathrm{d}\eta \mathrm{d}\zeta = \iint_\sigma \left(\frac{\partial \overline{u'v'}}{\partial y} + \frac{\partial \overline{u'w'}}{\partial z} \right) \mathrm{d}\eta \mathrm{d}\zeta$$

$$= \oint_{\mathrm{d}\sigma} \left(\overline{u'v'}\boldsymbol{j} + \overline{u'w'}\boldsymbol{k} \right) \cdot \boldsymbol{n} \mathrm{d}\gamma = \oint_{\mathrm{d}\sigma} \overline{u'v'_{n_\sigma}} \mathrm{d}\gamma$$

$$= \oint_{\mathrm{d}\sigma_w + \mathrm{d}\sigma_{\mathrm{jets}} + \mathrm{d}\sigma_{\mathrm{sides}} + \mathrm{d}\sigma_{\mathrm{top}}} \overline{u'v'_{n_\sigma}} \mathrm{d}\gamma = \int_{\mathrm{d}\sigma_{\mathrm{top}}} \overline{u'v'_{n_\sigma}} \mathrm{d}\zeta. \tag{3.32}$$

As before, there is no velocity fluctuations at the wall or the jets. The contributions on the sides cancel out because $\mathrm{d}\zeta$ is infinitesimally small. In this case however, the top line is not zero as it depends on η. Note that the integral accounts for both wall and jet contributions. This is just to take into account both cell possibilities but it would never be found at the same time in the study case proposed.

(c) Viscous component.

$$\iint_\sigma I_v \mathrm{d}\eta \mathrm{d}\zeta = -\frac{1}{Re_b} \iint_\sigma \left(\frac{\partial^2 \overline{u}}{\partial y^2} + \frac{\partial^2 \overline{u}}{\partial z^2} \right) \mathrm{d}\eta \mathrm{d}\zeta$$

$$= -\frac{1}{Re_b} \oint_{\mathrm{d}\sigma} \left(\frac{\partial \overline{u}}{\partial y}\boldsymbol{j} + \frac{\partial \overline{u}}{\partial z}\boldsymbol{k} \right) \cdot \boldsymbol{n} \mathrm{d}\gamma = -\frac{1}{Re_b} \oint_{\mathrm{d}\sigma} \frac{\partial \overline{u}}{\partial \boldsymbol{n}_\sigma} \mathrm{d}\gamma$$

$$= -\frac{1}{Re_b} \left(\int_{\mathrm{d}\sigma_w} \frac{\partial \overline{u}}{\partial \boldsymbol{n}_\sigma} \mathrm{d}\gamma + \int_{\mathrm{d}\sigma_{\mathrm{jet}_l}} \frac{\partial \overline{u}}{\partial \boldsymbol{n}_\sigma} \mathrm{d}\gamma + \int_{\mathrm{d}\sigma_{\mathrm{jet}_r}} \frac{\partial \overline{u}}{\partial \boldsymbol{n}_\sigma} \mathrm{d}\gamma + \int_{\mathrm{d}\sigma_{\mathrm{top}} + \mathrm{d}\sigma_{\mathrm{sides}}} \frac{\partial \overline{u}}{\partial \boldsymbol{n}_\sigma} \mathrm{d}\gamma \right). \tag{3.33}$$

Equation (3.33) accounts for both wall and jet contributions as well. If the cell to integrate starts on the wall, the first term is used; if the cell starts on either of the jets, the second or third terms are used. However, no matter where it starts, the last term (the top of the cell) is always present. As for the side segments, they cancel each other out. The different possibilities are addressed in (3.34) and (3.35). In order to simplify the equations, the distribution function $w_\psi(\zeta) = C_\psi(\gamma)/C_\psi^z$ is introduced as

- Wall cells

$$\int_{\mathrm{d}\sigma_w} \frac{\partial \overline{u}}{\partial \boldsymbol{n}_\sigma} \mathrm{d}\zeta = -\frac{Re_b}{2} \int_{\mathrm{d}\sigma_w} C_f(\zeta)\mathrm{d}\zeta = -\frac{Re_b}{2} C_f^z \int_{\mathrm{d}\sigma_w} w_w(\zeta)\mathrm{d}\zeta, \tag{3.34}$$

- Jet cells

$$\int_{\mathrm{d}\sigma_{\mathrm{jet}_i}} \frac{\partial \overline{u}}{\partial \boldsymbol{n}_\sigma} \mathrm{d}\zeta = -\frac{Re_b}{2} \int_{\mathrm{d}\sigma_{\mathrm{jet}_i}} C_{\mathrm{jet}_i}(\zeta)\mathrm{d}\zeta = -\frac{Re_b}{2} C_{\mathrm{jet}_i}^z \int_{\mathrm{d}\sigma_{\mathrm{jet}_i}} w_{\mathrm{jet}_i}(\zeta)\mathrm{d}\zeta. \tag{3.35}$$

(d) (e) and (f) Convective terms, streamwise turbulent and viscous stresses; Pressure gradient term; and temporal term are kept as surface integrals. In the case of a channel flow, with a constant pressure gradient, the mean pressure is the same everywhere in the section. Therefore, this Pressure gradient term is zero. In the case of an open boundary condition, this term would be kept.

Substituting (3.31)–(3.33) into (3.30), the following is obtained:

$$\begin{aligned}\frac{s_w}{2A_\Sigma} C_f^z dA_\sigma = &\int_{\mathrm{d}\sigma_{\mathrm{top}}} \overline{u'v'_{n_\sigma}} \mathrm{d}\zeta + \frac{1}{2} C_f^z \int_{\mathrm{d}\sigma_w} w_w(\zeta)\mathrm{d}\zeta + \sum_{i=1}^{N_j} \left[\frac{1}{2} C_{\mathrm{jet}_i}^z \int_{\mathrm{d}\sigma_{\mathrm{jet}_i}} w_{\mathrm{jet}_i}(\zeta)\mathrm{d}\zeta\right] \\ &- \frac{1}{Re_b} \int_{\mathrm{d}\sigma_{\mathrm{top}}} \frac{\partial \overline{u}}{\partial \boldsymbol{n}_\sigma} \mathrm{d}\zeta + \iint_\sigma \left(I''_x + \frac{\partial \bar{u}''}{\partial t}\right) \mathrm{d}\eta \mathrm{d}\zeta - \frac{s_{\mathrm{jet}}}{2A_\Sigma} \sum_{i=1}^{N_j} C_{\mathrm{jet}_i}^z dA_\sigma,\end{aligned} \tag{3.36}$$

where N_j is the number of jets, in this case, 2, which are the left and right ones. Solving for C_f^z,

$$\begin{aligned}\frac{1}{2} C_f^z \int_{\mathrm{d}\sigma_w} w_w(\zeta)\mathrm{d}\zeta - \frac{s_w}{2A_\Sigma} C_f^z dA_\sigma = &\frac{1}{Re_b} \int_{\mathrm{d}\sigma_{\mathrm{top}}} \frac{\partial \overline{u}}{\partial \boldsymbol{n}_\sigma} \mathrm{d}\zeta - \int_{\mathrm{d}\sigma_{\mathrm{top}}} \overline{u'v'_{n_\sigma}} \mathrm{d}\zeta \\ - \sum_{i=1}^{N_j} \left[\frac{1}{2} C_{\mathrm{jet}_i}^z \int_{\mathrm{d}\sigma_{\mathrm{jet}_i}} w_{\mathrm{jet}_i}(\zeta)\mathrm{d}\zeta\right] + \frac{s_{\mathrm{jet}}}{2A_\Sigma} \sum_{i=1}^{N_j} C_{\mathrm{jet}_i}^z dA_\sigma &- \iint_\sigma \left(I''_x + \frac{\partial \bar{u}''}{\partial t}\right) \mathrm{d}\eta \mathrm{d}\zeta,\end{aligned} \tag{3.37}$$

and rearranging the terms,

$$\frac{1}{2} C_f^z s_w \int_{\mathrm{d}\sigma_w} \left[w_w(\zeta) \frac{\mathrm{d}\zeta}{s_w} - \frac{\eta \mathrm{d}\zeta}{A_\Sigma}\right] = \frac{1}{Re_b} \int_{\mathrm{d}\sigma_{\mathrm{top}}} \frac{\partial \overline{u}}{\partial \boldsymbol{n}_\sigma} \mathrm{d}\zeta - \int_{\mathrm{d}\sigma_{\mathrm{top}}} \overline{u'v'_{n_\sigma}} \mathrm{d}\zeta$$

$$-\sum_{i=1}^{N_j}\left\{\frac{1}{2}C^z_{\mathrm{jet}_i}s_{\mathrm{jet}}\int_{\mathrm{d}\sigma_{\mathrm{jet}_i}}\left[w_{\mathrm{jet}_i}(\zeta)\frac{\mathrm{d}\zeta}{s_{\mathrm{jet}}}-\frac{\eta\mathrm{d}\zeta}{A_\Sigma}\right]\right\}-\iint_\sigma\left(I''_x+\frac{\partial\bar{u}''}{\partial t}\right)\mathrm{d}\eta\mathrm{d}\zeta. \tag{3.38}$$

As pointed out at the beginning of this section, the elementary surfaces have to be summed in ζ as well. Since $\mathrm{d}\zeta$ is infinitesimally small, all integrals of the type $\int_\sigma \mathrm{d}\zeta$ in the ζ direction become $\mathrm{d}\zeta$. Therefore, (3.38), which is the result of the integration up to the first integral of step 3 in the original FIK method, becomes (3.39). Moreover, $\boldsymbol{n}_\sigma$ has been replaced with η because $\boldsymbol{n}_\sigma$ at the top of the cell points in the same direction as η, which yields

$$\frac{1}{2}C^z_f s_w\int_{\zeta_w}\left[w_w(\zeta)\frac{\mathrm{d}\zeta}{s_w}-\frac{\eta\mathrm{d}\zeta}{A_\Sigma}\right]=\frac{1}{Re_b}\int_\zeta\frac{\partial\overline{u}}{\partial\eta}\mathrm{d}\zeta-\int_\zeta\overline{u'v'_\eta}\mathrm{d}\zeta$$

$$-\sum_{i=1}^{N_j}\left\{\frac{1}{2}C^z_{\mathrm{jet}_i}s_{\mathrm{jet}}\int_{\zeta_{\mathrm{jet}_i}}\left[w_{\mathrm{jet}_i}(\zeta)\frac{\mathrm{d}\zeta}{s_{\mathrm{jet}}}-\frac{\eta\mathrm{d}\zeta}{A_\Sigma}\right]\right\}-\int_\zeta\int_0^\eta\left(I''_x+\frac{\partial\bar{u}''}{\partial t}\right)\mathrm{d}\eta\mathrm{d}\zeta. \tag{3.39}$$

A double integration of the form $\int_0^{\eta_{\mathrm{top}}}\mathrm{d}\eta\int_0^\eta\mathrm{d}\eta$ is applied for the next step (which corresponds to the last two integrals of step 3). To solve the double integral, integration by parts is used following Fukagata (2004). A general quantity $\psi(\eta)$ inside the double integral $\int_0^{\eta_{\mathrm{top}}}\mathrm{d}\eta\int_0^\eta\mathrm{d}\eta$ is solved using integration by parts as

$$\int_0^{\eta_{\mathrm{top}}}\int_0^\eta\psi\mathrm{d}\eta\mathrm{d}\eta=\int_0^{\eta_{\mathrm{top}}}\left(\int_0^\eta\psi\mathrm{d}\eta\right)\mathrm{d}\eta$$

$$=\left[\eta\int_0^\eta\psi\mathrm{d}\eta\right]_0^{\eta_{\mathrm{top}}}-\int_0^{\eta_{\mathrm{top}}}\eta\psi\mathrm{d}\eta=\int_0^{\eta_{\mathrm{top}}}\left(\eta_{\mathrm{top}}-\eta\right)\psi\mathrm{d}\eta, \tag{3.40}$$

and similarly, in the case a triple integral is found in the form $\int_0^{\eta_{\mathrm{top}}}\mathrm{d}\eta\int_0^\eta\mathrm{d}\eta\int_0^\eta\mathrm{d}\eta$, the result is $\int_0^{\eta_{\mathrm{top}}}\frac{1}{2}\left(\eta_{\mathrm{top}}-\eta\right)^2\psi\mathrm{d}\eta$. The equation to develop is the following:

$$\frac{1}{2}C^z_f s_w\underbrace{\int_0^{\eta_{\mathrm{top}}}\int_0^\eta\int_{\zeta_w}\left[w_w(\zeta)\frac{\mathrm{d}\zeta}{s_w}-\frac{\eta\mathrm{d}\zeta}{A_\Sigma}\right]\mathrm{d}\eta\mathrm{d}\eta}_{\text{(a)}}=\underbrace{\frac{1}{Re_b}\int_0^{\eta_{\mathrm{top}}}\int_0^\eta\int_\zeta\frac{\partial\overline{u}}{\partial\eta}\mathrm{d}\zeta\mathrm{d}\eta\mathrm{d}\eta}_{\text{(b)}}$$

$$-\underbrace{\int_0^{\eta_{\mathrm{top}}}\int_0^\eta\int_\zeta\overline{u'v'_\eta}\mathrm{d}\zeta\mathrm{d}\eta\mathrm{d}\eta}_{\text{(c)}}-\sum_{i=1}^{N_j}\frac{1}{2}C^z_{\mathrm{jet}_i}s_{\mathrm{jet}}\underbrace{\int_0^{\eta_{\mathrm{top}}}\int_0^\eta\int_{\zeta_{\mathrm{jet}_i}}\left[w_{\mathrm{jet}_i}(\zeta)\frac{\mathrm{d}\zeta}{s_{\mathrm{jet}}}-\frac{\eta\mathrm{d}\zeta}{A_\Sigma}\right]\mathrm{d}\eta\mathrm{d}\eta}_{\text{(a)}}$$

$$\underbrace{-\int_0^{\eta_{\text{top}}}\int_0^{\eta}\int_0^{\eta}\int_{\zeta}\left(I_x''+\frac{\partial\bar{u}''}{\partial t}\right)\mathrm{d}\zeta\mathrm{d}\eta\mathrm{d}\eta\mathrm{d}\eta}_{\text{(c)}},\tag{3.41}$$

where the integrals labelled with (c) can be solved with (3.40) and the triple integral case. Integrals labelled with (a) can be substituted with a general variable ψ depending on η. Then, one can substitute $\psi = w_\psi(\zeta)\frac{\mathrm{d}\zeta}{s_\psi} - \frac{\eta\mathrm{d}\zeta}{A_\Sigma}$ and solve (a) as (c). Integral (b) can be solved as

$$\frac{1}{Re_b}\int_0^{\eta_{\text{top}}}\int_0^{\eta}\int_{\zeta}\frac{\partial\overline{u}}{\partial\eta}\mathrm{d}\zeta\mathrm{d}\eta\mathrm{d}\eta = \frac{1}{Re_b}\int_{\zeta}\int_0^{\eta_{\text{top}}}\int_0^{\eta}\mathrm{d}\overline{u}\left(\eta\right)\mathrm{d}\eta\mathrm{d}\zeta$$

$$= \frac{1}{Re_b}\int_{\zeta}\int_0^{\eta_{\text{top}}}\overline{u}\left(\eta\right)\mathrm{d}\eta\mathrm{d}\zeta = \int_{\zeta}\frac{\int_0^{\eta_{\text{top}}}\overline{u}\left(\eta\right)\mathrm{d}\eta}{Re_b}\mathrm{d}\zeta.\tag{3.42}$$

Solving for C_f^z, the FIK-E expression is obtained from (3.41) as

$$C_f^z\left(t\right) = \frac{2}{s_w\mathcal{A}}\left\{\mathcal{T}_{\text{bulk}}+\mathcal{T}_{\text{Rey}}+\mathcal{T}_{\text{jet}}+\mathcal{T}_{I_x}+\mathcal{T}_{\text{temp}}\right\},\tag{3.43}$$

where

$$\mathcal{A} = \int_{\zeta_w}\int_0^{\eta_{\text{top}}}\left(\eta_{\text{top}}-\eta\right)\left(w_w\left(\zeta\right)\frac{\mathrm{d}\zeta}{s_w}-\frac{\eta\mathrm{d}\zeta}{A_\Sigma}\right)\mathrm{d}\eta,\tag{3.44}$$

$$\mathcal{T}_{\text{bulk}} = \int_{\zeta}\frac{\int_0^{\eta_{\text{top}}}\overline{u}\left(\eta\right)\mathrm{d}\eta}{Re_b}\mathrm{d}\zeta,\tag{3.45}$$

$$\mathcal{T}_{\text{Rey}} = -\int_{\zeta}\int_0^{\eta_{\text{top}}}\left(\eta_{\text{top}}-\eta\right)\overline{u'v'_\eta}\mathrm{d}\eta\mathrm{d}\zeta,\tag{3.46}$$

$$\mathcal{T}_{\text{jet}} = -\frac{1}{2}s_{\text{jet}}\sum_{i=1}^{N_j}\left\{C_{\text{jet}_i}^z\int_{\zeta_{\text{jet}_i}}\int_0^{\eta_{\text{top}}}\left(\eta_{\text{top}}-\eta\right)\left[w_{\text{jet}_i}(\zeta)\frac{\mathrm{d}\zeta}{s_{\text{jet}}}-\frac{\eta\mathrm{d}\zeta}{A_\Sigma}\right]\mathrm{d}\eta\right\},\tag{3.47}$$

$$\mathcal{T}_{I_x} = -\int_{\zeta}\int_0^{\eta_{\text{top}}}\frac{1}{2}\left(\eta_{\text{top}}-\eta\right)^2\left(I_x-\frac{\iint_\Sigma I_x\mathrm{d}\eta\mathrm{d}\zeta}{A_\Sigma}\right)\mathrm{d}\eta\mathrm{d}\zeta,\tag{3.48}$$

$$\mathcal{T}_{\text{temp}} = -\int_{\zeta}\int_0^{\eta_{\text{top}}}\frac{1}{2}\left(\eta_{\text{top}}-\eta\right)^2\left(\frac{\partial\bar{u}}{\partial t}-\frac{\iint_\Sigma\frac{\partial\bar{u}}{\partial t}\mathrm{d}\eta\mathrm{d}\zeta}{A_\Sigma}\right)\mathrm{d}\eta\mathrm{d}\zeta,\tag{3.49}$$

and

$$C_\psi^z = \frac{1}{s_\psi}\int_\psi C_\psi(\zeta)d\psi,\tag{3.50}$$

$$w_\psi\left(\zeta\right) = C_\psi\left(\zeta\right)/C_\psi^z,\tag{3.51}$$

$$C_\psi = \frac{2}{Re_b}\left.\frac{\partial \overline{u}}{\partial \eta}\right|_{\eta=0}. \tag{3.52}$$

Throughout the rest of the thesis, reference to each part of the equation will be the following. The common factor in the FIK-E (3.43), $2/\left(s_w\mathcal{A}\right)$, multiplied by any of the terms $\mathcal{T}_{\text{bulk}}$, $\mathcal{T}_{\text{Rey}}$, $\mathcal{T}_{\text{jet}}$, $\mathcal{T}_{I_x}$, $\mathcal{T}_{\text{temp}}$ will be the bulk contribution, Reynolds stresses contribution, jets contribution, inhomogeneous contribution and temporal contribution, respectively. $\mathcal{A}$ is a function of the shape of the cross section as it depends on the skin friction force distribution. This thesis adopted the terminology of the bulk contribution as Peet and Sagaut (2009) instead of laminar from Fukagata et al. (2002). This is because the laminar term is the only contribution in the case of a smooth channel flow but that is not the case if the geometry changes with the x direction. Even though that is not in the scope of this thesis, this terminology is used for consistency.

Since the thesis is focused on channel flow, the sum of the convective terms, streamwise turbulent and viscous stresses components reduces to

$$I_x = \frac{\partial \bar{u}\bar{u}}{\partial x} + \frac{\partial \bar{u}\bar{v}}{\partial y} + \frac{\partial \bar{u}\bar{w}}{\partial z} + \frac{\partial \overline{u'u'}}{\partial x} - \frac{1}{Re_b}\frac{\partial^2 \overline{u}}{\partial x^2} = \nabla \cdot \left(\bar{u}\bar{\boldsymbol{v}}\right) \tag{3.53}$$

3.3 Validation and application

The channel flow with Zero Mass Jets (ZMJ) is studied with the FIK-E (3.43) to verify the simulation and assess each contribution of the skin friction coefficient. This also serves as a validation for the derived expression. There will be 3 cases to study: smooth channel flow, channel flow with ZMJ with jets off and the channel flow with ZMJ with jets on.

Even though Shefflow is an unstructured code, the simulations are not performed using a curvilinear grid like the one in figure 3.4. Simulations are computed in the Cartesian grids from sections 2.5.3, 2.7.3.1 and 2.7.3.2 and then the data is interpolated to the curvilinear grid with the proper transformations for analysis.

3.3.1 Smooth channel flow

As a first step to validate the FIK-E expression, it must reduce to the original expression introduced by Fukagata et al. (2002) when applied to the canonical case of the steady smooth channel. The FIK-E reduces to a single line integration where $w_w = 1$, $s_w = 1$ and $\eta_{\text{top}} = 1$.

Parameter	Value	Parameter	Value
L_x	2π	Re_b	2800
L_y	2	Re_τ	180
L_z	$4\pi/3$	u_b^*	42 m/s
Δx^+	8.84	h^*	0.001 m
Δy^+	0.2∼4.13	T^*	110.0 K
Δz^+	4.49	Δt^+	0.25

Table 3.1: Parameters of the simulation for the smooth channel flow. Viscous units are non-dimensionalised with a friction velocity of $u_\tau^* = 2.7$ m/s.

Moreover, $\mathcal{T}_{\text{jet}} = \mathcal{T}_{I_x} = \mathcal{T}_{\text{temp}} = 0$, which leaves the expression as

$$C_f^z = \frac{2}{\int_0^1 (1-\eta)(1-\eta)\,\mathrm{d}\eta}\left[\frac{\int_0^1 \overline{u}(\eta)\,\mathrm{d}\eta}{Re_b} - \int_0^1 (1-\eta)\,\overline{u'v'_\eta}\mathrm{d}\eta\right] \tag{3.54}$$

where $\int_0^1 (1-\eta)(1-\eta)\,\mathrm{d}\eta = 1/3$ and $\int_0^1 \overline{u}(\eta)\,\mathrm{d}\eta = 1$. Therefore, the original equation is completely recovered since $F'' = 0$ for smooth channel flows. In the case of an open boundary flow, $F'' \neq 0$ and the term $\frac{1}{2}\int_0^1 (1-\eta)^2 F''\mathrm{d}\eta$ is added inside the brackets in (3.54) as

$$C_f = \frac{6}{Re_b} - 6\int_0^1 (1-\eta)\,\overline{u'v'_\eta}\mathrm{d}\eta - 3\int_0^1 (1-\eta)^2 F''\mathrm{d}\eta. \tag{3.55}$$

Note that the original FIK method uses the $2u_b^*$ for scaling instead of u_b^*, therefore, to recover (11) of Fukagata et al. (2002), the first term is multiplied by 2 and the second and third term by 4. The DNS simulation by Shefflow for the smooth channel flow has the characteristics described in section 2.7.3, repeated in table 3.1 for convenience.

The skin friction coefficient value using FIK-E (3.43), simplified to C_f, is shown in table 3.2, which has been also compared with the results of Kim et al. (1987), labelled C_f^{KMM}, and the traditional skin friction coefficient formula, C_f^{slope}, defined in (3.7). The difference is computed as $C_f/C_f^{\text{KMM}} - 1$ or $C_f/C_f^{\text{slope}} - 1$. The theoretical bulk contribution for the smooth channel is $\mathcal{T}_{\text{bulk,smooth}} = 6/Re_b = 2.14 \times 10^{-3}$, while the one obtained by (3.54) has an error of 0.8%. Both the simulation and equation show good agreement with the case found in the literature. The main contribution to the friction coefficient comes from the Reynolds shear stress contribution.

C_f	Bulk contr.	Reynolds contr.
8.11×10^{-3}	2.16×10^{-3}	5.95×10^{-3}

C_f^{slope}	Difference
8.20×10^{-3}	-1.11%

C_f^{KMM}	Difference
8.18×10^{-3}	-0.87%

Table 3.2: Comparison and contributions of skin friction coefficient values for the smooth channel flow.

Parameter	Value	Parameter	Value
L_x	2π	Re_b	2800
L_y	$2.01, 1.98$	Re_τ	180
L_z	$4\pi/3$	u_b^*	$42\ m/s$
Δx^+	8.84	h^*	$0.001\ m$
Δy^+	0.2∼4.09	T^*	$110.0\ K$
Δz^+	0.5∼3.80	Δt^+	0.25
δ_{jet}^+	2	L_{step}^+	36
$\boldsymbol{v}_{\text{jet}}$	0	L_{jet}^+	90

Table 3.3: Parameters of the simulation for the ZMJ channel flow with jets off. Viscous units are non-dimensionalised with the friction velocity of the smooth channel flow.

3.3.2 WT-ZMJ with jets off

This simulation is performed using the channel flow of figure 2.10 with $\boldsymbol{v}_{\text{jet}} = 0$. The parameters of the channel are gathered in table 3.3. The values of L_y correspond to the two types of wall, being the largest the distance from the channel centre to the wall that has a length of L_{jet}, and the smallest the distance from the centre to the wall that has a length of L_{step}. These values are set so as the volume of the channel is the same as the volume of the smooth channel of section 3.3.1.

The cross-sectional grid for this case is the one in figure 2.11. There are a total of 12 sections, as there are 6 per wall.

The contributions to the skin friction coefficient as well as the comparison with the traditional skin friction coefficient formula can be found in table 3.4. Drag Reduction (DR) is

C_f	Bulk contr.	Reynolds contr.	Inhomogeneous contr.
8.10×10^{-3}	2.13×10^{-3}	5.94×10^{-3}	2.77×10^{-5}

C_f^{slope}	Difference	DR	DR (%)
8.20×10^{-3}	-1.25%	$O(10^{-5})$	$\sim 0\%$

Table 3.4: Comparison and contributions of skin friction coefficient values for the ZMJ channel flow with jets off.

computed as

$$DR = C_f / C_{f,\text{smooth}}^{\text{slope}} - 1, \tag{3.56}$$

where $C_{f,\text{smooth}}^{\text{slope}}$ is the skin friction coefficient of the smooth channel flow calculated with the traditional method. In this case, DR is almost not noticeable, as the change in geometry is minimum.

There is a small contribution to the skin friction coefficient from the inhomogeneous term as vortices are created due to the steps placed at the wall. As it is addressed in the next section, this contribution plays an important role in the FIK-E, and it is explained in detail in section 3.4.5.

3.3.3 WT-ZMJ with jets on

The DNS data from the simulation in section 2.7.3.2 is analysed with the FIK-E. The maximum velocity of the jets is the one of the baseline case $|\boldsymbol{v}_{\text{jet}}^+| = U_{\text{jet,max}}^+ = 27$ and the period of oscillation is $T_{\text{osc}}^+ = 125$. The angle at which the jets act is $\beta = 75\,\text{deg}$.

In order to apply the FIK-E, an ensemble average is applied in time. As shown in (3.18)–(3.20), the jets act in a periodic fashion. Moreover, it can be observed that the skin friction coefficient calculated with the traditional method is also periodic (figure 3.5). This fact is important, as a flow with no periodicity cannot be analysed as the ensemble average would not be correct. Statistics have been obtained from the time $t^+ = 250$ to $t^+ = 2125$.

A complete phase has 500 time steps, from which flow fields are extracted every 25 time steps and therefore, a phase has a resolution of 20 phase time steps. Averaging each phase, one can use the FIK-E to calculate the skin friction coefficient contributions, plotted in figure 3.6. Colours correspond to the contributions shown in the FIK-E equation, repeated in (3.57) for clarity. The boxed parts of the equation are integrated and multiplied by the leading term

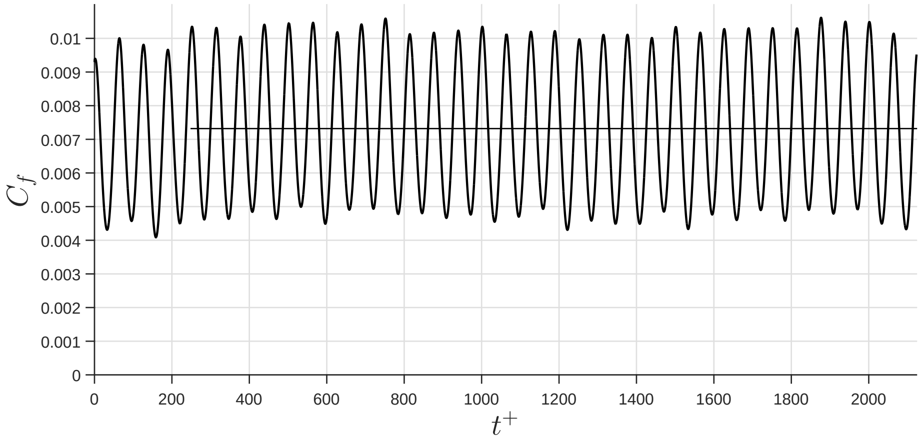

Figure 3.5: Friction coefficient history after the activation of jets at $t^+ = 0$. The straight line represents the mean skin friction coefficient once it stabilises.

to obtain the contributions in figure 3.6.

$$
\begin{aligned}
C_f^z(t) = \frac{2}{s_w \int_{\zeta_w} \int_0^{\eta_\text{top}} (\eta_\text{top} - \eta) \left(w_w(\zeta) \frac{\mathrm{d}\zeta}{s_w} - \frac{\eta \mathrm{d}\zeta}{A_\Sigma} \right) \mathrm{d}\eta} \Bigg\{ \int_\zeta \Bigg[& \boxed{\frac{\int_0^{\eta_\text{top}} \overline{u}(\eta) \mathrm{d}\eta}{Re_b}} - \boxed{\int_0^{\eta_\text{top}} (\eta_\text{top} - \eta) \overline{u' v'_\eta} \mathrm{d}\eta} \\
- \boxed{\int_0^{\eta_\text{top}} \frac{1}{2} (\eta_\text{top} - \eta)^2 \left(\frac{\partial \bar{u}}{\partial t} - \frac{\iint_\Sigma \frac{\partial \bar{u}}{\partial t} \mathrm{d}\eta \mathrm{d}\zeta}{A_\Sigma} \right) \mathrm{d}\eta} & - \boxed{\int_0^{\eta_\text{top}} \frac{1}{2} (\eta_\text{top} - \eta)^2 \left(I_x - \frac{\iint_\Sigma I_x \mathrm{d}\eta \mathrm{d}\zeta}{A_\Sigma} \right) \mathrm{d}\eta} \Bigg] \mathrm{d}\zeta \\
& - \boxed{\int_{\text{jet}_l} \frac{1}{2} s_\text{jet} C^z_{\text{jet}_l} \int_0^{\eta_\text{top}} (\eta_\text{top} - \eta) \left[w_{\text{jet}_l}(\zeta) \frac{\mathrm{d}\zeta}{s_\text{jet}} - \frac{\eta \mathrm{d}\zeta}{A_\Sigma} \right] \mathrm{d}\eta} \\
& - \boxed{\int_{\text{jet}_r} \frac{1}{2} s_\text{jet} C^z_{\text{jet}_r} \int_0^{\eta_\text{top}} (\eta_\text{top} - \eta) \left[w_{\text{jet}_r}(\zeta) \frac{\mathrm{d}\zeta}{s_\text{jet}} - \frac{\eta \mathrm{d}\zeta}{A_\Sigma} \right] \mathrm{d}\eta} \Bigg\}
\end{aligned} \tag{3.57}
$$

The mean skin friction coefficient in total time obtained with the FIK-E, $C_{f,\text{mean}} = 7.28 \times 10^{-3}$ is similar to the one obtained with the traditional method, $C_{f,\text{mean}}^\text{slope} = 7.32 \times 10^{-3}$, with a difference of -0.52%. As obtained in section 2.7.3.2, the reduction in drag is of 10.7%.

A more in-depth study of every contribution for this case is found in section 3.4.

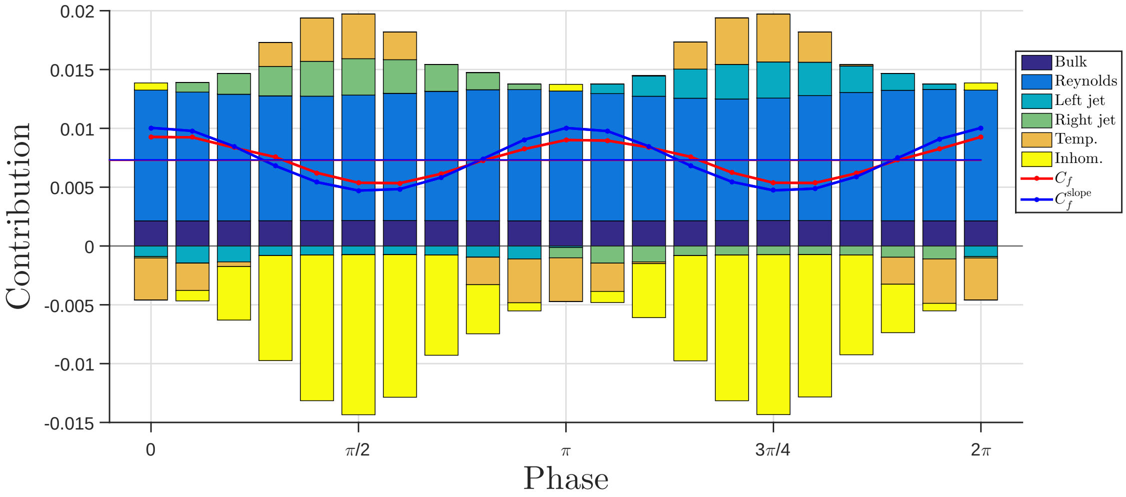

Figure 3.6: Friction coefficient contributions of the baseline case as a function of phase. Phase at $t = 0$ and $t = 2\pi$ are repeated for consistency. Straight lines represent the mean skin friction coefficient in total time for the traditional method (blue) and the FIK-E (red).

3.4 Detailed contributions

In this section, a detailed study of every term of the FIK-E expression (3.43) is presented. For that, the flow of section 3.3.3 is used.

3.4.1 Parameter $\mathcal{A}$

The parameter $\mathcal{A}$ is calculated through the skin friction distribution over the section. Peet and Sagaut (2009) used the laminar skin friction distribution to guess the value. However, in this thesis, the traditional method of calculating the skin friction (3.7) is used to calculate the ensemble average skin friction as a function of z and then, it is fed to the equation. Therefore, a closer guess can be used to calculate $\mathcal{A}$. An example of the distribution of skin friction can be plotted in figure 3.7.

Note that there are two places where the line is discontinued. Those are the jumps in geometry from the step wall and the jet wall. Oscillations near the sucking jet are numerical oscillations due to the numerical scheme. These oscillations have to be smoothed to achieve good results in the extended FIK method. For that, the velocity of the jet is imposed at the

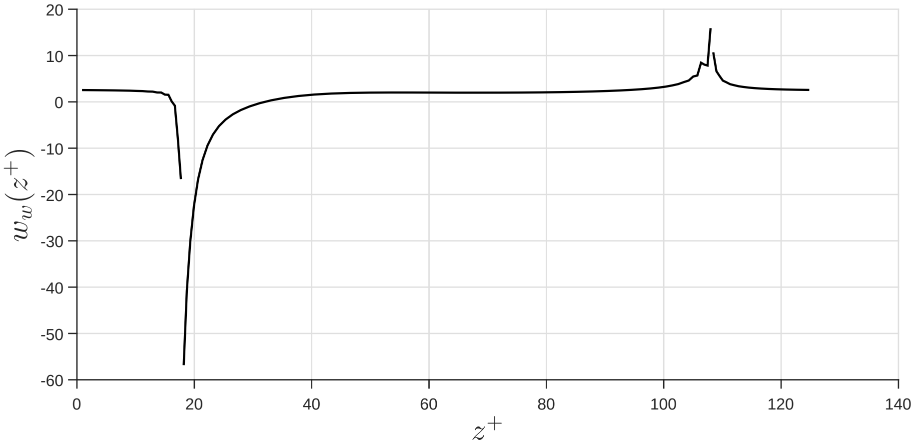

Figure 3.7: Distribution of skin friction using the traditional method (3.7) at $t = \pi/2$.

boundary condition and a spline is applied using 4-6 points. The corrected flow field can be compared in figure 3.8. Also, to visualise it better, the streamwise velocity u^+ at $y^+ = 1$ when the phase $\phi = \pi/2$, with the right jet extracting air from the domain and the left jet injecting air to the channel, is plotted in figure 3.9.

As commented in section 3.3.1, for the smooth channel, $\mathcal{A} = 1/3$, making the multiplicand of the FIK-E to have a value of 6. In this case, that value changes with phase (figure 3.10), but the oscillation in value is not high, as it changes around ±0.5%. However, the mean value increases more than 40%, resulting in higher contributions to the skin friction.

3.4.2 Bulk contribution

Throughout all the phases the bulk term is almost constant , even though the mean streamwise velocity changes.

However, the change is very localised and therefore, does not have a great effect in the ensemble mean. This value is close to the one of the smooth channel case with the same Reynolds number, $\mathcal{T}_{\text{bulk,smooth}} = 6/Re_b = 2.14 \times 10^{-3}$. The values obtained are $\mathcal{T}_{\text{bulk}} = 2.15 \times 10^{-3} \pm 9.21 \times 10^{-6}$.

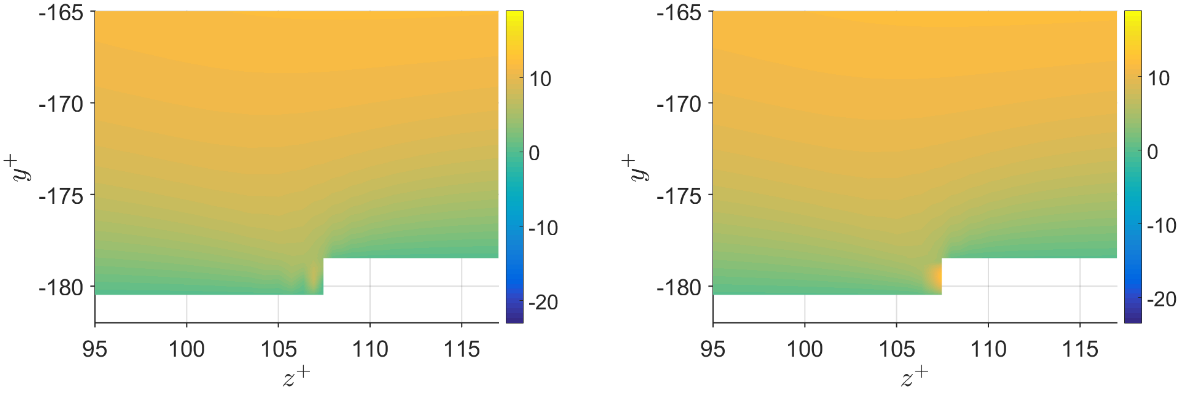

(a) Before smoothing.

(b) After smoothing.

Figure 3.8: Zoom of the right jet at phase $\phi = \pi/2$ showing the contour of u^+.

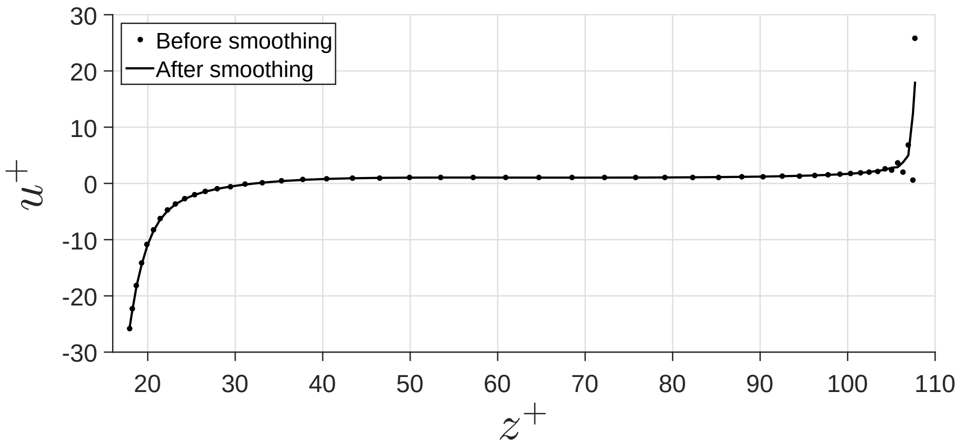

Figure 3.9: Streamwise velocity u^+ at $y^+ = 1$ at phase $\phi = \pi/2$ before and after the smoothing.

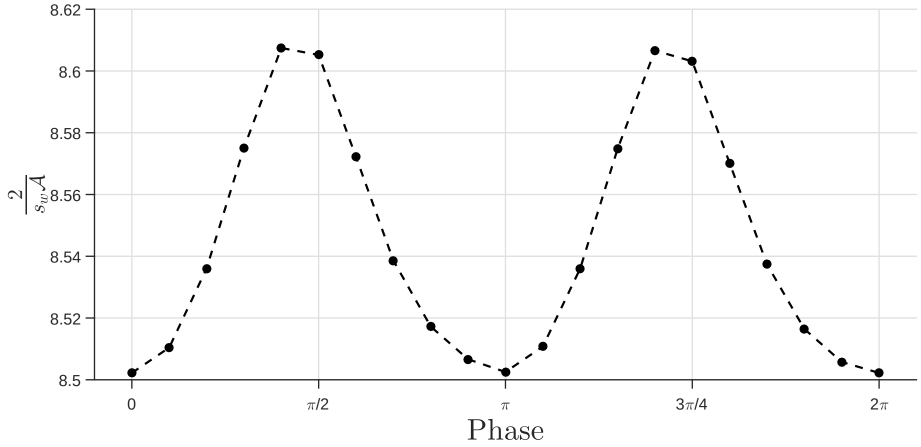

Figure 3.10: Multiplicand of FIK-E as a function of phase.

3.4.3 Reynolds stress contribution

The Reynolds stress contribution behaves similarly to that of the bulk contribution (figure 3.11).

The oscillation is bigger than in the bulk case but the oscillation is two orders lower. The values obtained are $\mathcal{T}_{\text{Rey}} = 1.08 \times 10^{-2} \pm 2.62 \times 10^{-4}$.

3.4.4 Jets contribution

Since the jet inclusion has a remarkable impact on the skin friction coefficient, the intuition tells us that this term should be determinant in the reduction of the skin friction. However, this term does not have that impact as this only accounts for the jet as a boundary condition. The impact on the skin friction comes mainly from the influence of jets *on* the flow.

As a matter of fact, the term associated with this contribution is similar to the friction coefficient itself. It can be seen as a portion of the wall that is removed and replaced by a moving wall. Since the relative area of the jets with respect to the wall is small, $2s_{\text{jet}}/s_w = 3.1\%$, the *friction* associated with it is small, as it can be appreciated in figure 3.12.

When the jet extracts air from the channel, the influence from this term is bigger. The blowing jet creates a plume of high speed air close to the boundary condition that extends in the flow field, whereas the sucking jet accelerates the surrounding air to the jet entrance. The more flow field is affected, the smaller the gradient is at the boundary, as the condition

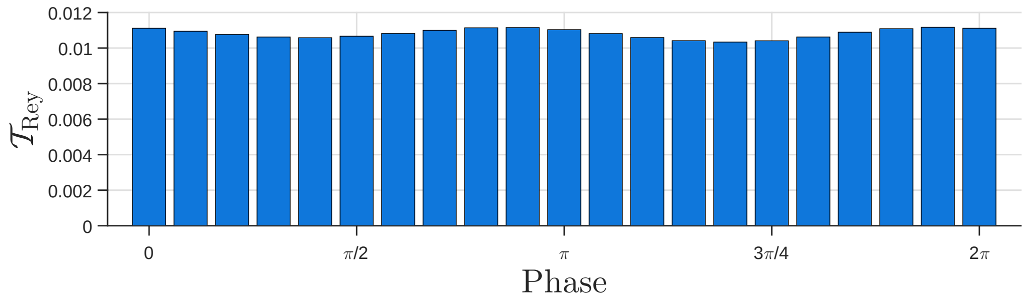

Figure 3.11: Reynolds shear stress contribution as a function of phase. Phase at $t = 0$ and $t = 2\pi$ are repeated for consistency.

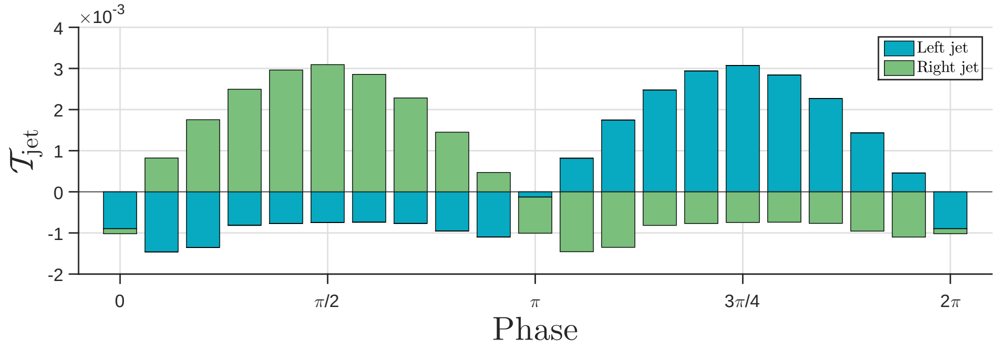

Figure 3.12: Jets contribution as a function of phase. Phase at $t = 0$ and $t = 2\pi$ are repeated for consistency.

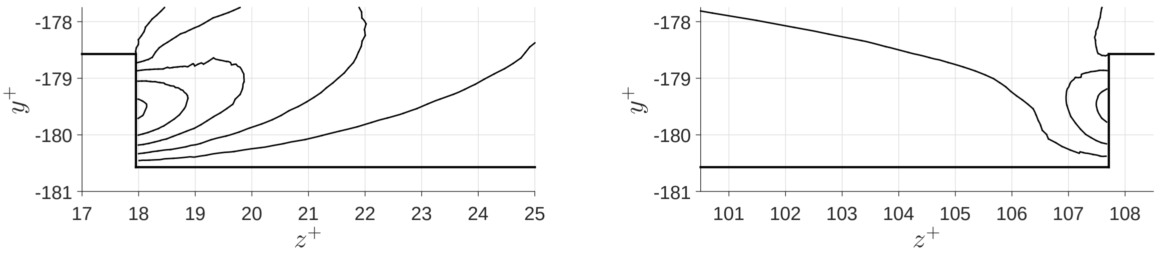

(a) Left jet.

(b) Right jet.

Figure 3.13: Contour levels of $\Delta|\boldsymbol{v}^+| = 5$ at $t = \pi/2$. The gradient is more abrupt in the right jet (b) than in the left jet (a), as the contour lines are closer together.

is spread more easily. An example of this phenomenon can be found in figure 3.13. As the jets approach the maximum velocity at the boundary, the flow changes with it. The flow near the blowing jet can *follow* the jet speed whereas the flow near the sucking jet cannot. That is why the blowing contribution to the skin friction decreases when approaching to the peak and the sucking contribution increases (figure 3.12).

3.4.5 Inhomogeneous contribution

The inhomogeneous contribution is the sum of different derivatives in the flow, reported in (3.53). There are two non-zero terms in the case of a channel case, $\partial\bar{u}\bar{v}/\partial y$ and $\partial\bar{u}\bar{w}/\partial z$, as the derivatives with respect to x are zero. The first term is related with the inhomogeneity in the y direction, which, in the case of a complex geometry, has always a non-zero value. The second term is related to the inhomogeneity in the z direction. In the flow fields studied in this thesis, the change of the v velocity in the y direction is usually lower than the change of the w velocity in the z direction, as the jets have a spanwise component, making the second term $\partial\bar{u}\bar{w}/\partial z$ dominant in the inhomogeneous contribution. Figure 3.14 shows these two terms for the baseline case. In this case, the spanwise component is three orders of magnitude bigger than the component normal to the wall.

This second term is also related to the symmetry of the flow field to the z direction of the device, as a symmetric flow field to the centre of the device would mean the cancellation of the derivatives with respect to z. This is the key contribution of the ZMJ. As discussed in section 3.4.4, the jets modify the flow by the injection of momentum. This momentum injection translates into high localised velocities near the wall close to the jet, which break

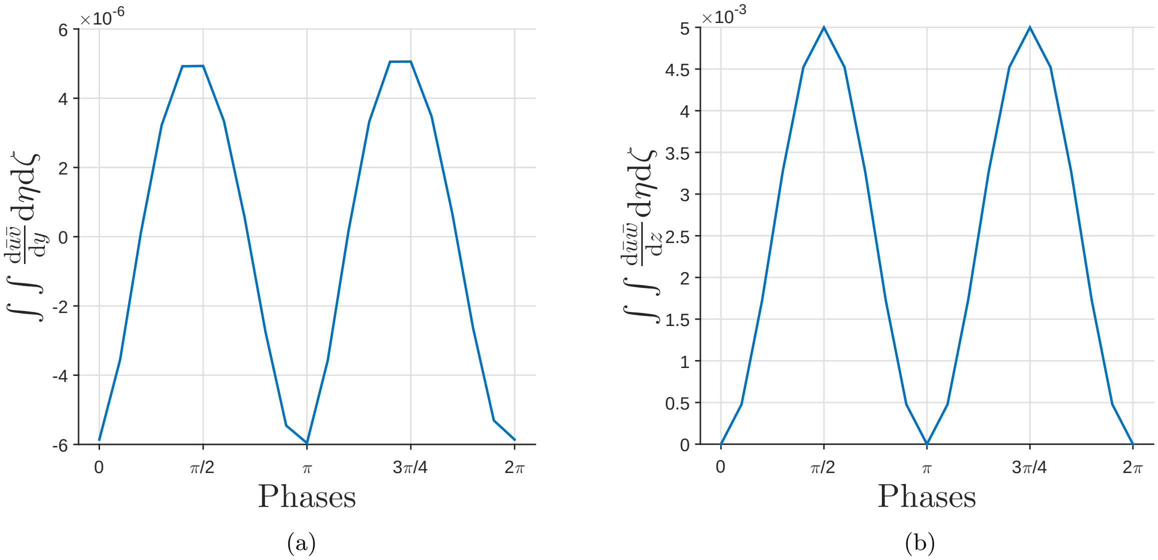

(a)

(b)

Figure 3.14: Integration of the two non-zero terms in the inhomogeneous contribution for the ZMJ baseline case.

the symmetry of the flow, which can also be appreciated in figure 3.13. With this, the value of I_x increases (figure 3.15) and therefore, the inhomogeneous contribution decreases the skin friction coefficient.

It is of interest to observe this contribution when the jets are off, like in section 3.3.2. The inhomogeneous contribution is almost zero in this case because the flow is symmetric, but there is a slight deviation from zero due to the first non-zero term in the inhomogeneous contribution. The value of I_x for the case with ZMJ off can be observed in figure 3.16.

3.4.6 Temporal contribution

As a side effect, the change in velocity for localised parts of the flow field has a negative impact in the skin friction coefficient as well. The blowing jet at 75 deg introduces a plume of negative velocity, therefore, increasing the temporal contribution when the jet approaches its maximum velocity. Although this increase is negative for the drag reduction, when the jets approach to their minimum influence, the flow recovers itself. This produces the opposite effect, making this contribution beneficial to the skin friction.

If an average is taken over time instead of phase, the temporal contribution cancels itself

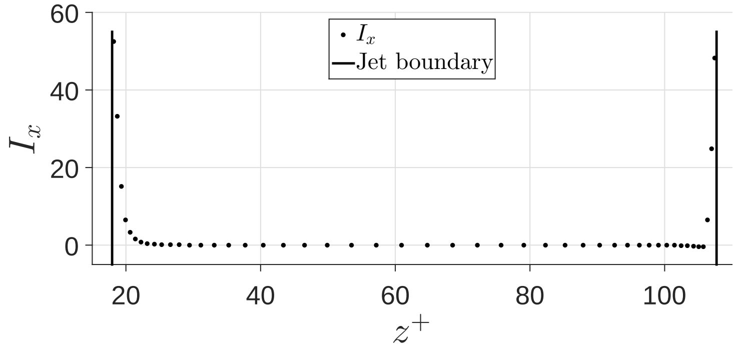

Figure 3.15: Inhomogeneous contribution at $y^+ = 1$ from the jet wall, which is the centre of the jet. Phase time is $t = \pi/2$.

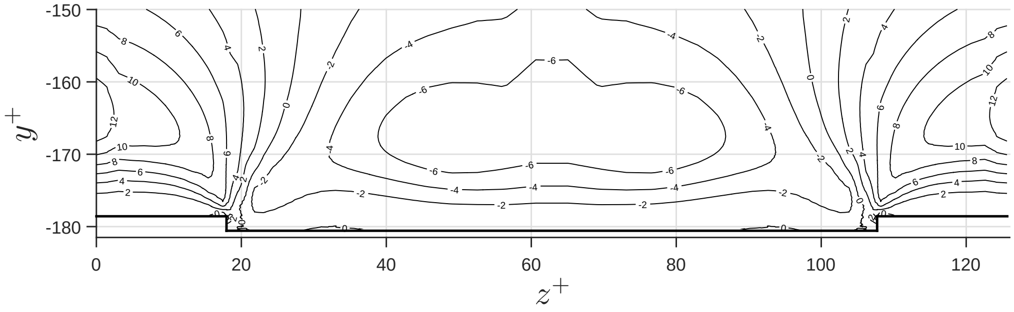

Figure 3.16: Cross section view of the quantity I_x of the case with ZMJ off. Values are multiplied by 10^3. The y coordinate starts at the centre of the channel.

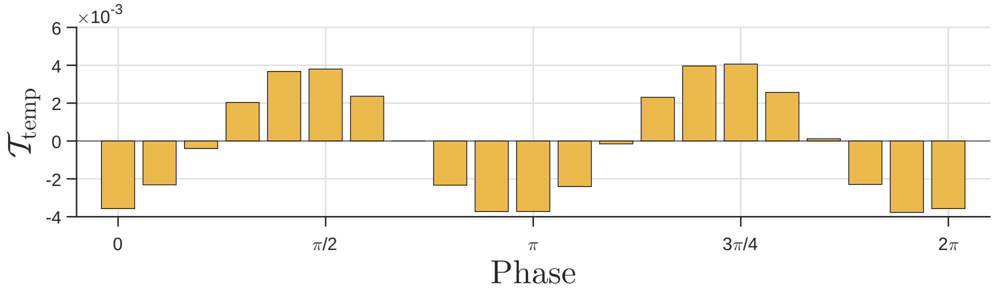

Figure 3.17: Temporal contribution as a function of phase. Phase at $t = 0$ and $t = 2\pi$ are repeated for consistency.

out, plotted in figure 3.17.

3.5 Conclusions

This chapter has presented a way to relate skin friction to flow field data in complex geometries with boundary conditions that are not necessary walls. It includes a detailed derivation of the expression from the Navier-Stokes equation, assuming the flow is incompressible.

The FIK-E expression gives the skin friction value as a function of phase, given that the flow statistics are periodic.

Moreover, a detailed study of cases where jets firing close to the wall and parallel to it is performed. The study of the baseline case shows the following:

- As a consequence of the WT-ZMJ, Reynolds stresses increase, which makes its contribution a 78.9% higher than the one for the smooth channel.
- The inhomogeneous contribution on the other hand, decreases drastically the total skin friction coefficient when the jets are active, accounting for the increase in Reynolds stresses and other effects like the negative temporal contribution and the sucking jet.
- For the phase when the jets are not active, due to their oscillatory behaviour, the temporal contribution helps lowering the skin friction. However, in the case studied, this contribution does not lower the skin friction enough to get a reduction at that specific phase, but helps the overall skin friction.

As the inhomogeneous contribution is the most important contribution for the reduction of skin friction, there is a focus in changing the flow close to the wall and the jets (as there is a factor of $(1-\eta)^2$).

Different combinations of parameters are to be tested and analysed with the FIK-E method to maximise the efficiency on drag reduction.

Chapter 4

Power consumption of the WT-ZMJ and parametric study

4.1 Introduction

It has been proved that the Wall Tangential Zero-Mass Jets reduce the skin friction coefficient at an optimum β angle of around 75 deg by 10.7%. However, a way to produce the jet boundary condition has to be created. The device capable of producing these jets is discussed in section 4.2 along with its power requirements.

Different parameters are varied to study their effects and find whether there exist a better set of parameters that further reduce the skin friction. The jet period of oscillation T_{osc}, the maximum jet velocity $U_{\mathrm{jet,max}}$ and the distance between jets L_{jet} are the parameters chosen for this study. The FIK-E method derived in chapter 3 is used to analyse the flow fields to have a better understanding of the reduction or increase of the friction coefficient. The β angle is also studied with this technique.

4.2 Energy analysis for baseline

An estimate of the power required to operate the jets is presented in this section using a model of the chambers underneath the channel walls. Figure 4.1 shows a schematic of the system. A piston separates the two chambers and moves sinusoidally in the z direction, forcing the fluid in the compression chamber to discharge through the jet opening and out into the channel. Simultaneously, the pressure drops in the suction chamber, causing the fluid to enter the

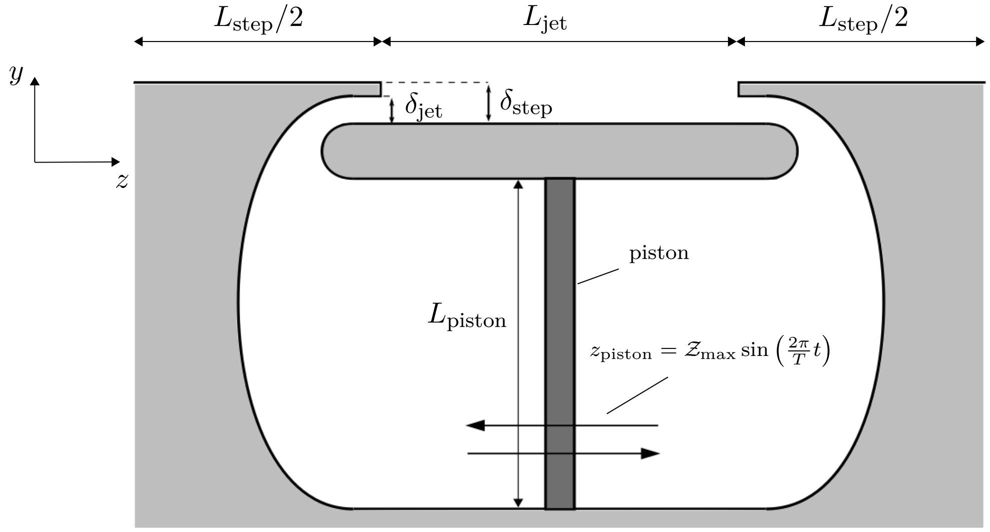

Figure 4.1: Schematic of the chambers producing the wall jets.

jet opening and fill the chamber. The chambers alternate their behaviour every half cycle, according to the motion of the piston.

The in-house code Shefflow is used to compute the flow in the chamber and outside of the jet openings. The domain of the simulation consists of the chambers and half of the channel above them. Symmetry boundary conditions are imposed at the half channel boundary and periodic boundary conditions are enforced at the sides of the computational domain. The flow is assumed to be laminar and two-dimensional in this study. Figure 4.1 represents the purely spanwise case ($\beta = 0$). In the practical case of oblique jets, the exits would require inclined vanes to drive the fluid out into the channel at an angle. The losses due to the three-dimensionality of the vanes are assumed small with respect to the rest of the losses and are studied in section 4.2.1.1. The wall that separates the jet and the channel above has a finite thickness. This avoids a sharp wall end of zero thickness at the jet exit, which would create intense velocity gradients when the fluid leaves the chamber.

As a two-dimensional simulation, there is no streamwise flow. However, the half height h^*, the bulk velocity u_b^* and the viscous velocity u_τ of the reference smooth channel case are still used to scale quantities. The parameters of the chambers and the simulation details are found in table 4.1.

L^+_{step}	L^+_{jet}	L^+_{piston}	δ^+_{jet}	δ^+_{step}	$\langle w \rangle^+_{\text{jet,max}}$	T^+_{osc}	Δt^+	u^*_b (m/s)
36	90	50	2	2.5	18	125	0.25	42

Table 4.1: Simulation and chamber parameters. $\langle w \rangle_{\text{jet,max}}$ is the jet velocity spatial mean, T_{osc} is the period of oscillation and Δt is the time step. The other quantities are found in figure 4.1.

The position of the piston is described by

$$z_{\text{piston}} = \mathcal{Z}_{\text{max}} \sin\left(\frac{2\pi}{T_{\text{osc}}} t\right), \tag{4.1}$$

where T_{osc} is the period of oscillation of the piston and $\mathcal{Z}_{\text{max}}$ is the maximum displacement travelled by the piston with respect to the central position. The period of oscillation T_{osc} is the same as the period of oscillation of the jet boundary condition in the full three-dimensional simulation. The maximum displacement $\mathcal{Z}_{\text{max}}$ as a function of the average jet velocity is calculated using the conservation of mass. The flow inside the chamber is compressible, but in order to have a estimation of the piston velocity, the incompressible version of the continuity equation is used,

$$\int_A \boldsymbol{v} \cdot \boldsymbol{n} \mathrm{d}A = 0, \tag{4.2}$$

where A is the surface of the chamber including the jet exit orifice and $\boldsymbol{n}$ is the normal unit vector perpendicular to A, pointing outwards. Since $\boldsymbol{n}$ for the piston surface and for the jet exit surface point in the z direction, (4.2) reduces to

$$- w_{\text{piston}}\left(t\right) A_{\text{piston}} + \int_{A_{\text{jet}}} w_{\text{jet}}\left(y, t\right) \mathrm{d}A = 0, \tag{4.3}$$

where w_{piston} is the velocity of the piston and w_{jet} is the velocity profile at the jet exit, A_{piston} is the surface of the piston, and A_{jet} is the jet exit area. Writing (4.3) per unit depth, the surface integral becomes a line integral from the base of the jet wall to the beginning of the step,

$$- w_{\text{piston}}\left(t\right) L_{\text{piston}} + \int_0^{\delta_{\text{jet}}} w_{\text{jet}}\left(y, t\right) \mathrm{d}y = 0. \tag{4.4}$$

where L_{piston} is the length of the piston. The spatial mean velocity of the jet, defined according to

$$\langle w \rangle_{\text{jet}}(t) = \frac{1}{\delta_{\text{jet}}} \int_{\delta_{\text{jet}}} w_{\text{jet}}(y,t)\,\mathrm{d}y, \tag{4.5}$$

and the velocity of the piston, found from (4.1), are substituted into (4.4). The maximum displacement of the piston is

$$\mathscr{Z}_{\max} = \frac{T}{2\pi} \frac{\delta_{\text{jet}}}{L_{\text{piston}}} \langle W \rangle_{\text{jet,max}} \,. \tag{4.6}$$

where $\langle W \rangle_{\text{jet,max}}$ is the maximum spatial mean velocity achieved by the jet within a period.

The boundary conditions for the jet velocity in the three-dimensional simulation are the ones found in table 4.1, which result into an amplitude of $\mathscr{Z}_{\max} = 0.079$ and, consequently, a maximum piston velocity of $W_{\text{piston,max}} = 0.046$.

To calculate the power required to move the piston, P_{piston}, an integration of the difference in pressure is performed over the piston as a function of time. This results in the force that the piston has to overcome at the required velocity at time t to produce the jet flow at the exit. The scaled power per unit width is

$$P_{\text{piston}}(t) = \frac{2P^*_{\text{piston}}(t)}{\rho^* u_b^{*3} L^*_{\text{piston}}}, \tag{4.7}$$

where

$$P^*_{\text{piston}}(t) = w^*_{\text{piston}}(t) \int_{L_{\text{piston}}} \Delta p^*_{\text{piston}}(y,t)\mathrm{d}y, \tag{4.8}$$

and $\Delta p^*_{\text{piston}}$ is the pressure difference on the piston. Figure 4.2 shows the averaged non-dimensional pressure difference acting on the wall,

$$\Delta p_{\text{piston}}(t) = \frac{2}{\rho^* u_b^{*2} L^*_{\text{piston}}} \int_{L_{\text{piston}}} \Delta p^*_{\text{piston}}(y,t)\,\mathrm{d}y, \tag{4.9}$$

and the power required to move the piston at w_{piston}. Quantities in figure 4.2 are ensemble-averaged over the period of oscillation. The start of the period is defined when the left jet starts to inject the fluid into the channel. The phase of the piston movement, given by (4.1), has therefore a 90 deg phase difference since the piston starts at the central position.

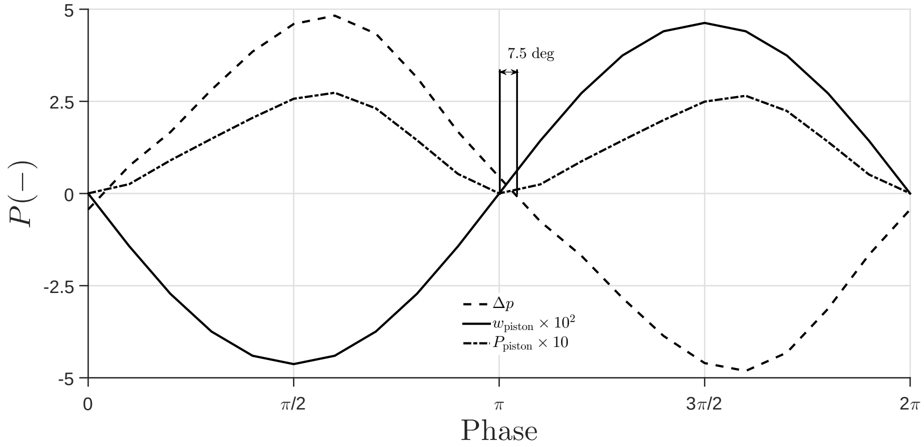

Figure 4.2: Ensemble average of the velocity of the piston, pressure difference and power required to move the piston.

The averaged power required to move the piston is

$$\bar{P}_{\text{piston}} = \frac{1}{T} \int_0^T P_{\text{piston}}(t)\,\mathrm{d}t. \tag{4.10}$$

For the case with the conditions of table 4.1, $\bar{P}_{\text{piston}} = 14.07 \times 10^{-2}$. There is a slight phase lag of approximately 7.5 deg between the pressure experienced by the piston and the velocity of the piston. This is due to compressibility effects near the piston wall as seen in figure 4.3. Compressibility effects are more pronounced near the zone where the piston and the static wall meet.

Figure 4.4 shows the right jet velocity profile imposed in the three-dimensional simulation with the 7.5 deg phase lag included and the velocity profile of the two-dimensional simulation. When air enters the chamber, from phase 0 to π, the maximum velocity peak is slightly closer to the bottom solid surface instead of maintaining a symmetric profile. This is due to the fact that air that comes from the step wall has to change completely its momentum whereas the air that comes from the jet wall does not.

The results obtained in the two-dimensional simulation are consistent with the assumption of a parabolic jet flow for the three-dimensional channel flow simulation.

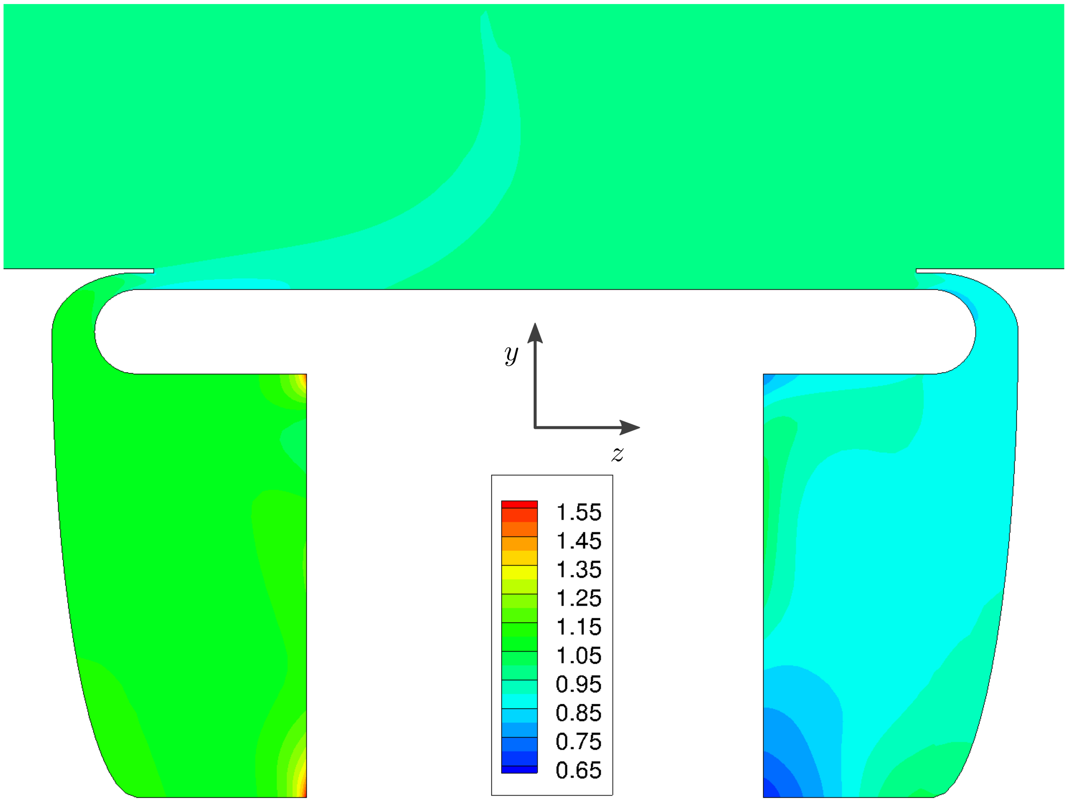

Figure 4.3: Contour levels of ρ/ρ_0 at $t = \pi/2$. The left chamber is at the compression phase and the right chamber is at the expansion phase.

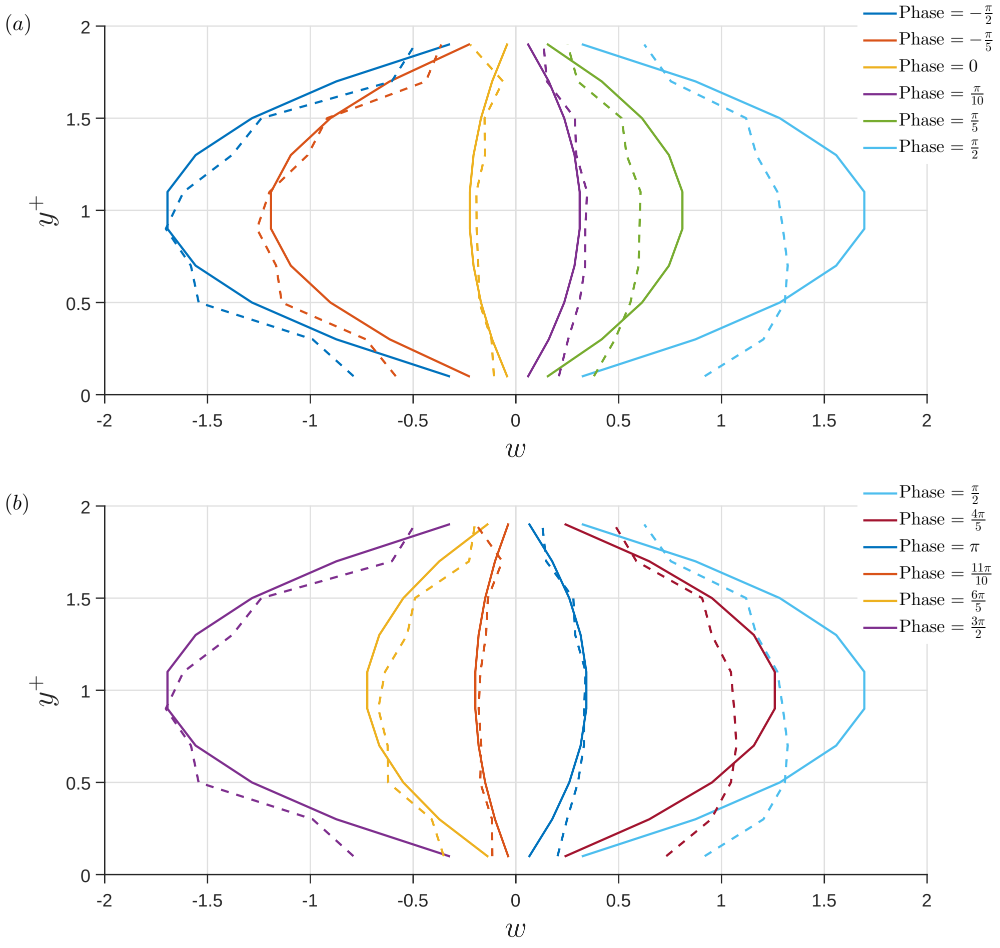

Figure 4.4: Velocity profiles at the exit of the right jet. Solid lines represent the parabolic boundary condition imposed in the three-dimensional channel flow simulations with a phase delay of 7.5deg to compare with the laminar simulation. Dashed lines represent the actual velocity obtained with the laminar simulation. Phases from the neutral position when the piston moves towards the positive z direction ($-\pi/2$) to the neutral position half a cycle later ($\pi/2$) are represented in (a). Phases from the neutral position when the piston moves towards the negative z direction ($\pi/2$) to the neutral position half a cycle later ($3\pi/2$) are represented in (b).

4.2.1 Cavity losses and efficiency of the device

The power required to operate the piston has to overcome losses due to the shear stresses on the chamber walls and the viscous energy dissipation to generate the jets. The compressible kinetic energy equation (1-106) in Hinze (1975) is useful to compute these losses. Integrating (1-106) in Hinze (1975) over the volume leads to

$$\int_V \frac{\mathrm{D}}{\mathrm{D}t}\frac{|\boldsymbol{v}|^2}{2}\mathrm{d}V = -\frac{1}{2}\int_V \boldsymbol{v}\cdot\nabla p\mathrm{d}V + \frac{1}{Re_b}\int_V \nabla\cdot\left(\boldsymbol{v}\cdot\overline{\overline{\tau}}\right)\mathrm{d}V - \frac{1}{Re_b}\int_V \overline{\overline{\tau}} : \nabla\boldsymbol{v}\mathrm{d}V, \tag{4.11}$$

where the operand $\mathrm{D}()/\mathrm{D}t$ is the material derivative, $\nabla()$ is the gradient, $\nabla\cdot()$ is the divergence, $:$ is the contraction, V is the volume of the chamber, $\overline{\overline{\tau}}$ is the viscous shear stress tensor and Re_b is the Reynolds number based on u_b^*. Expanding the material derivative and the first term of the right hand side,

$$\int_V \frac{\partial}{\partial t}\frac{|\boldsymbol{v}|^2}{2}\mathrm{d}V + \int_\Sigma \frac{|\boldsymbol{v}|^2}{2}\boldsymbol{v}\cdot\boldsymbol{n}\mathrm{d}\sigma = \frac{1}{2}\int_V p\left(\nabla\cdot\boldsymbol{v}\right)\mathrm{d}V - \frac{1}{2}\int_V \nabla\cdot\left(\boldsymbol{v}p\right)\mathrm{d}V$$

$$+\frac{1}{Re_b}\int_V \nabla\cdot\left(\boldsymbol{v}\cdot\overline{\overline{\tau}}\right)\mathrm{d}V - \frac{1}{Re_b}\int_V \overline{\overline{\tau}} : \nabla\boldsymbol{v}\mathrm{d}V, \tag{4.12}$$

where Σ denotes the bounded surface of the volume of the chamber. Applying the divergence theorem to the second and third terms of the right hand side of the equation,

$$P_{\mathrm{t}} = P_{\mathrm{jet}} + P_{\mathrm{piston}} + P_{\mathrm{surface\,forces}} - \left[P_{\mathrm{compression}} + P_{\mathrm{dissipation}}\right], \tag{4.13}$$

where

$$P_{\mathrm{t}} = \int_V \frac{\partial}{\partial t}\frac{|\boldsymbol{v}|^2}{2}\mathrm{d}V, \tag{4.14}$$

$$P_{\mathrm{jet}} = -\frac{1}{2}\int_{\Sigma_{\mathrm{jet}}} \left(p + |\boldsymbol{v}|^2\right)\boldsymbol{v}\cdot\boldsymbol{n}\mathrm{d}\sigma, \tag{4.15}$$

$$P_{\mathrm{piston}} = -\frac{1}{2}\int_{\Sigma_{\mathrm{piston}}} \left(p + |\boldsymbol{v}|^2\right)\boldsymbol{v}\cdot\boldsymbol{n}\mathrm{d}\sigma, \tag{4.16}$$

$$P_{\mathrm{surface\,forces}} = -\frac{1}{Re_b}\int_{\Sigma_{\mathrm{jet}}} \boldsymbol{v}\cdot\overline{\overline{\tau}}\cdot\boldsymbol{n}\mathrm{d}\sigma, \tag{4.17}$$

$$P_{\mathrm{compression}} = -\frac{1}{2}\int_V p\left(\nabla\cdot\boldsymbol{v}\right)\mathrm{d}V, \tag{4.18}$$

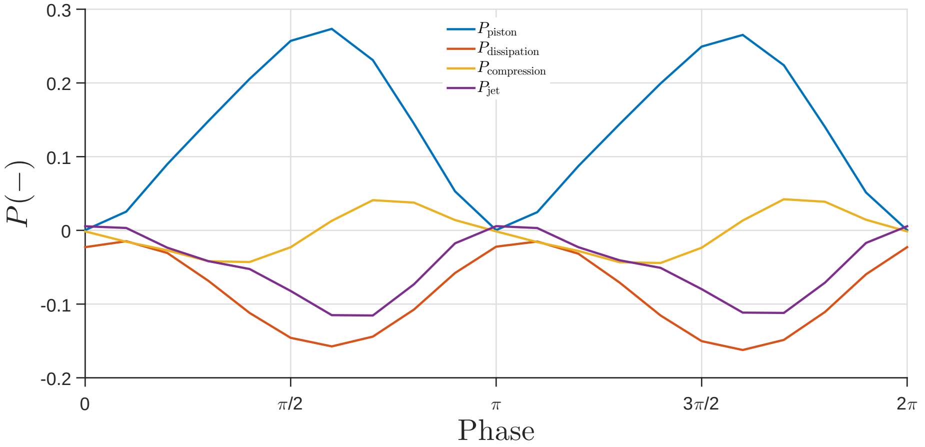

Figure 4.5: Power spent on the actuation of the jets and loss in the chambers. Positive values mean power being applied to the chambers and negative values mean losses of power from the chambers.

$$P_{\text{dissipation}} = \frac{1}{Re_b} \int_V \overline{\overline{\tau}} : \nabla \boldsymbol{v} \mathrm{d}V. \tag{4.19}$$

The last two terms have been written separately to show that these are responsible to transform mechanical energy into internal energy and vice versa in the case of the compression term whereas the rest of the term are devoted only to increase or decrease the mechanical power. Expressing (4.13) per width and applying the ensemble average, the result shows that the simulation can be treated as quasi-steady because P_{t} can be neglected as it is five orders of magnitude smaller than the other terms of the right hand side of (4.13). Also, $P_{\text{surface forces}} \approx 0$ because the velocity at the exit of the jet is almost symmetric and $\partial w/\partial z \approx 0$. For the sake of clarity, these two terms are not shown in figure 4.5, which shows the power spent in both chambers through a complete cycle.

A slight phase lag exists between the piston actuation and the jets due to compressibility effects found in the chambers. The power from the piston is spent in the compression/expansion of air when the piston accelerates (phases $\phi = 0$ to $\pi/2$ and $\phi = \pi$ to $3\pi/2$) and it is recovered once the piston decelerates (phases $\phi = \pi/2$ to π and $\phi = 3\pi/2$ to 2π). The mean power associated with the jets is $\bar{P}_{\text{jet}} = 5.22 \times 10^{-2}$, making the mean power lost in the chambers due to dissipation $\bar{P}_{\text{dissipation}} = 8.74 \times 10^{-2}$ and compressibility effects $\bar{P}_{\text{compression}} = 0.47 \times 10^{-2}$. The efficiency of the device is therefore $\bar{P}_{\text{jet}}/\bar{P}_{\text{piston}} = 37.1\%$.

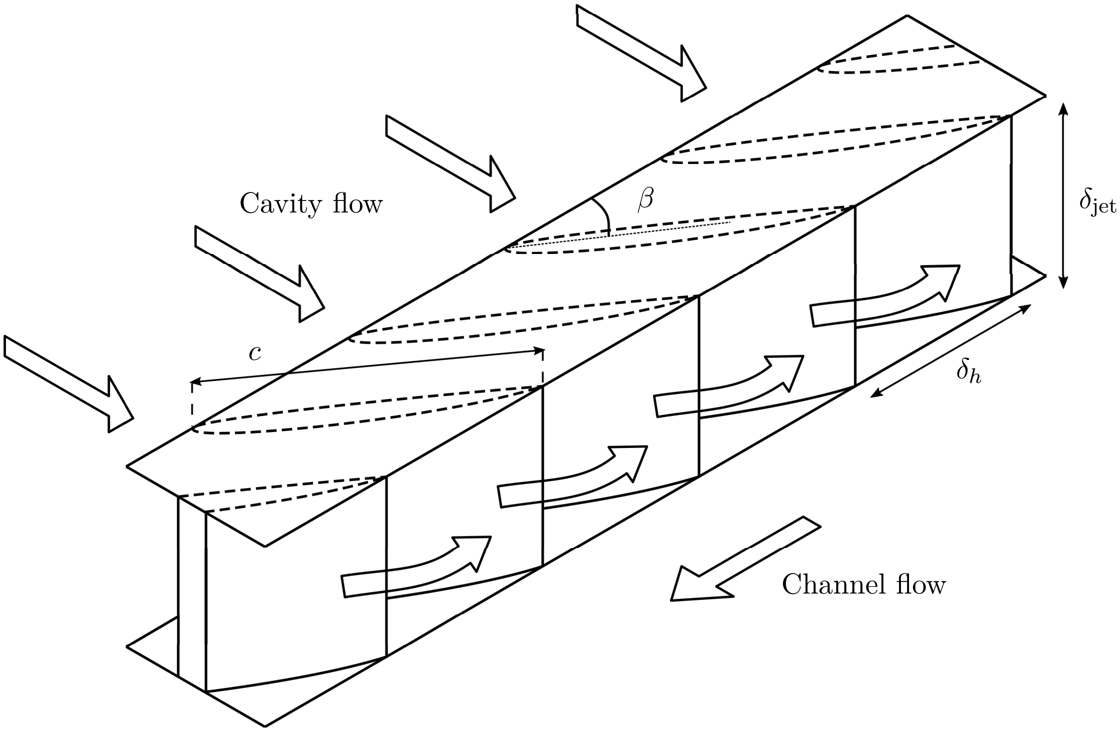

Figure 4.6: Schematic of the guide vanes used to change the direction of the flow to an angle β.

4.2.1.1 Estimation of guide vane power loss

To reproduce the jets at a β angle from the channel flow direction, guide vanes are placed before the jet exit as in figure 4.6. In order to estimate the loss of pressure and velocity, a comparison with the corner turning vanes of a wind tunnel is performed.

Vane shapes used to turn the direction of the flow range from bent plates to highly cambered airfoils. According to Barlow et al. (2015), the corner loss coefficient for a 90 deg turn is

$$K = \frac{\Delta H}{q_{\text{in}}} \tag{4.20}$$

where $\Delta H = p_{\text{out}} + q_{\text{out}} - (p_{\text{in}} + q_{\text{in}})$, the subscript *in* stands for the flow before the vanes and *out* for the flow after the vanes and $q = \frac{1}{2}\rho u^2$ is the dynamic pressure. The 90 deg turning is unrealistic, but it gives an idea of the worst possible scenario, as the vanes would be at

$\beta = 75\,\mathrm{deg}$.

Although there is an extensive literature on losses around corners, very low Reynolds numbers are not studied. The lowest Reynolds number based on the cord of the vane found is $Re_c = 154000$ by Sahlin and Johansson (1991). The empirical formula as a function of Re_c for a gap-cord ratio $\delta_h/c = 1/4$ according to Barlow et al. (2015) is

$$K = 0.10 + \frac{4.55}{(\log_{10} Re_c)^{2.58}}, \tag{4.21}$$

where, in the case of the exit cavity flow with $c = 4\delta_{\mathrm{jet}}$, the Reynolds number is $Re_c = 216$. Using (4.21), the corner loss coefficient is $K = 0.61$. Assuming the maximum velocity before the vanes to be $\langle W\rangle_{\mathrm{jet,max}}$ and that the pressure and velocity are reduced proportionally, the percentage of the power after the guide vanes can be calculated as $r_{\mathrm{vanes}} = P_{\mathrm{before}}/P_{\mathrm{after}} \times 100$ where

$$P_{\mathrm{before/after}} = pu\delta_h\delta_{\mathrm{jet}}. \tag{4.22}$$

For the case with the conditions of table 4.1, $r_{\mathrm{vanes}} = 93\%$. Therefore, the power of the jet is reduced to $\bar{P}_{\mathrm{jet}} = 4.86 \times 10^{-2}$ and the overall efficiency of the device is $\bar{P}_{\mathrm{jet}}/\bar{P}_{\mathrm{piston}} = 34.5\%$.

4.2.2 Channel flow power

For the channel flow simulation, the additional term of the driving force $(\partial p/\partial x)_{\mathrm{drive}}$ is extracted from (4.11), specifically from the first term of the right hand side as

$$\nabla p = \begin{bmatrix} \partial p/\partial x \\ 0 \\ 0 \end{bmatrix}_{\mathrm{drive}} + \begin{bmatrix} \partial p/\partial x \\ \partial p/\partial y \\ \partial p/\partial z \end{bmatrix}', \tag{4.23}$$

where the ' refers to the fluctuations in pressure difference. The driving pressure difference is applied to the entire channel. This separation produces the term for the driving power

$$P_{\mathrm{drive}} = -\frac{1}{2}\int_V u \left[\frac{\partial p}{\partial x}\right]_{\mathrm{drive}} \mathrm{d}V = -\frac{1}{2}\left[\frac{\partial p}{\partial x}\right]_{\mathrm{drive}} \int_V u\mathrm{d}V. \tag{4.24}$$

The channel flow is, contrary to the cavity flow, incompressible and therefore, according to the x-direction momentum equation,

$$\frac{\partial u}{\partial t} = -\frac{1}{2}\frac{\partial p}{\partial x} - \nabla \cdot \left(-u\boldsymbol{v} + \frac{1}{Re_b}\nabla \cdot \overline{\overline{\tau}} \cdot \boldsymbol{n} \right), \tag{4.25}$$

which can be simplified by an average in time and in the x-direction as

$$\frac{1}{2}\left[\frac{\partial p}{\partial x}\right]_{\mathrm{drive}} = -\frac{\partial \overline{u u_i}}{\partial x_i} - \frac{\partial \overline{u' u'_i}}{\partial x_i} + \frac{1}{Re_b}\frac{\partial^2 \overline{u}}{\partial x_i^2}, \tag{4.26}$$

where the Einstein notation has been adopted with subscripts $i = 2, 3$ which denote y, z directions and v, w velocity components. Integration in y from the bottom wall to the top wall leads to

$$\left[\frac{\partial p}{\partial x}\right]_{\mathrm{drive}} = -\int \frac{\partial \overline{uw}}{\partial z}\mathrm{d}y - \int \frac{\partial \overline{u'w'}}{\partial z}\mathrm{d}y + \frac{2}{Re_b}\left.\frac{\partial \overline{u}}{\partial y}\right|_{y=0} + \frac{1}{Re_b}\int \frac{\partial^2 \overline{u}}{\partial z^2}\mathrm{d}y, \tag{4.27}$$

where another integration in z makes the first, second and third integral zero due to temporal symmetry. Substitution in (4.24) and noting that $\int u \mathrm{d}y = 2$ yields

$$P_{\mathrm{drive}} = -\frac{2}{Re_b}\left.\frac{\partial \overline{u}}{\partial y}\right|_{y=0} L_x L_{\mathrm{device\,wall}}. \tag{4.28}$$

where $L_{\mathrm{device\,wall}} = L_{\mathrm{step}} + L_{\mathrm{jet}}$. Note that $(L_x, L_{\mathrm{device\,wall}}) = (L_x^*, L_{\mathrm{device\,wall}}^*)/L_{\mathrm{piston}}^*$

Substitution of the mean friction coefficient $\overline{C}_f$ and expressing (4.28) per unit width,

$$P_{\mathrm{drive}} = \overline{C}_f L_{\mathrm{device\,wall}}. \tag{4.29}$$

For the baseline, where the friction coefficient is reduced 10.7%, from 8.20×10^{-3} to 7.32×10^{-3}, the average power saved is $\bar{P}_{\mathrm{saved}} = 2.21 \times 10^{-3}$.

4.2.3 Conclusion on power consumption

The power required by the jets is high, which comes from the high velocity of the jets. As the power required is proportional to the cube of the mean velocity of the jet $\bar{P}_{\mathrm{jet}} \propto |\boldsymbol{v}_{\mathrm{jet}}|^3$, a parametric study of the velocity is performed. Also, frequency and slot width L_{jet} sensitivities are studied to potentially reduce the power consumption for the actuation.

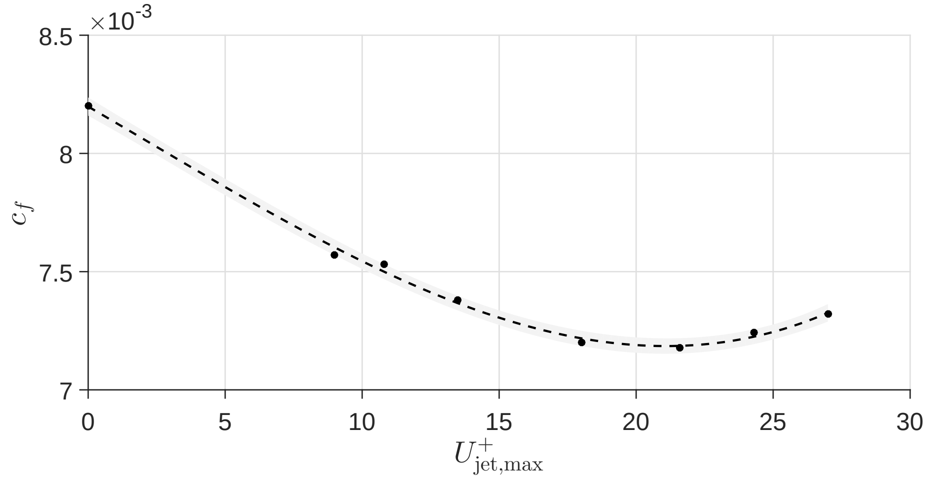

Figure 4.7: Skin friction coefficient sensitivity to $U^+_{\text{jet,max}}$. The dashed line corresponds to the third order trend line of the data and the shadowed area is an estimate of the standard deviation of the error in predicting a future value at another velocity.

4.3 Jet velocity sensitivity

Lower velocities of the jet are studied in this section. A sweep between $U^+_{\text{jet,max}} = 0$ to $U^+_{\text{jet,max}} = 27$ is performed and the skin friction coefficient corresponding to each velocity are plotted in figure 4.7.

No velocities have been studied where $U^+_{\text{jet,max}} < 8$ because the benefits of these lower velocities tend to give smaller skin friction reduction, and therefore, they are not interesting for this study.

The maximum reduction case simulated has been at $U^+_{\text{jet,max}} = 21.6$ with $C_f = 7.18 \times 10^{-3}$ and following the trend line, a minimum of the skin friction coefficient could be found at $U^+_{\text{jet,max}} \sim 20$. However, since the power decreases with the cube of the velocity, the lowest possible value of the velocity is sought without lowering the benefits in skin friction reduction. If the jet velocity is halved from the baseline case, $U^+_{\text{jet,max}} = 13.5$, the skin friction coefficient increases to $C_f = 7.38 \times 10^{-3}$ from the baseline value of $C_f = 7.32 \times 10^{-3}$, a 0.8% increase. The potential benefit lost from the maximum reduction case at $U^+_{\text{jet,max}} = 21.6$ is of 2.8%. However, this is compensated with the amount of power required from the jets being reduced by a factor of 8 from the baseline and a factor of 4 from the maximum reduction case.

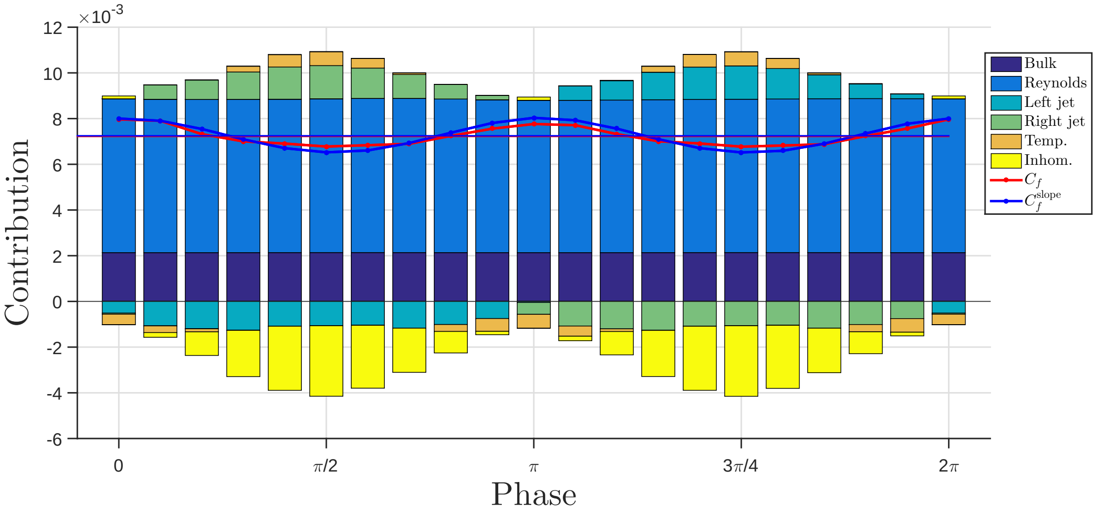

Figure 4.8: Friction coefficient contributions for $U^+_{\mathrm{jet,max}} = 13.5$ as a function of phase. Phase at $t = 0$ and $t = 2\pi$ are repeated for consistency. Straight lines represent the mean skin friction coefficient in total time for the traditional method (blue) and the FIK-E (red).

4.3.1 FIK-E analysis

The extended version of the method used by Fukagata et al. (2002), the FIK-E, that has been developed in section 3.2 is used to obtain the contributions that make the skin friction reduction possible.

The case of $U^+_{\mathrm{jet,max}} = 13.5$ is highlighted here since it provides a good trade-off between power expenditure and skin friction reduction. Applying the FIK-E to this case, figure 4.8 can be obtained.

Comparing these results with the ones of the baseline case (figure 3.6), one can clearly see that all contributions have been reduced considerably with the exception of the bulk contribution. This contribution, as demonstrated in section 3.2, only depends on the mean velocity of the flow.

The reduction of the jet velocity leads to smaller changes in the velocity of flow field, which is reflected by both the inhomogeneous and temporal contributions. The inhomogeneous term along the period of oscillation has been reduced a 79.1% of its value while the temporal amplitude decreased by 84.3%.

In the case of the jet contribution, plotted individually in figure 4.9, the negative contri-

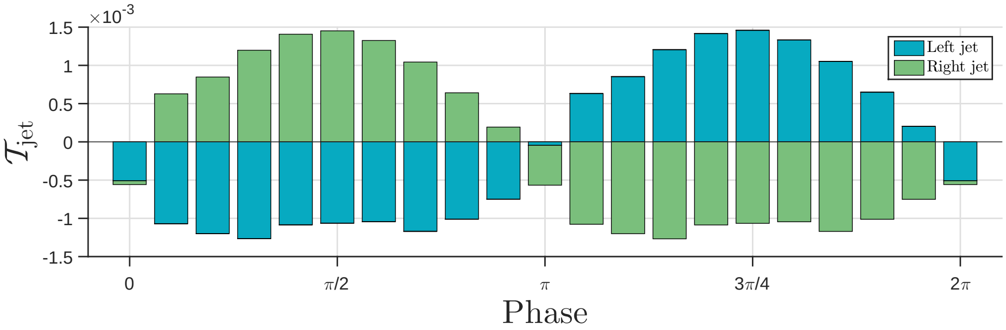

Figure 4.9: Jets boundary contribution for the half jet velocity case, $U^+_{\text{jet,max}} = 13.5$.

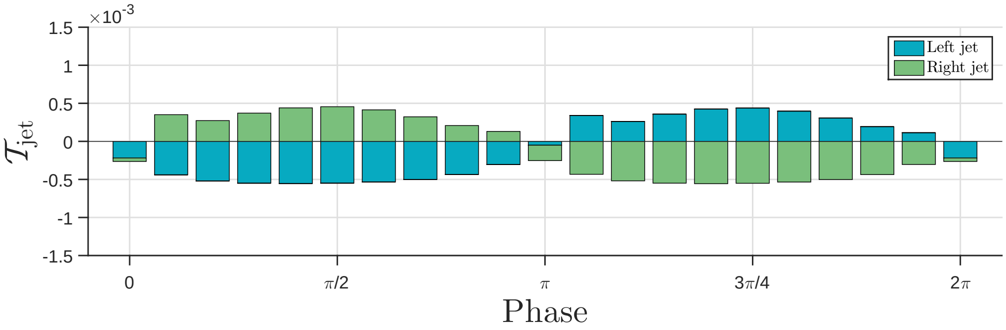

Figure 4.10: Jets boundary contribution for the case with $U^+_{\text{jet,max}} = 9$.

butions to the skin friction, i.e. the jet extracting air from the channel, has been decreased by 51.6% whereas the beneficial contributions of the blowing jet increase slightly (6.2%) while maintaining its value throughout the blowing (as opposed to decrease at the peak of the blowing like in the case of the baseline). This is because less area of flow field is affected and the jet plume cannot establish as well as in the baseline case and therefore, the gradient at the interface of the blowing jet is higher even though the velocity is reduced.

It is of interest to further reduce the velocity to explore the behaviour of this contribution, as shown in figure 4.10. At $U^+_{\text{jet,max}} = 9$, the blowing phase of each jet cannot sustain the plume in the flow field, making the gradient at the interface grow at the peak of the blowing phase. The reduction in skin friction is smaller in this case because the jets are not strong enough to make an impact in the flow field, reducing the inhomogeneous contribution too much (to 7.3% of the baseline case).

$U^+_{\text{jet,max}}$	C_f^{slope}	Bulk contr.	Reynolds contr.	Jets +	Jets -	Temp. amplitude	Inhom. contr.	C_f	Diff. (%)
0	8.20	2.13	5.94	-	-	-	0.03	8.10	-1.25
9	7.57	2.13	6.03	0.29	-0.46	0.29	-0.50	7.49	-1.06
10.8	7.53	2.13	6.13	0.36	-0.50	0.57	-0.70	7.42	-1.42
13.5	7.38	2.14	6.71	0.88	-1.02	0.62	-1.36	7.34	-0.57
18	7.20	2.14	7.40	1.21	-1.05	1.45	-2.53	7.16	-0.65
21.6	7.18	2.14	9.05	1.45	-1.07	2.49	-4.36	7.20	0.25
24.3	7.24	2.14	9.91	1.64	-1.07	3.31	-5.34	7.27	0.34
27	7.32	2.15	10.81	1.81	-0.96	3.92	-6.52	7.28	-0.52

Table 4.2: Contributions of the skin friction coefficient for cases with different $U^+_{\text{jet,max}}$. The value of C_f^{slope} has been obtained with (3.7) while C_f is the result of the FIK-E analysis. The columns 'Jets +' and 'Jets -' are the mean values of the jet contributions that increase and decrease the skin friction coefficient, respectively. The difference column is obtained as $C_f/C_f^{\text{slope}} - 1$. Columns 2-9 are multiplied by 10^3.

Both the jets and inhomogeneous contributions reduce the skin friction (and the temporal contribution, but its main effect is the skin friction oscillation around the mean value). However, one cannot forget about the Reynolds stress contribution, which increases the skin friction and the reason why this analysis is required. The Reynolds stress contribution drops with the maximum velocity of the jet, being reduced by 37.9% at $U^+_{\text{jet,max}} = 13.5$ and by 16.3% at $U^+_{\text{jet,max}} = 21.6$.

The detailed contributions of the different cases are reported in table 4.2.

4.4 Frequency sensitivity

A frequency sensitivity is performed to explore more options for the jets. The numerical simulations time step has to be changed in order to obtain 500 time steps per period. Two simulations at smaller periods of $T^+_{\text{osc}} = 62.5$ and $T^+_{\text{osc}} = 93.75$ are performed, with time steps of $\Delta t^+ = 0.125$ and $\Delta t^+ = 0.1875$, respectively. Another two simulations with higher periods of $T^+_{\text{osc}} = 187.5$ and $T^+_{\text{osc}} = 250$ are performed, with time steps of $\Delta t^+ = 0.375$ and $\Delta t^+ = 0.5$, respectively. The resultant skin friction coefficient is shown in figure 4.11.

The data obtained in this sensitivity results in different behaviours when the period increases or decreases. This is why the confidence in the trend line is lower than in the previous

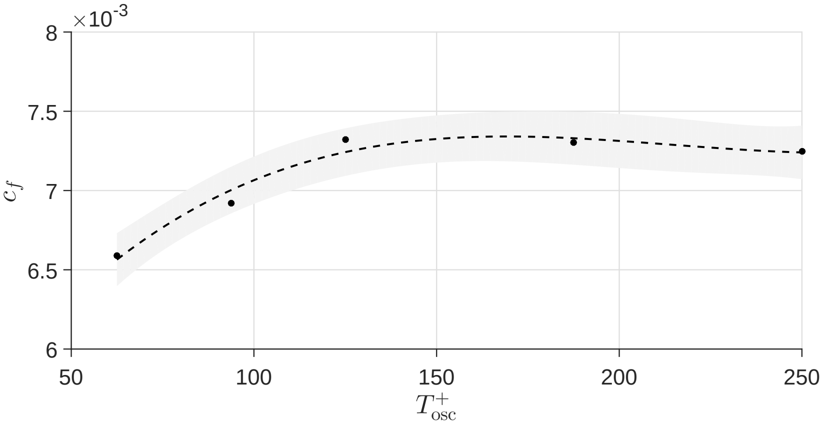

Figure 4.11: Skin friction coefficient sensitivity to T^+_{osc}. The dashed line corresponds to the third order trend line of the data and the shadowed area is an estimate of the standard deviation of the error in predicting a future value at another period.

case. When the period is lowered, that is, when the frequency of the jets is higher, the friction coefficient tends to decrease in an almost linear fashion. However, when the jets oscillate slower, the behaviour does not change significantly. A minimum appears to be between the baseline case and the double period case, but more simulations should be performed in this area to confirm it.

In order to explore further the implications of the jets, a steady case of the jets on (i.e. $T^+_{\text{osc}} \to \infty$) is simulated. This system could not use the device proposed in section 4.2, but it is worth to study this case nevertheless, as the resultant skin friction when the period is increased should tend to this value. For a continuous jet operation, blowing in one side and extracting air from the domain in the other side of the device, the skin friction coefficient is $C_f = 5.22 \times 10^{-3}$. This is a very low value compared with the ones from previous cases. According to figure 4.11, the friction coefficient decreases when the period is increased but the trend is not as pronounced to suggest the value obtained with $T^+_{\text{osc}} \to \infty$. More cases should be simulated to better understand the sensitivity to this parameter at higher T^+_{osc}.

4.4.1 FIK-E analysis

Applying the FIK-E method to the case with the oscillation period of $T^+_{\text{osc}} = 62.5$, the following figure is obtained:

Comparing the results at smaller oscillating periods with the baseline case (figure 3.6),

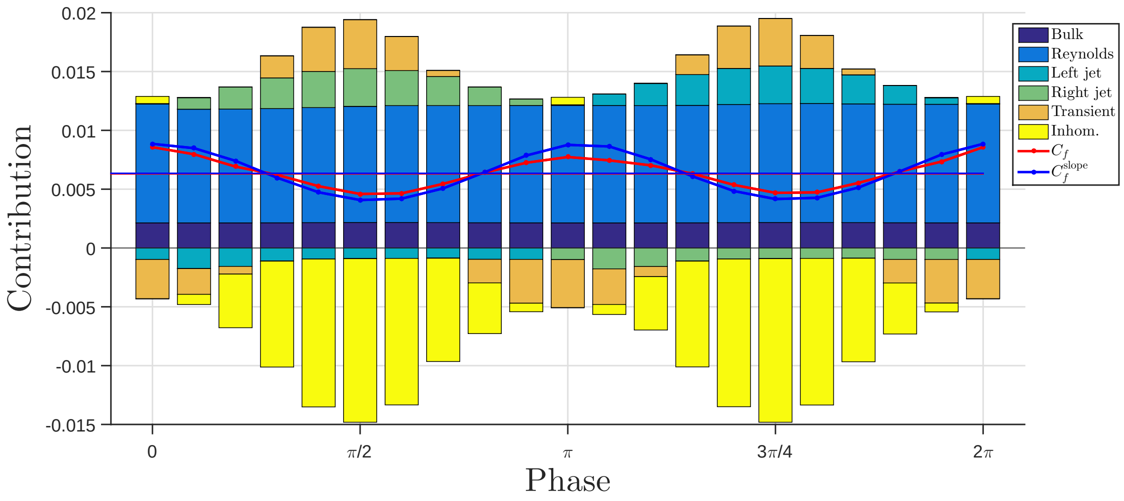

Figure 4.12: Friction coefficient contributions for $T^+_{\text{osc}} = 62.5$ as a function of phase. Phase at $t = 0$ and $t = 2\pi$ are repeated for consistency. Straight lines represent the mean skin friction coefficient in total time for the traditional method (blue) and the FIK-E (red).

there are no significant differences. The friction coefficient line for the FIK-E method cannot *follow* the changes in the flow as well as in the baseline case, even though the difference in the mean value is still small (-0.83%).

One may think that the inhomogeneous contribution would further decrease the friction coefficient, but, as summarised in table 4.3, the contrary is true. The flow field takes some time to adjust to the velocity imposed by the jets, and a frequency higher than the baseline implies the flow field has less time to *react* to the velocity ejected or extracted. This is further emphasised by the jets contribution, which increases in both terms as frequency does, as the gradient near the boundary condition is higher when the flow is not settled. The most contributor to the reducing of the skin friction is the Reynolds stress contribution, as less flow is altered, reducing its effects from the baseline case.

The result of the FIK-E method for the oscillation period of $T^+_{\text{osc}} = 250$ is plotted in figure 4.13.

In this case, a very different distribution of the skin friction contributions is found. The inhomogeneous contribution appears to behave similarly to the baseline case but the Reynolds stress contribution oscillates more wildly than the other cases previously studied. On the

T^+_{osc}	C_f^{slope}	Bulk contr.	Reynolds contr.	Jets +	Jets -	Temp. amplitude	Inhom. contr.	C_f	Diff. (%)
62.5	6.59	2.15	9.95	1.94	-1.10	4.13	-6.42	6.53	-0.83
93.75	6.92	2.14	10.13	1.86	-1.07	4.05	-6.47	6.86	-0.98
125	7.32	2.15	10.81	1.81	-0.96	3.92	-6.52	7.28	-0.52
187.5	7.30	2.15	10.89	1.78	-1.59	3.01	-6.00	7.25	-0.71
250	7.25	2.15	10.91	1.81	-1.05	3.09	-6.56	7.24	-0.11
∞	5.22	2.16	14.21	3.01	-0.84	-	-13.32	5.23	0.03

Table 4.3: Contributions of the skin friction coefficient for cases with different T^+_{osc}. The value of C_f^{slope} has been obtained with (3.7) while C_f is the result of the FIK-E analysis. The columns 'Jets +' and 'Jets -' are the mean values of the jet contributions that increase and decrease the skin friction coefficient, respectively. The difference column is obtained as $C_f/C_f^{\text{slope}} - 1$. Columns 2-9 are multiplied by 10^3.

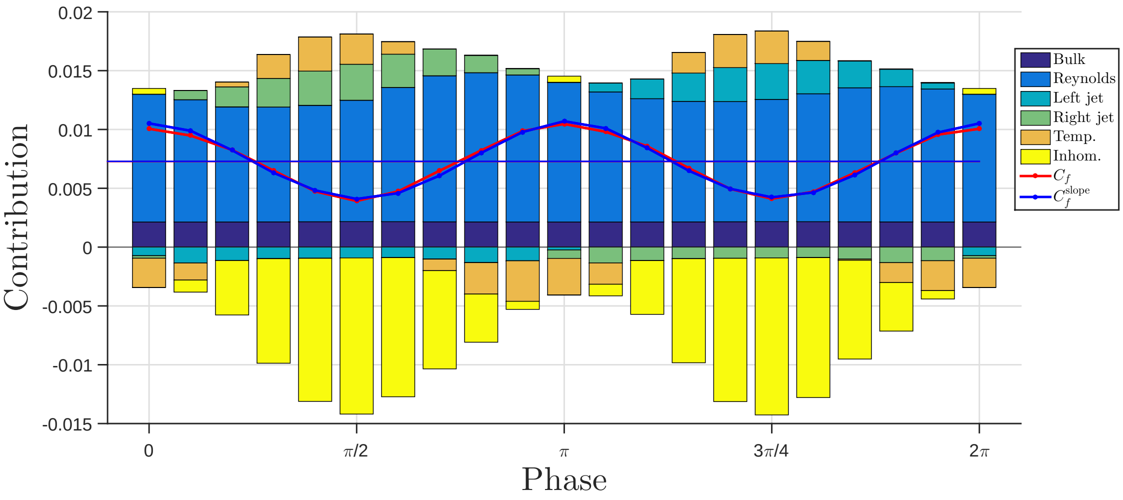

Figure 4.13: Friction coefficient contributions for $T^+_{\text{osc}} = 250$ as a function of phase. Phase at $t = 0$ and $t = 2\pi$ are repeated for consistency. Straight lines represent the mean skin friction coefficient in total time for the traditional method (blue) and the FIK-E (red).

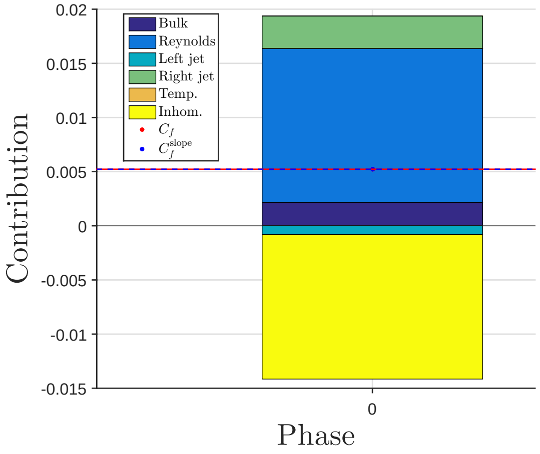

Figure 4.14: Friction coefficient contributions for $T^+_{\text{osc}} \rightarrow \infty$. Straight lines represent the mean skin friction coefficient for the traditional method (blue) and the FIK-E (red).

other hand, the temporal contributions are reduced in size from the low period cases. A clear conclusion for the contributions of the skin friction cannot be drawn from the higher period cases and more cases are to be simulated to obtain a better understanding for these contributions.

When the jets are kept constant, i.e. when $T^+_{\text{osc}} \rightarrow \infty$, the contributions are the ones presented in figure 4.14.

The temporal contribution is identically zero as there is only one *phase*. The inhomogeneous contribution almost completely compensates the Reynolds stresses contribution. It is interesting to see how the boundary condition of the blowing jet (left jet) is very small compared to the sucking jet (right jet), which is in line with the physics commented in section 3.4.4.

4.5 L^+_{jet} sensitivity

The original idea for the jets was to mimic the oscillating wall with a more practical approach. The idea of this sensitivity started to make the jets similar to an oscillating wall. The way it was thought is to shorten the space between the jets to create a layer that was isolated from the channel flow. This concept made the air blown from one jet to enter the opposite slot.

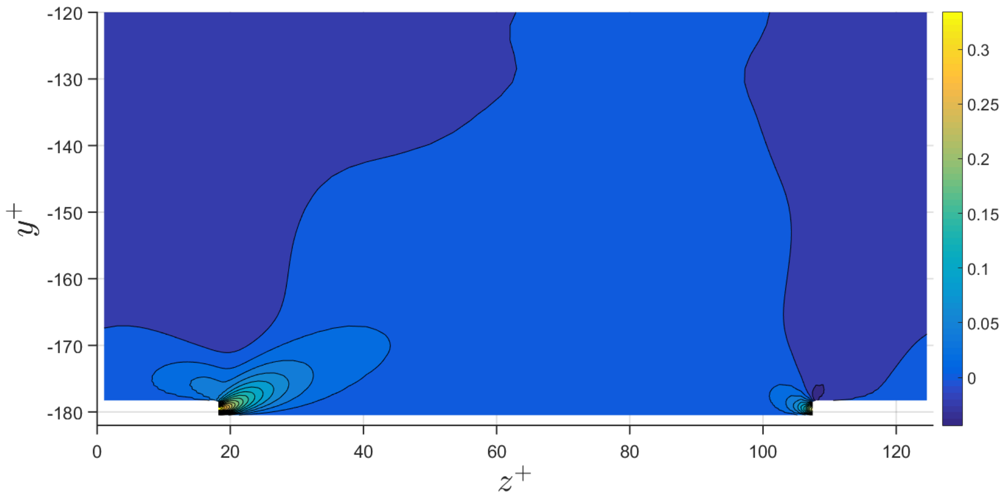

Figure 4.15: Contour plot of the velocity in the z direction for the baseline configuration with $L^+_{\text{jet}} = 90$. The values are normalised with the bulk velocity u_b.

The problems with this idea are that the space between jets should be very small or the velocity of the jets should be very high in order for the ejected plume to reach the other slot. However, the idea to shorten the distance L^+_{jet} is an interesting case to explore. For that, L^+_{jet} is reduced from 90 to 27, consequently reducing L^+_z from $4\pi/3$ to $2\pi/3$. All other parameters are kept the same as in the baseline.

For the mesh parameters, the spacing in the z direction has been reduced from $\Delta z^+ = 0.5 \sim 3.80$ to $\Delta z^+ = 0.5 \sim 1.51$ to be more accurate in the jet wall. Even though the cell spacing is reduced, the total number of cells in the z direction is reduced from the original $n_z = 504$ to $n_z = 384$. The x and y directions are kept as the baseline mesh.

The jet influence in this simulation presents a similar behaviour to the baseline case. However, since the space between the jets is shorten drastically, the portion affected by the jets is bigger than in the previous case. In fact, at the peak of the operation of the jets, the plume from one jet affects the flow near the opposite jet, which does not happen in the baseline case. Figure 4.15 and 4.16 show the comparison of contour plots of the velocity in the z direction with the baseline.

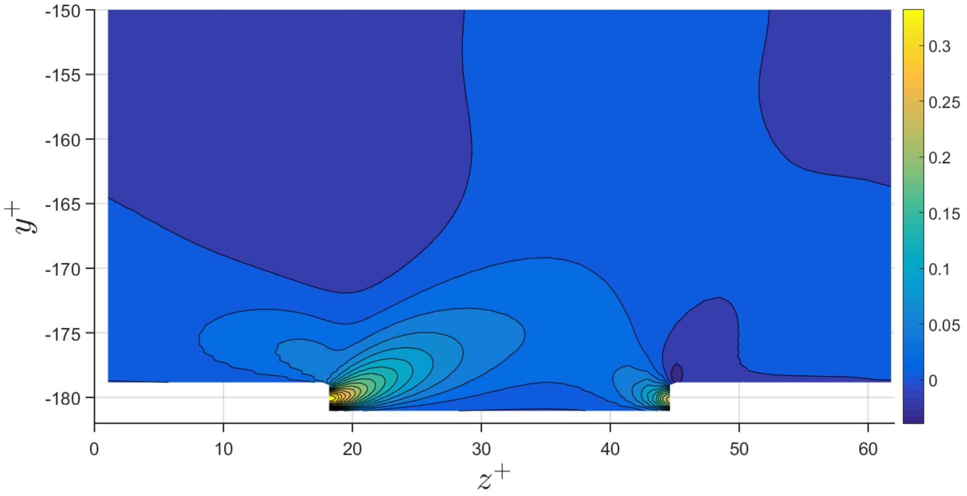

Figure 4.16: Contour plot of the velocity in the z direction for the baseline configuration with $L^+_{\text{jet}} = 27$. The values are normalised with the bulk velocity u_b.

4.5.1 FIK-E analysis

The differences that present this case can be appreciated not only in the skin friction reduction, but in the analysis with the FIK-E, in figure 4.17 and table 4.4.

The values of the jet, temporal and inhomogeneous contributions have been doubled as the flow near the wall is changed drastically. If the Reynolds stress contribution had increased proportionally, this would have only increased the oscillations of the skin friction coefficient. However, the flow near the jet adapts to the jet flow faster, making it more laminar since the jet plume has less perturbation associated due to the boundary condition value, which does not increase the Reynolds stress contribution proportionally.

In the case of $L^+_{\text{jet}} = 27$, the reduction in drag obtained is of 57.2% which is a large increase from the baseline case. However, since the number of jets has to be doubled to cover the same span as the baseline (figure 4.15 and 4.16), the effective reduction would be 28.6%. It is still a noticeable increase of efficiency, which could lead to even more beneficial skin friction reductions if more cases are explored. More cases should be run with intermediate L^+_{jet} to fully understand the behaviour of the flow.

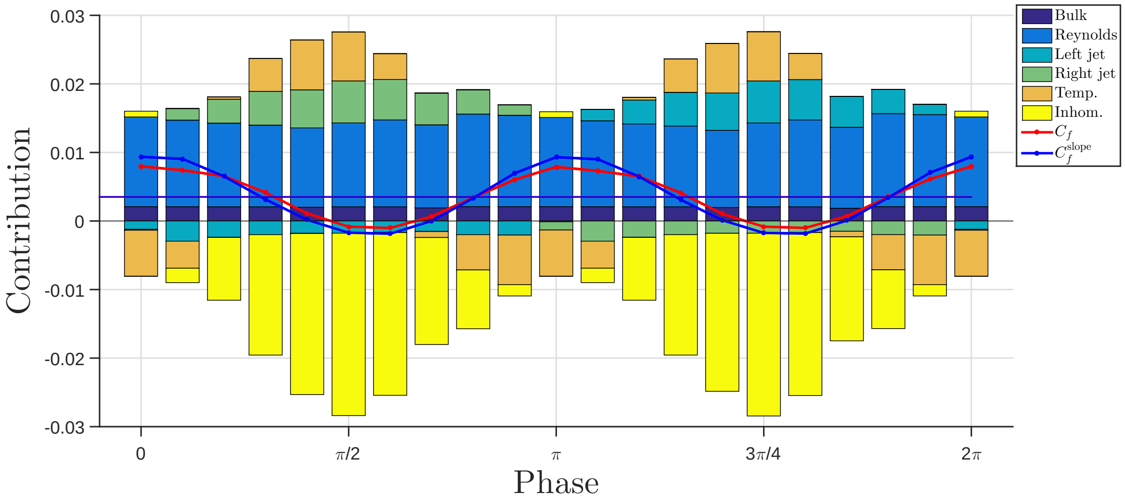

Figure 4.17: Friction coefficient contributions for $L^+_{\text{jet}} = 27$ as a function of phase. Phase at $t = 0$ and $t = 2\pi$ are repeated for consistency. Straight lines represent the mean skin friction coefficient in total time for the traditional method (blue) and the FIK-E (red).

L^+_{jet}	C_f^{slope}	Bulk contr.	Reynolds contr.	Jets +	Jets -	Temp. amplitude	Inhom. contr.	C_f	Diff. (%)
27	3.50	2.05	12.48	3.72	-1.93	7.26	-12.73	3.54	1.08
90	7.32	2.15	10.81	1.81	-0.96	3.92	-6.52	7.28	-0.52

Table 4.4: Contributions of the skin friction coefficient for cases with different L^+_{jet}. The value of C_f^{slope} has been obtained with (3.7) while C_f is the result of the FIK-E analysis. The columns 'Jets +' and 'Jets -' are the mean values of the jet contributions that increase and decrease the skin friction coefficient, respectively. The difference column is obtained as $C_f/C_f^{\text{slope}} - 1$. Columns 2-9 are multiplied by 10^3.

β(deg)	C_f^{slope}	Bulk contr.	Reynolds contr.	Jets +	Jets -	Temp. amplitude	Inhom. contr.	C_f	Diff. (%)
30	10.77	2.13	15.86	0.08	-0.19	10.28	-6.86	10.71	-0.54
45	8.81	2.15	15.59	0.65	-0.29	9.24	-9.14	8.88	0.73
60	7.84	2.16	14.81	1.28	-0.50	7.69	-9.83	7.90	0.80
70	7.43	2.15	12.67	1.66	-0.80	5.59	-8.30	7.38	-0.70
75	7.32	2.15	10.81	1.81	-0.96	3.92	-6.52	7.28	-0.52

Table 4.5: Contributions of the skin friction coefficient for cases with different β. The value of C_f^{slope} has been obtained with (3.7) while C_f is the result of the FIK-E analysis. The columns 'Jets +' and 'Jets -' are the mean values of the jet contributions that increase and decrease the skin friction coefficient, respectively. The difference column is obtained as $C_f/C_f^{\text{slope}} - 1$. Columns 2-9 are multiplied by 10^3.

4.6 β angle sensitivity

The sensitivity to the ejection angle of the jets is already presented in section 2.7.3.2. In this section, the contributions that make the $\beta = 75\,\text{deg}$ the optimum case are to be studied.

4.6.1 FIK-E analysis

The contributions of the different configurations of jets regarding a change in β are reported in table 4.5. Unfortunately, the cases where $\beta = 0$ and $\beta = 15\,\text{deg}$ are not statistically convergent when phase averaged. The cases from $\beta = 30\,\text{deg}$ are reported.

It is clear from the data that the spanwise component of the jets increases the Reynolds contribution. In order to reduce it, the direction of the jets in the spanwise component should be minimised. However, the inhomogeneous contribution relies on both the spanwise velocity and the streamwise velocity. At $\beta = 60\,\text{deg}$, the inhomogeneous contribution is maximum because the combined action of the streamwise flow and the jet flow direction maximises its product and the derivatives in I_x. Even though $\beta = 60\,\text{deg}$ should be the case of maximum skin friction reduction, the Reynolds contribution decreases more rapidly from $\beta = 60\,\text{deg}$ to $75\,\text{deg}$ than the inhomogeneous contribution does, as it can be observed in figure 4.18.

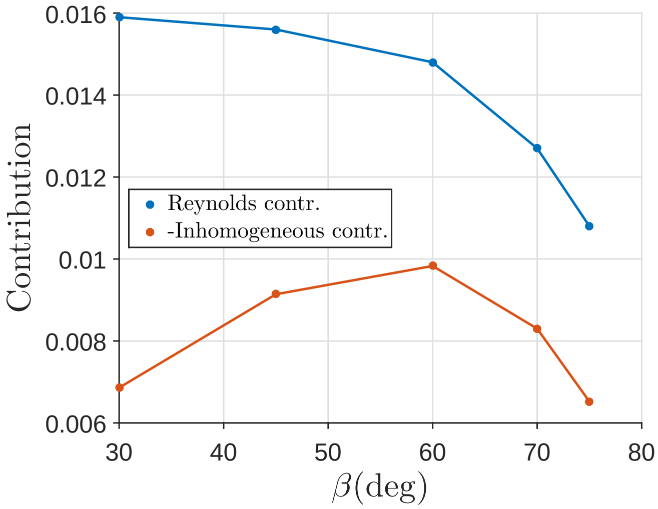

Figure 4.18: Comparison of the Reynolds and Inhomogeneous contributions as a function of the jet angle β.

4.7 Conclusions

All parameters studied have a significant impact on the skin friction reduction or increase of the WT-ZMJ. Identifying the contributions affected by each parameter is key to understand the jets influence:

- The inhomogeneous contribution is the one that helps the most by reducing the negative effects of the Reynolds contribution. Modifying the velocity field in both streamwise and spanwise components in a balanced way maximises the benefits from this term.
- The Reynolds contribution is higher the more the flow is disturbed in the spanwise component. On the other hand, near the jet plume, the perturbations from the ensemble mean velocities are reduced as the boundary condition values are injected without perturbation.
- As a result of the jet velocity being reduced, the Reynolds stresses term is reduced as well as the inhomogeneous term. However, the former is reduced faster than the latter, which is of interest in the case of reducing the power spent on the operation of the jets, as the power of the jets is proportional to the cube of the velocity.

- The temporal contribution does not affect the skin friction if the average of its value is taken. It only affects the amplitude of the oscillation. This term could be of importance if the vibrations of the device are taken into account.

- The jet wall L_{jet} plays an important role on the skin friction coefficient, as the inhomogeneous contribution increases enormously when it is reduced. However, more simulations should be performed in order to identify whether there is a combination with other parameter, such as the velocity of the jet, that synergises and produces an amplified effect like the one obtained in figure 4.17.

The flow with wall tangential zero-mass jets installed is a very complex flow that have more parameters yet to be studied. In this chapter, a preliminary investigation of some of the parameters has been shown, but there are many interactions with other parameters that could lead to more beneficial outcomes. Also, more configurations of the parameters studied should be simulated in future work to obtain a clearer view of the mechanisms that take place in the skin friction reduction.

One of the parameters that is of paramount importance is the streamwise incoming flow. Obtaining the jets effectiveness in higher Reynolds number flow would be of enormous interest.

Chapter 5

Proof of concept towards application

5.1 Introduction

The research conducted in Wall Tangential Zero Mass Jets has been through the use of DNS of the channel flow at a bulk Reynolds number of $Re_b = 2800$. However, the intention is to place these devices in the fuselage of an aircraft, which works in a regime of Reynolds numbers of around $Re \sim 10^6$.

In order to explore what the potential benefits of the WT-ZMJ could be, one can approach the challenge in different ways. Nowadays, as commented in section 2.4, using DNS to simulate the flow around a fuselage is completely infeasible. A RANS simulation is used in these cases where the Reynolds number is very high. Mele and Tognaccini (2012) and Mele and Tognaccini (2016) extended the classical Wilcox boundary condition (Wilcox et al. (1998)) for rough walls in order to represent riblets. Another way to represent phenomena occurring near the wall is the method proposed by Aupoix et al. (2012), which consists in modifying the turbulence model to represent the DNS conditions. This is the method followed and extended in this chapter.

The idea of this chapter is to observe the flow characteristics from DNS results, mainly the velocity profile, and build a turbulence model from the one proposed by Spalart and Allmaras (1992) to work in RANS simulations.

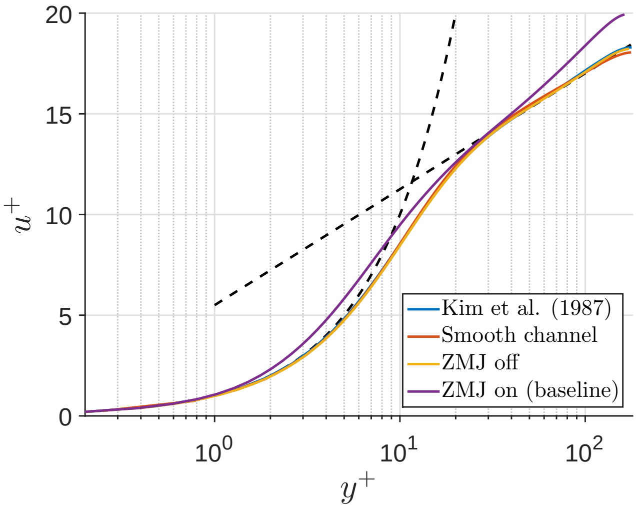

Figure 5.1: Velocity profile of different DNS cases. Dashed lines correspond to the viscous sublayer and logarithmic layer approximate equations (1.4).

5.1.1 Logarithmic layer changes due to ZMJ

The velocity profile of the smooth channel flow from Kim et al. (1987), from section 2.5.3 and the baseline case geometry with ZMJ off and on are plotted in figure 5.1. All viscous units in this chapter (denoted by the superscript +) are scaled with the friction velocity u_τ^* corresponding to its simulation unless otherwise stated.

The results from the smooth channel and baseline case with jets off are very similar (i.e. in terms of velocity profile, skin friction, Reynolds stresses...). When the jets are active, the logarithmic layer slope increases. The idea to reproduce this behaviour in a RANS simulation is to obtain a set of parameters in the turbulence model that matches the data from the DNS results.

5.2 RANS simulation of the channel flow using S–A model

Shefflow can simulate RANS simulations using the S–A turbulence model (Spalart and Allmaras (1992)). The model is described in section 2.4.1.1, which adds an extra equation to the Reynolds average Navier-Stokes equations in order to solve the closure problem.

For the S–A turbulence model to be accurate, there is a mesh requirement, which is that

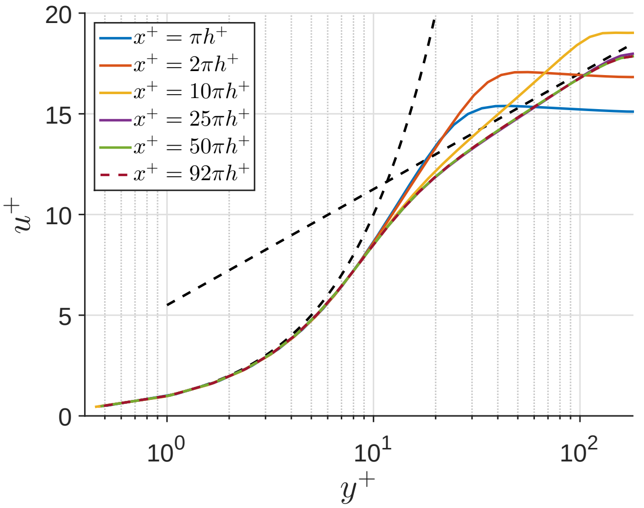

Figure 5.2: Velocity profiles at different x positions along the channel flow simulated in RANS using S–A turbulence model.

the height of the first cell from the wall has to be $y^+ < 1$. The length of the channel has to be much longer than in the DNS because inlet and outlet conditions are set instead of periodic boundary conditions at the beginning and end of the domain. Therefore, the flow has to develop from a uniform flow to the turbulent flow profile. Velocity profiles of the flow at different stages are captured in figure 5.2.

Velocity profiles are recorded at a distance of $x^+ = 92\pi h^+$, where the flow is converged and it is far enough from the outflow boundary conditions to not be affected by numerical errors. The mesh details for the channel to simulate the flow in RANS are gathered in table 5.1.

The S–A turbulence model parameters are chosen to properly capture a set of canonical cases. In some cases, these parameters are able to obtain good results but not completely accurate, as it is a model. Figure 5.3 shows the comparison between the smooth channel flow resolved by means of DNS and RANS using the S–A turbulence model.

As it can be seen, the velocity profile could be corrected. Section 5.3 explains how this model can be improved for the channel flow at very low Reynolds numbers ($Re_\tau = 180$, $Re_b = 2800$).

Parameter	Value	Parameter	Value
L_x^+	$96\pi h^+$	Re_b	2800
L_y^+	$2h^+$	Re_τ	180
Δx^+	28.59	u_b^*	42 m/s
Δy_w^+	0.48	u_τ^*	2.7 m/s
ν^*	$1.5 \times 10^{-5}\mathrm{m}^2/\mathrm{s}$	h^*	0.001 m
$p*$	16063 Pa	T^*	110.0 K

Table 5.1: Parameters of the simulation for the channel flow using RANS.

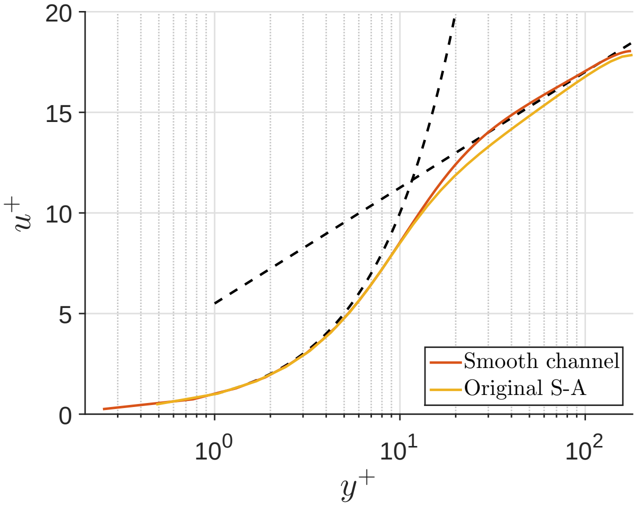

Figure 5.3: Velocity profiles of the channel flow simulated with DNS and RANS using S–A turbulence model.

Parameter	Value	Parameter	Value
L_x^+	$144\pi h^+$	Re_b	125000
L_y^+	$2h^+$	Re_τ	5200
Δx^+	67.05	u_b^*	1 m/s
Δy_w^+	0.56	u_τ^*	41.5 mm/s
ν^*	$8 \times 10^{-6}\text{m}^2/\text{s}$	h^*	1 m
$p*$	50090 Pa	T^*	142.4 K

Table 5.2: Parameters of the simulation for the channel flow of $Re_b = 125000$ using RANS.

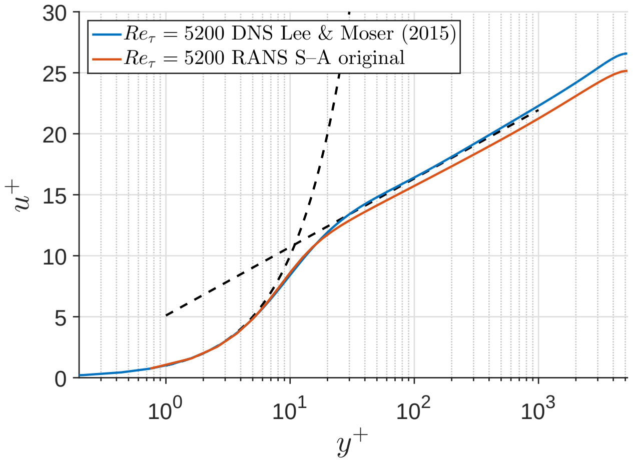

Figure 5.4: Velocity profiles of the smooth channel flow simulated with DNS from Lee and Moser (2015) and RANS using the original S–A turbulence model.

5.2.1 RANS simulation of a channel flow of $Re_b \sim 10^5$ using S–A model

For higher Reynolds numbers, a similar situation is found. A smooth channel flow of $Re_\tau = 5200$ is studied, which implies $Re_b = 125000$. The dimensions of the channel are found in table 5.2.

The length of the channel required to have a converged solution has increased. In order to compare with DNS, the results obtained by Lee and Moser (2015) for the smooth channel flow are used, which are available in a public database. As in section 5.2, the original S–A turbulence model approximates to the DNS solution but could be improved. The velocity profile is shown in figure 5.4.

5.3 Methodology to obtain the turbulence model calibrated by DNS data

Aupoix et al. (2012) wanted to simulate the flow details at riblet level for a realistic configuration. Unfortunately, this is impractical as the Reynolds number is very high for these applications. They proposed different strategies to model riblets for these flows:

- by shifting the velocity profile in the law of the wall as a representation of the change of skin friction due to the action of the riblets,
- by modifying the turbulence model to reproduce this same shift, as they affect the flow in the wall region.

In this chapter, the second strategy is adopted and extended to the case of the jets, which show not only a shift but a tilt in the logarithmic region (figure 5.1).

The first parameter studied is the one that Aupoix et al. (2012) studies, c_{v1}, which controls the model behaviour in the wall region, specially in the viscous sublayer. Since this layer is directly responsible for the gradient at the wall, it contributes to the value of the friction velocity. As the scaling of the viscous units depends on this value, this parameter shifts the logarithmic layer as can be seen in figure 5.5. The velocity profiles have been scaled both with the baseline $u_\tau^* = 2.7$ m/s on the left and with their own u_τ^* on the right.

Looking at figure 5.5a, it is clear the effect on the viscous sublayer, as the logarithmic region is almost coincident. Also, it affects the development of the velocity profile in the buffer region. However, when the scaling is applied for each simulation in figure 5.5b, the effects of the new friction velocity show as the mentioned shift in the logarithmic layer. Increasing c_{v1} reduces the velocity gradient at the wall and consequently, decreases the friction velocity and skin friction.

In order to tilt the logarithmic layer, the parameter c_{b1} is used. It can be found in the production term in the transport equation for the eddy viscosity. It is also a part in the destruction term as, for the logarithmic layer, there is an equilibrium between the production, diffusion and destruction terms with $c_{\mathrm{w1}} = c_{\mathrm{b1}}/\kappa^2 + (1 + c_{\mathrm{b2}})\,\sigma$. Varying c_{b1}, the velocity profiles of figure 5.6 are obtained.

The inclination of the logarithmic layer can be seen in both plots, whether they are scaled with the baseline friction velocity or their own. The parameter c_{b1} appears in the equation multiplying directly to κ, which is why it has a noticeable effect in the behaviour of the slope

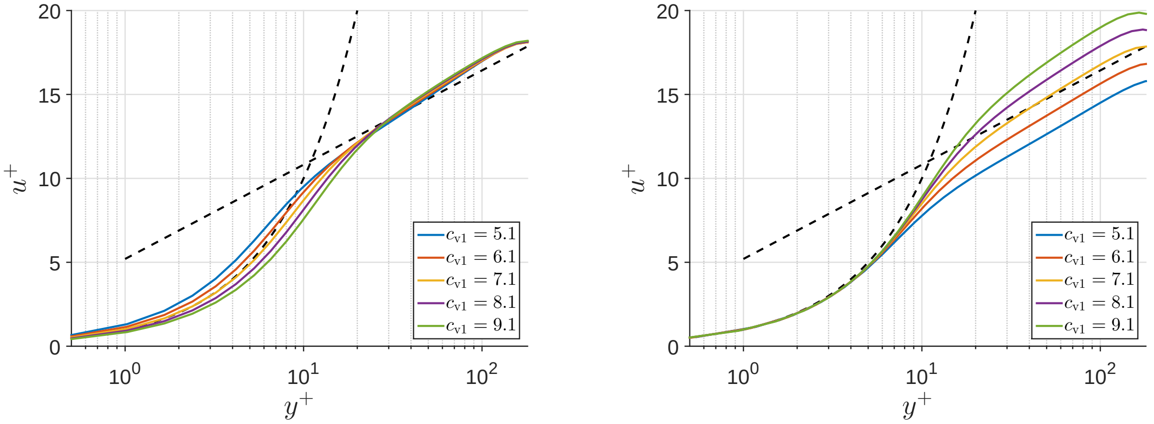

(a) Baseline u_τ^*.

(b) Own u_τ^*.

Figure 5.5: Velocity profiles of the channel flow using S–A turbulence model with a different parameter from the original $c_{\mathrm{v1}} = 7.1$.

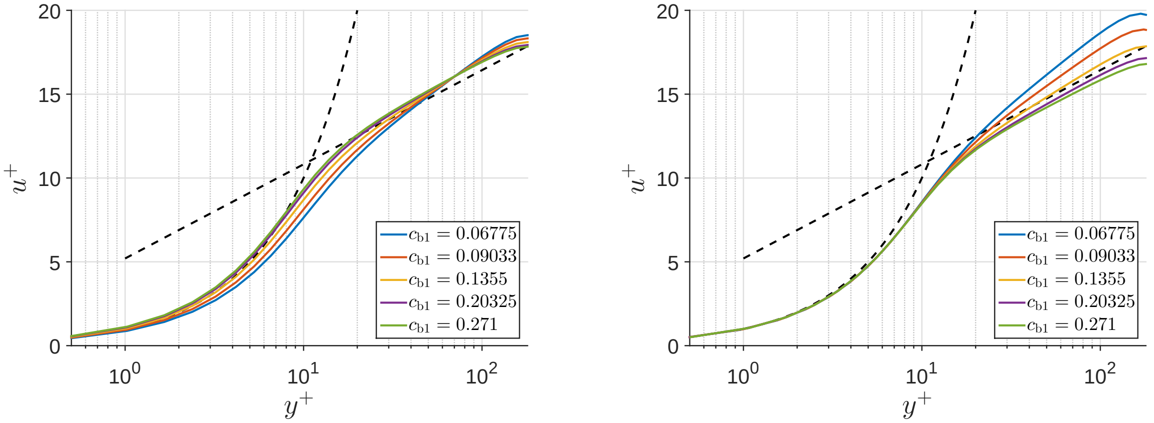

(a) Baseline u_τ^*.

(b) Own u_τ^*.

Figure 5.6: Velocity profiles of the channel flow using S–A turbulence model with a different parameter from the original $c_{\mathrm{b1}} = 0.1355$.

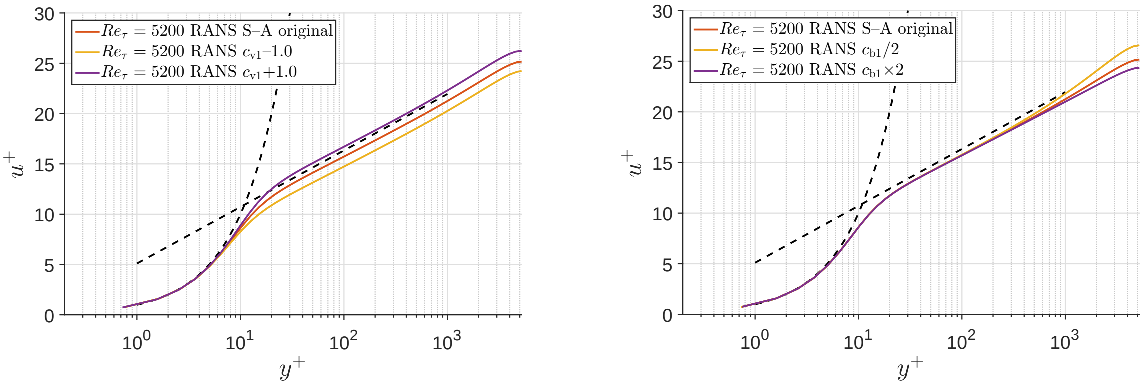

(a) Change in c_{v1}. (b) Change in c_{b1}.

Figure 5.7: Velocity profiles of the smooth channel flow at $Re_\tau = 5200$ using S–A turbulence model with different c_{v1} and c_{b1} parameters from the original.

of the logarithmic layer. Even though c_{b1} mostly impacts the logarithmic layer, it also has an effect on the friction coefficient, lowering it as c_{b1} decreases its value.

With the ability to shift and tilt the logarithmic layer profile, one can relate DNS with the RANS simulations regarding the velocity profile in the logarithmic layer.

5.3.1 Turbulence model parameters effect in $Re_b \sim 10^5$

Similarly, both parameters are individually modified to observe their effects on the flow. The resultant velocity profiles of the simulations with different parameters can be appreciated in figure 5.7.

It can be seen how the effects of c_{b1} are transported further from the wall, at $y^+ > 3 \times 10^2$. The effect of c_{v1} still remains to shift the logarithmic layer.

5.4 Modelling of the channel flow using RANS

In order to model the effects of the jets in a channel flow, the methodology in section 5.3 is applied. A RANS solution that provides the same velocity profile in the logarithmic layer can be found by a set of S–A turbulence model parameters.

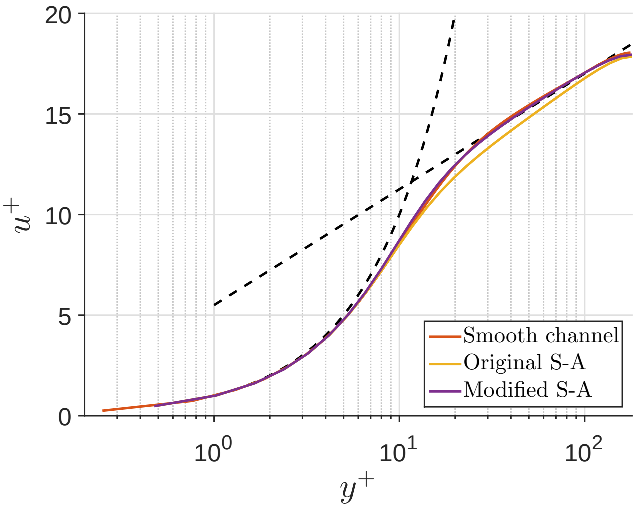

Figure 5.8: Velocity profiles of the smooth channel flow simulated with DNS and RANS using the modified S–A turbulence model.

5.4.1 Smooth channel

First, the smooth channel velocity profile is obtained with the set $(c_{\text{v1}}, c_{\text{b1}}) = (8.15, 0.240)$. The comparison of the DNS and the RANS simulations is shown in figure 5.8.

The friction coefficients of the DNS and RANS simulations are $c_f = 8.20 \times 10^{-3}$ and $c_f = 8.21 \times 10^{-3}$, respectively. The difference between the two simulations is of 0.17%.

5.4.1.1 Smooth channel at $Re_b \sim 10^5$

By increasing the value of c_{v1} to 7.8 and reducing the value of c_{b1} to 0.10, a better fit to the one in section 5.2.1 is obtained, as can be seen in figure 5.9.

The friction coefficients of the DNS and RANS simulations of the channel at $Re_b = 125000$ are $c_f = 3.44 \times 10^{-3}$ and $c_f = 3.51 \times 10^{-3}$, respectively. The difference between the two simulations is of 1.95%.

5.4.2 Channel with ZMJ off

For the channel with jets off, another RANS simulation is performed to find the set of parameters that would represent the case accurately. This set is $(c_{\text{v1}}, c_{\text{b1}}) = (7.80, 0.176)$ and the

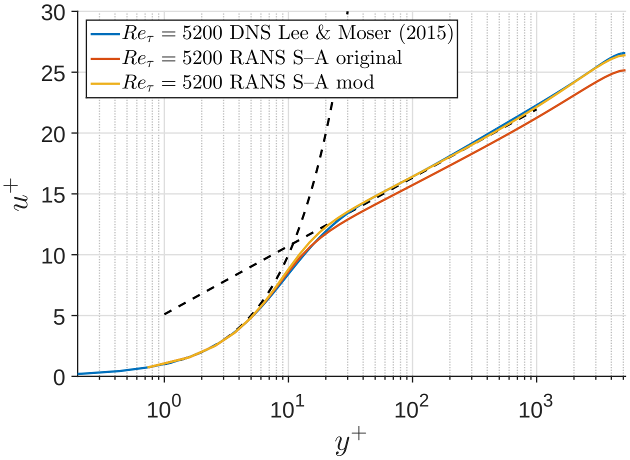

Figure 5.9: Velocity profiles of the smooth channel flow simulated with DNS from Lee and Moser (2015) and RANS using the modified S–A turbulence model.

comparison of the velocity profiles of the two simulations is plotted in figure 5.10.

The friction coefficients of the DNS and RANS simulations of the channel with jets off are $c_f = 8.20 \times 10^{-3}$ and $c_f = 8.21 \times 10^{-3}$, respectively. The difference between the two simulations is of 0.08%.

5.4.3 Channel with ZMJ on

A similar procedure to the one of the previous section is followed for the channel with jets on for different jet configurations. As an example, the velocity profiles of different jet velocities are plotted in figure 5.11 comparing their outcomes in DNS and RANS with the modified S–A turbulence model.

The aim is to approximate the logarithmic layer with this method. However, the buffer layer cannot be approximated correctly and it follows a similar pattern as the original turbulence model. The values of c_{v1} and c_{b1} are plotted in figure 5.12, 5.13 and 5.14 for variations in β, $U_{\mathrm{jet,max}}$ and T_{osc}, respectively. All data is gathered in table 5.3. The case with different L_{jet} could not be reproduced with this method, as the jets modify substantially the behaviour of the velocity profile.

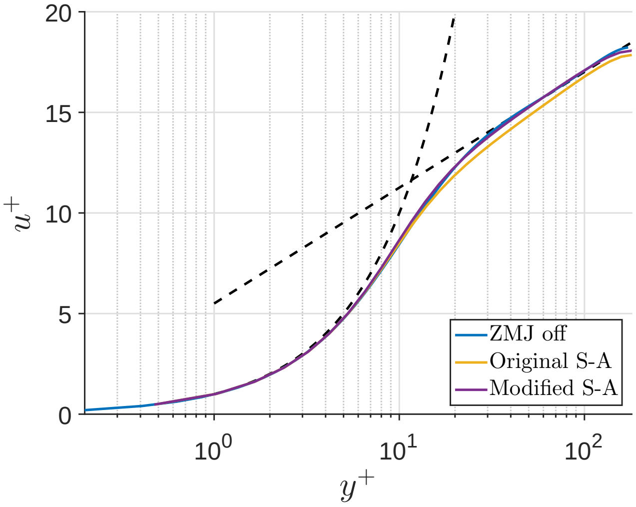

Figure 5.10: Velocity profiles of the channel flow with ZMJ off simulated with DNS and RANS using the modified S–A turbulence model.

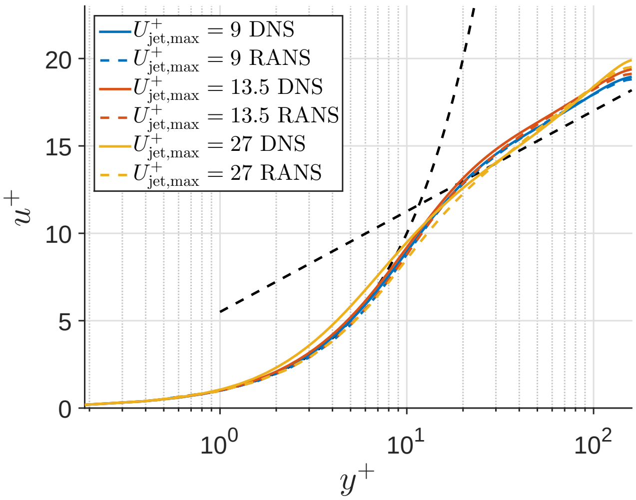

Figure 5.11: Velocity profiles of the smooth channel flow simulated with DNS and RANS using the modified S–A turbulence model.

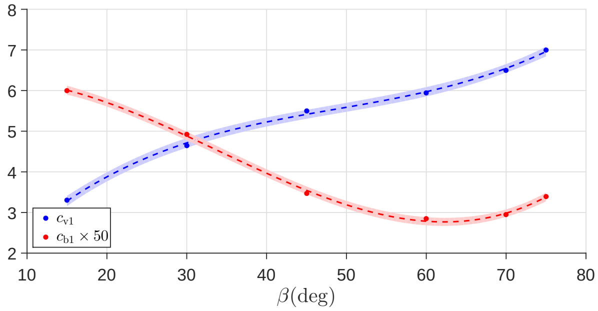

Figure 5.12: Set of parameters of the modified S–A turbulence model to represent the WT-ZMJ configurations with different jet angles β.

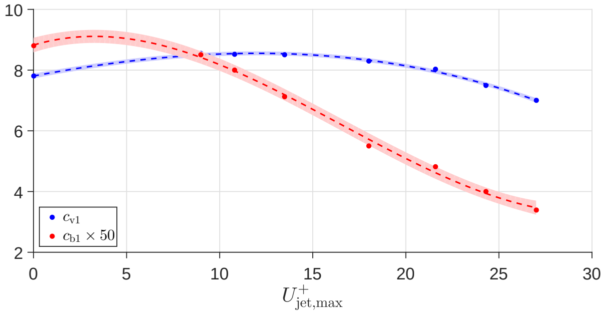

Figure 5.13: Set of parameters of the modified S–A turbulence model to represent the WT-ZMJ configurations with different maximum jet velocities $U_{\mathrm{jet,max}}$.

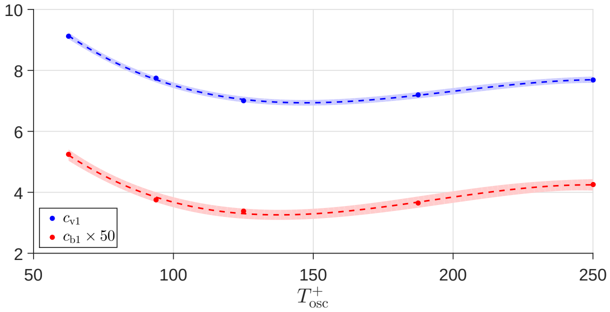

Figure 5.14: Set of parameters of the modified S–A turbulence model to represent the WT-ZMJ configurations with different periods of oscillation T_{osc}.

β	$U_{\text{jet,max}}$	T_{osc}	c_{v1}	c_{b1}	$c_{f,\text{RANS}}$	$c_{f,\text{DNS}}$	Diff. (%)
75	9	125	8.55	0.170	7.57	7.57	-0.01
75	10.8	125	8.52	0.160	7.53	7.53	-0.05
75	13.5	125	8.51	0.143	7.39	7.38	0.19
75	18	125	8.29	0.110	7.20	7.20	-0.01
75	21.6	125	8.03	0.097	7.18	7.18	0.10
75	24.3	125	7.50	0.080	7.25	7.24	0.11
75	27	125	7.00	0.068	7.31	7.32	-0.12
15	27	125	3.30	0.120	13.59	13.59	~ 0
30	27	125	4.65	0.099	10.79	10.77	0.15
45	27	125	5.50	0.070	8.82	8.81	0.11
60	27	125	5.94	0.057	7.86	7.84	0.23
70	27	125	6.50	0.059	7.42	7.43	-0.13
75	27	125	7.00	0.068	7.31	7.32	-0.12
75	27	62.5	9.12	0.105	6.59	6.59	-0.05
75	27	93.75	7.75	0.075	6.94	6.92	0.35
75	27	125	7.00	0.068	7.31	7.32	-0.12
75	27	187.5	7.20	0.073	7.31	7.30	0.03
75	27	250	7.69	0.085	7.24	7.25	-0.06

Table 5.3: Set of parameters for the simulation of the channel flow with WT-ZMJ using RANS. Friction coefficients are multiplied by 10^3.

5.4.4 Conclusion on turbulence model modification

An extensive set of parameters are obtained to model the jets with different settings in RANS with the modified S–A turbulence model. The idea is to predict new set of parameters without the need of running more simulations. For that, more set of parameters can be obtained and then interpolated to estimate the friction coefficient.

A base case without modification is required to be simulated in both DNS and RANS in order to apply this method. The reason is the mismatch of the smooth channel RANS simulations with DNS. The correction from the base case has to be identified in order to apply the modified turbulent model. Fortunately, the effects of shifting and twisting of the parameters are consistent at different Reynolds numbers.

This page has been intentionally left blank.

Chapter 6

Conclusions and Future work

In this thesis, the Wall Tangential Zero-Mass Jets have been studied in detail using the FIK-E. This active flow control system has been investigated in this thesis to better understand its potential benefits.

This short chapter contains an overall summary of the main points achieved and an outline of the future work to be followed to further investigate this technology.

6.1 Conclusions

The WT-ZMJ has been analysed in four different aspects, coinciding with the objectives of the thesis:

- When the jets were firstly analysed, the Reynolds stresses were found to increase. This contradicted the analysis of Fukagata et al. (2002), questioning the decrease of skin friction. The contributions of the skin friction are decomposed in chapter 3 by extending the FIK analysis to the FIK-E to find where the reduction comes from. The main actor that alleviates the increase of Reynolds stresses is the inhomogeneous contribution, which is related to the modification of the velocity field near the wall.

  The FIK-E, derived in chapter 3, is valid for other types of flows such as open boundary layer flows. The additional benefit of this formula is that flows can be analysed with respect to phase time and that the jet condition (or transpiration) can be applied.

- Different settings of the WT-ZMJ have been simulated in order to increase the reduction coming from this technology in chapter 4. Moreover, the FIK-E has been used to properly identify the contributions affected by different parameters. The results obtained with the FIK-E are accurate, with an average deviation from the traditional method of calculating the friction coefficient of 0.70%.

As the inhomogeneous contribution is the main source of skin friction reduction, there is an interest in modifying spanwise and streamwise velocities. A balance of these two magnitudes has to be reached with the firing direction of the jet, β. When β is around 60 deg, the inhomogeneous contribution is maximum. However, the Reynolds shear stress contribution is important at that stage and decreases the higher the β. It has been found that a β in the neighbourhood of 75 deg minimises the value of these two factors, obtaining a minimum in the skin friction coefficient.

Lower jet velocities lead to a less altered flow field, making both inhomogeneous and Reynolds shear stress contributions decrease. They do it at different rates, which makes the inhomogeneous contribution less effective the lower the velocity is. Fortunately, the action of the jet contribution has a maximum net benefit at $U^+_{\text{jet,max}} \approx 20$, where the blowing jet plume cannot establish as in the baseline case, providing a higher velocity gradient at the boundary, but it is strong enough to increase the velocity value at the exit of the jet.

These beneficial effects are related to flow field areas where the jet has the most influence in. Therefore, when the area where flow control cannot reach, i.e. the centre of the jet wall, is shorten, the skin friction coefficient is decreased drastically. Note that less area is covered by the devices and therefore, more devices have to be placed, increasing the input power. The findings show that the skin friction reduction overcomes the increase in input power, making it a viable option to consider in order to find a case where the saved power is positive.

On average, in the cases studied (excluding the $T_{osc} \to \infty$ case), the Reynolds stress contribution increases a 78% due to the action of the jets compared to the smooth channel flow. However, the inhomogeneous contribution reduces a 51% of the value of the total Reynolds shear stress contribution. Only due to the inhomogeneous contribution, the skin friction coefficient is reduced 1.21×10^{-3}, which is 14.75% of the original value without any flow control.

- A power balance study was applied to the cavity producing the jets to estimate the potential losses and power required by the WT-ZMJ in chapter 4. Most of the power introduced by the piston is transformed into internal energy due to dissipation. This accounts for 62% of the total. Since the flow inside the cavity is compressible, there is power lost due to this fact, but it is minimum. The air is either compressed or expanded when the piston is accelerating towards the centre position and therefore, power is lost. However, when the piston decelerates, after reaching the centre position, the compressed air has room to expand, transforming internal energy into mechanical energy. This translates to a power recovery that is very close to the one lost. The same happens with the air that expands.

- The WT-ZMJ can be modelled in RANS simulations using different sets of parameters in the S–A turbulence model. In chapter 5, this model has been extrapolated to different Reynolds numbers in an attempt to show the potential benefits of this technology.

6.2 Future work

More research in WT-ZMJ would be needed to increase the Technological Readiness Level of this technology. Some of the potential studies that can be performed are:

- The extension of the parameters studied in this thesis. Even though some of the most important configurations have been tried, there are many more that could potentially reduce the skin friction.
- Combinations of different parameters can be tested in order to build parameter maps and find a minimum skin friction value. Two or more parameters changes can be simulated in DNS and compared with the combination of c_{v1} and c_{b1} corresponding to that case.
- The effect of WT-ZMJ at higher Reynolds numbers. Even though a prediction has been explored in chapter 5 about the potential benefits of WT-ZMJ at high Reynolds numbers, the DNS verification should be obtained. It is challenging to increase the Reynolds number while obtaining accurate results, but a lot of insight could be gained from this sensitivity.
- A power balance in a three dimensional simulations with streamwise flow. The results from this thesis have been separated into a channel flow and a cavity flow due to computational limitations. However, the combination of these two flows could be of great interest to prove some of the assumptions made.

- A study to obtain the efficiencies of different chamber designs. Other options could reduce the power lost in the chamber due to dissipation.

- A similar mechanism to the streamwise travelling waves proposed by Quadrio et al. (2009a) can be investigated. The jets in this thesis are operating at the same velocity at all points in the x direction. Having a travelling wave along the streamwise direction could improve the capabilities of the WT-ZMJ.

- Open boundary layer simulations. The research on WT-ZMJ have been performed in a channel flow exclusively. It would be very interesting to observe the implications of using these devices in a growing boundary layer. One of the advantages of being a zero net mass device is that the boundary layer would not be increased.

  In order to simulate the open boundary layer, a similar procedure to that of the turbulent inflow generation method from Lund et al. (1998) could be investigated.

Bibliography

Abe, Y., Nonomura, T., and Fujii, K. (2015). Spatial growth of the spanwise disturbance induced by a synthetic jet on separation control over an airfoil. In *53rd AIAA Aerospace Sciences Meeting*, page 1057.

Agostini, L. and Leschziner, M. (2018). The impact of footprints of large-scale outer structures on the near-wall layer in the presence of drag-reducing spanwise wall motion. *Flow, Turbulence and Combustion*, 100(4):1037–1061.

Aljallis, E., Sarshar, M.A., Datla, R., Sikka, V., Jones, A., and Choi, C.-H. (2013). Experimental study of skin friction drag reduction on superhydrophobic flat plates in high reynolds number boundary layer flow. *Phys. Fluids*, 25(2):025103.

Allmaras, S.R., Johnson, F., and Spalart, P.R. (2012). Modifications and clarifications for the implementation of the Spalart-Allmaras turbulence model. In *Seventh International Conference on Computational Fluid Dynamics (ICCFD7)*, pages 1–11.

Amitay, M., Smith, D.R., Kibens, V., Parekh, D.E., and Glezer, A. (2001). Aerodynamic flow control over an unconventional airfoil using synthetic jet actuators. *AIAA J.*, 39(3):361–370.

Anderson, J.D. Jr. (2007). *Fundamentals of aerodynamics.* McGraw Hill, 4 edition.

Asada, H. and Kawai, S. (2017). High-order implicit discontinuous Galerkin scheme for unsteady turbulent flows. In *55th AIAA Aerospace Sciences Meeting*, page 0739.

Aupoix, B., Pailhas, G., and Houdeville, R. (2012). Towards a general strategy to model riblet effects. *AIAA J.*, 50(3):708–716.

Barlow, J. B., Rae Jr, W. H., and Pope, A. (2015). Low speed wind tunnel testing. *INCAS Bulletin*, 7(1):133.

Baron, A. and Quadrio, M. (1996). Turbulent drag reduction by spanwise wall oscillations. *Appl. Sc. Res.*, 55:311–326.

Bechert, D.W. and Bertenwerfer, M. (1989). The viscous flow on surfaces with longitudinal ribs. *J. Fluid Mech.*, 206:105–209.

Bechert, D.W., Bruse, M., Hage, W., and Meyer, R. (2000). Fluid mechanics of biological surfaces and their technological application. *Naturwissenschaften*, 87(4):157–171.

Bechert, D.W., Bruse, M., Hage, W., Van der Hoeven, J.G.T., and Hoppe, G. (1997). Experiments on drag-reducing surfaces and their optimization with an adjustable geometry. *J. Fluid Mech.*, 338:59–87.

Brachet, M.E. (1991). Direct simulation of three-dimensional turbulence in the Taylor-Green vortex. *Fluid Dyn. Res.*, 8(1-4):1–8.

Brachet, M.E., Meiron, D.I., Orszag, S.A., Nickel, B.G., Morf, R.H., and Frisch, U. (1983). Small-scale structure of the Taylor-Green vortex. *J. Fluid Mech.*, 130:411–452.

Bradshaw, P. and Pontikos, N. S. (1985). Measurements in the turbulent boundary layer on an 'infinite' swept wing. *J. Fluid Mech.*, 159:105–130.

Castonguay, P., Vincent, P., and Jameson, A. (2011). Application of high-order energy stable flux reconstruction schemes to the euler equations. In *49th AIAA Aerospace Sciences Meeting including the New Horizons Forum and Aerospace Exposition*, page 686.

Choi, H., Moin, P., and Kim, J. (1994). Active turbulence control for drag reduction in wall-bounded flows. *J. Fluid Mech.*, 262:75–110.

Choi, K-S. (2002). Near-wall structure of turbulent boundary layer with spanwise-wall oscillation. *Phys. Fluids*, 14(7):2530–2542.

Choi, K.-S., DeBisschop, J.R., and Clayton, B.R. (1998). Turbulent boundary-layer control by means of spanwise-wall oscillation. *AIAA J.*, 36(7):1157–1162.

Coe, D.J., Allen, M.G., Smith, B.L., and Glezer, A. (1995). Addressable micromachined jet arrays. In *Solid-State Sensors and Actuators, 1995 and Eurosensors IX.. Transducers' 95. The 8th International Conference on*, volume 2, pages 329–332. IEEE.

Daniello, R.J., Waterhouse, N.E., and Rothstein, J.P. (2009). Drag reduction in turbulent flows over superhydrophobic surfaces. *Phys. Fluids*, 21(085103).

Davidson, L. (2017). Fluid mechanics, turbulent flow and turbulence modeling. *Chalmers University of Technology, Goteborg, Sweden (Jan 2017).*

DeBonis, J. (2013). Solutions of the Taylor-Green vortex problem using high-resolution explicit finite difference methods. In *51st AIAA Aerospace Sciences Meeting including the New Horizons Forum and Aerospace Exposition*, page 382.

Drikakis, D., Fureby, C., Grinstein, F.F., and Youngs, D. (2007). Simulation of transition and turbulence decay in the Taylor-Green vortex. *J. Turb.*

Driver, D. and Hebbar, S. (1987). Experimental study of a three-dimensional, shear-driven, turbulent boundary layer. *AIAA J.*, 25(35).

Favre, A. (1983). Turbulence: Space-time statistical properties and behavior in supersonic flows. *Phys. Fluids*, 26(10):2851–2863.

Fukagata, K. (2004). Detailed derivation process of the FIK identity. *Private note.*

Fukagata, K., Iwamoto, K., and Kasagi, N. (2002). Contribution of Reynolds stress distribution to the skin friction in wall-bounded flows. *Phys. Fluids*, 14(11):73–76.

Fukagata, K. and Kasagi, N. (2003). Drag reduction in turbulent pipe flow with feedback control applied partially to wall. *Int. J. Heat Fluid Flow*, 24(4):480–490.

Gad-el Hak, M. (2000). *Flow control - Passive, Active and Reactive Flow Management.* Cambridge University Press.

Gao, H. and Wang, Z.J. (2013). A conservative correction procedure via reconstruction formulation with the chain-rule divergence evaluation. *J. Comp. Phys.*, 232(1):7–13.

Gersten, K. and Herwig, H. (1992). Strömungsmechanik. grundlagen der impuls. *Wärme-und Stoffübertragung aus asymptotischer Sicht*, 6.

Glezer, A. and Amitay, M. (2002). Synthetic jets. *Ann. Rev. Fluid Mech.*, 34(1):503–529.

Godunov, S.K. (1959). A difference method for numerical calculation of discontinuous solutions of the equations of hydrodynamics. *Matematicheskii Sbornik, translated US Joint Publ. Res. Service, JPRS 7226, 1969*, 89(3):271–306.

Hasegawa, Y., Quadrio, M., and Frohnapfel, B. (2014). Numerical simulation of turbulent duct flows with constant power input. *J. Fluid Mech.*, 750:191–209.

Henoch, C., Krupenkin, T. N., Kolodner, P., Taylor, J.A., Hodes, M.S., Lyons, A. M., Peguero, C., and Breuer, K. (2006). Turbulent drag reduction using superhydrophobic surfaces. *AIAA Paper*, 2006-3192.

Hinze, J.O. (1975). *Turbulence.* McGraw Hill, Inc. – Second Edition.

Hirsch, C. (2007). *Numerical computation of internal and external flows: The fundamentals of computational fluid dynamics.* Butterworth-Heinemann.

Iuso, G., Onorato, M., Spazzini, P.G., and di Cicca, G.M. (2002). Wall turbulence manipulation by large-scale streamwise vortices. *J. Fluid Mech.*, 473:23–58.

Jahanmiri, M. (2010). Active flow control: a review. Technical report, Chalmers University of Technology.

Jelly, TO, Jung, SY, and Zaki, TA (2014). Turbulence and skin friction modification in channel flow with streamwise-aligned superhydrophobic surface texture. *Phys. Fluids*, 26(9):095102.

Jeong, J. and Hussain, F. (1995). On the identification of a vortex. *J. Fluid Mech.*, 285:69–94.

Jung, W.J., Mangiavacchi, N., and Akhavan, R. (1992). Suppression of turbulence in wall-bounded flows by high-frequency spanwise oscillations. *Phys. Fluids A*, 4(8):1605–1607.

Kametani, Y. and Fukagata, K. (2011). Direct numerical simulation of spatially developing turbulent boundary layers with uniform blowing or suction. *J. Fluid Mech.*, 681(1):154–172.

Kim, J., Kim, K., and Sung, H.J. (2003). Wall pressure fluctuations in a turbulent boundary layer after blowing or suction. *AIAA J.*, 41(9):1697–1704.

Kim, J., Moin, P., and Moser, R. (1987). Turbulence statistics in fully developed channel flow at low Reynolds number. *J. Fluid Mech.*, 177:133–166.

Kim, K.H. and Kim, C. (2005). Accurate, efficient and monotonic numerical methods for multi-dimensional compressible flows: Part II: Multi-dimensional limiting process. *J. Comp. Phys.*, 208(2):570–615.

Kral, L., Donovan, J., Cain, A., and Cary, A. (1997). Numerical simulation of synthetic jet actuators. In *4th Shear Flow Control Conference*, page 1824.

Laadhari, F., Skandaji, L., and Morel, R. (1994). Turbulence reduction in a boundary layer by local spanwise oscillating surface. *Phys. Fluids*, 6(10):3218–3220.

Lardeau, S. and Leschziner, M.A. (2013). The streamwise drag-reduction response of a boundary layer subjected to a sudden imposition of transverse oscillatory wall motion. *Phys. Fluids*, 25:075109.

Lee, M. and Moser, R.D. (2015). Direct numerical simulation of turbulent channel flow up to $\mathrm{Re}_\tau \approx 5200$. *J. Fluid Mech.*, 774:395–415.

Lund, T.S., Wu, X., and Squires, K.D. (1998). Generation of turbulent inflow data for spatially-developing boundary layer simulations. *J. Comp. Phys.*, 140(2):233–258.

Mele, B. and Tognaccini, R. (2012). Numerical simulation of riblets on airfoils and wings. In *50th AIAA Aerospace Sciences Meeting Including the New Horizons Forum and Aerospace Exposition*, page 861.

Mele, B. and Tognaccini, R. (2016). Performance assessment of a Transonic wing-body configuration with riblets installed. *J. Aircraft*, 53(1):129–140.

Min, T. and Kim, J. (2004). Effects of hydrophobic surface on skin-friction drag. *Phys. Fluids*, 16(7):L55–L58.

Moin, P., Shih, T., Driver, D., and Mansour, N. (1990). Direct numerical simulation of a three-dimensional turbulent boundary layer. *Phys. Fluids A*, 2(1846).

Nakanishi, R., Mamori, H., and Fukagata, K. (2012). Relaminarization of turbulent channel flow using traveling wave-like wall deformation. *Int. J. Heat Fluid Flow*, 35:152–159.

Neeteson, N.J., Earl, T.A., Gomit, G., Jeon, Y.J., Chatelier, L., Rival, D.E., and David, L. (2016). Sensitivity Analysis of Lagrangian Finite Volume Method for Pressure Evaluation on 3D Experimental Data.

Peet, Y. and Sagaut, P. (2009). Theoretical prediction of turbulent skin friction on geometrically complex surfaces. *Phys. Fluids*, 21(10).

Pope, S.B. (2001). *Turbulent flows.* IOP Publishing.

Qin, N. and Xia, H. (2008). Detached eddy simulation of a synthetic jet for flow control. *Proceedings of the Institution of Mechanical Engineers, Part I: Journal of Systems and Control Engineering*, 222(5):373–380.

Quadrio, M. (2011). Drag reduction in turbulent boundary layers by in-plane wall motion. *Phil. Trans. Royal Soc. A*, 369(1940):1428–1442.

Quadrio, M., Auteri, F., Baron, A., Belan, M., and Bertolucci, A. (2009a). Experimental assessment of turbulent drag reduction by wall traveling waves. *XII EUROMECH European Turbulence Conference, Marburg (D), Sept. 7-10.*

Quadrio, M. and Ricco, P. (2003). Initial response of a turbulent channel flow to spanwise oscillation of the walls. *J. Turbul.*, 4 007.

Quadrio, M. and Ricco, P. (2004). Critical assessment of turbulent drag reduction through spanwise wall oscillations. *J. Fluid Mech.*, 521:251–271.

Quadrio, M. and Ricco, P. (2011). The laminar generalized Stokes layer and turbulent drag reduction. *J. Fluid Mech.*, 667:135–157.

Quadrio, M., Ricco, P., and Viotti, C. (2009b). Streamwise-travelling waves of spanwise wall velocity for turbulent drag reduction. *J. Fluid Mech.*, 627:161–178.

Rastegari, A. and Akhavan, R. (2015). On the mechanism of turbulent drag reduction with super-hydrophobic surfaces. *J. Fluid Mech.*, 773:R4.

Ricco, P. (2004). Modification of near-wall turbulence due to spanwise wall oscillations. *J. Turbul.*, 5 024.

Ricco, P. (2011). Laminar streaks with spanwise wall forcing. *Phys. Fluids*, 23(6):064103.

Ricco, P. and Hahn, S. (2013). Turbulent drag reduction through rotating discs. *J. Fluid Mech.*, 722:267–290.

Ricco, P., Ottonelli, C., Hasegawa, Y., and Quadrio, M. (2012). Changes in turbulent dissipation in a channel flow with oscillating walls. *J. Fluid Mech.*, 700:77–104.

Ricco, P. and Quadrio, M. (2008). Wall-oscillation conditions for drag reduction in turbulent channel flow. *Int. J. Heat Fluid Flow*, 29:601–612.

Rizzetta, D.P., Visbal, M.R., and Stanek, M.J. (1999). Numerical investigation of synthetic-jet flowfields. *AIAA J.*, 37(8):919–927.

Roe, P.L. (1981). Approximate Riemann solvers, parameter vectors, and difference schemes. *J. Comp. Phys.*, 43(2):357–372.

Roskam, Jan and Lan, Chuan-Tau Edward (1997). *Airplane aerodynamics and performance.* DARcorporation.

Sagaut, P., Deck, S., and Terracol, M. (2006). *Multiscale and Multiresolution Approaches in Turbulence. 2006.* Imperial College Press.

Sahlin, A. and Johansson, A. V. (1991). Design of guide vanes for minimizing the pressure loss in sharp bends. *Physics of Fluids A: Fluid Dynamics*, 3(8):1934–1940.

Sansone, M., Nguyen, L.D., Golubev, V.V., and Mankbadi, R.R. (2016). A numerical study of synthetic-jet actuation effect on airfoil trailing edge noise. In *22nd AIAA/CEAS Aeroacoustics Conference*, page 2918.

Saravi, S. and Cheng, K. (2013). A review of drag reduction by riblets and micro-textures in the turbulent boundary layers. *Europ. Sc. J.*, 9(33).

Schlichting, H. (1979). *Boundary-layer theory.* McGraw Hill.Inc.

Skote, M. (2011). Turbulent boundary layer flow subject to streamwise oscillation of spanwise wall-velocity. *Phys. Fluids*, 23:081703.

Smith, B.L. and Glezer, A. (1998). The formation and evolution of synthetic jets. *Phys. Fluids*, 10(9):2281–2297.

Spalart, P.R. and Allmaras, S.R. (1992). A one equation turbulence model for aerodinamic flows. *AIAA J.*, 94.

Spinosa, E. and Zhong, S. (2017). Reduction of skin friction drag in a turbulent boundary layer using circular synthetic jets. In *55th AIAA Aerospace Sciences Meeting*, page 0324.

Sumitani, Y. and Kasagi, N. (1995). Direct numerical simulation of turbulent transport with uniform wall injection and suction. *AIAA J.*, 33(7):1220–1228.

Taylor, G.I. and Green, A.E. (1937). Mechanism of the production of small eddies from large ones. *Proceedings of the Royal Society of London. Series A, Mathematical and Physical Sciences*, 158(895):499–521.

Tennekes, H. and Lumley, J.L. (1972). *A first course in turbulence*. MIT press.

Toro, E.F. (2013). *Riemann solvers and numerical methods for fluid dynamics: a practical introduction*. Springer Science & Business Media.

Wang, Z.J., Fidkowski, K., Abgrall, R., Bassi, F., Caraeni, D., Cary, A., Deconinck, H., Hartmann, R., Hillewaert, K., Huynh, H.T., et al. (2013). High-order CFD methods: current status and perspective. *Int. J. Num. Meth. Fluids*, 72(8):811–845.

Weiss, J.M. and Smith, W.A. (1995). Preconditioning applied to variable and constant density flows. *AIAA J.*, 33(11):2050–2057.

Wilcox, D.C. et al. (1998). *Turbulence modeling for CFD*, volume 2. DCW industries La Canada, CA.

Williams, D.M. and Jameson, A. (2013). Nodal points and the nonlinear stability of high-order methods for unsteady flow problems on tetrahedral meshes. In *21st AIAA Computational Fluid Dynamics Conference*, page 2830.

Wise, D.J., Alvarenga, C., and Ricco, P. (2014). Spinning out of control: Wall turbulence over rotating discs. *Phys. Fluids*, 26(12):125107.

Wise, D. J. and Ricco, P. (2014). Turbulent drag reduction through oscillating discs. *J. Fluid Mech.*, 746:536–564.

Witherden, F.D., Farrington, A.M., and Vincent, P. (2014). PyFR: An open source framework for solving advection-diffusion type problems on streaming architectures using the flux reconstruction approach. *Comp. Phys. Comm.*, 185(11):3028–3040.

Xia, H. and Qin, N. (2005). Dynamic grid and unsteady boundary conditions for synthetic jets flow. In *43rd AIAA Aerospace Sciences Meeting and Exhibit*, page 106.

Xie, F. (2019). *Zero mass jets for turbulent flow drag reduction*. PhD thesis, University of Sheffield.

Yao, J., Chen, X., and Hussain, F. (2018). Drag control in wall-bounded turbulent flows via spanwise opposed wall-jet forcing. *J. Fluid Mech.*, 852:678–709.

This page has been intentionally left blank.

Appendix A

Mesh sensitivity for ZMJ

The investigation of a β angle that produced a positive skin friction reduction was originally done with a coarser mesh. The mesh information of this coarse mesh is gathered in table A.1.

Parameter	Value	Parameter	Value	Parameter	Value
L_x	$4\pi h$	n_x	128	Δx^+	17.67
L_y	$2h$	n_y	149	Δy^+	$0.2 \sim 7.02$
L_z	$\frac{4}{3}\pi h$	n_z	84	Δz^+	8.98

Table A.1: Coarse mesh parameters

The sweep of β that this mesh gives is presented in figure A.1.

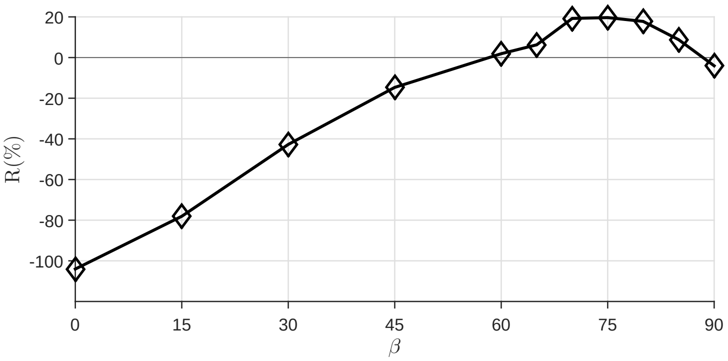

Figure A.1: Original sensitivity of reduction of c_f to changes in β.

The maximum skin friction reduction given by this mesh is at $\beta = 75\,\text{deg}$ with a value of $R(\%) = 19.7\%$. Mesh sensitivities of this case and the one at $\beta = 0$ were done with the meshes of table A.2 and the results can be seen in figure A.2.

Mesh	Δx^+	Δy^+	Δz^+	n_x	n_y	n_z	c_f at $\beta = 0$ $(\times 10^3)$	c_f at $\beta = 75\,\text{deg}$ $(\times 10^3)$
1	17.67	$0.2 \sim 7.02$	8.98	128	149	84	16.68	6.57
2	8.84	$0.2 \sim 4.09$	4.49	256	217	168	16.46	6.92
3	8.84	$0.2 \sim 4.09$	$1.0 \sim 4.49$	128	217	396	16.32	7.18
4	8.84	$0.2 \sim 4.09$	$0.5 \sim 3.80$	128	217	504	16.23	7.32
5	8.84	$0.2 \sim 4.09$	$0.2 \sim 3.97$	128	217	648	16.23	7.34

Table A.2: Coarse mesh parameters

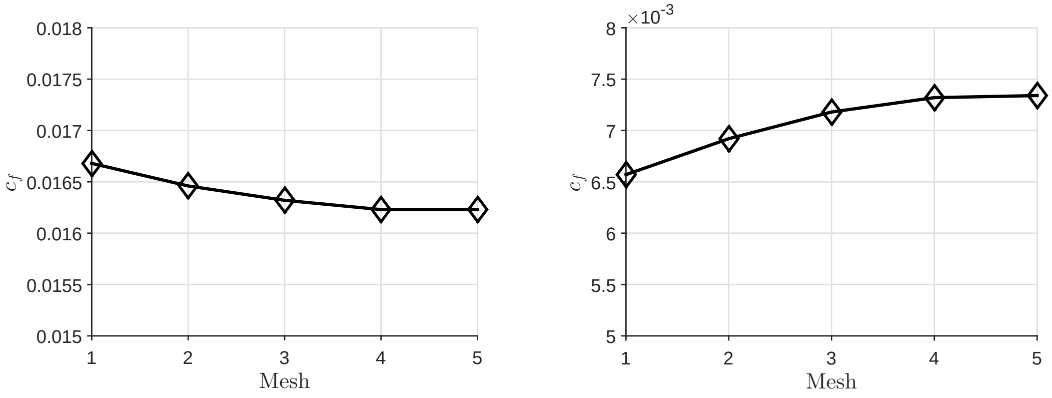

(a)

(b)

Figure A.2: Friction coefficient of the different meshes of table A.2 at $\beta = 0$ in (a) and $\beta = 75\,\text{deg}$ in (b).

According to the results, mesh 4 is enough to reproduce the channel flow with WT-ZMJ and it is the one used for this thesis.

Appendix B

Proof of concept for the turbulence model in a practical case

The turbulence model would be applied to the flow over a fuselage to predict the potential benefits of ZMJ. This is a proof of concept and caution must be taken, as this is a large extrapolation in terms of Reynolds number from the channel flow case to a flow over a fuselage.

As the jets are operating tangential to the wall and not adding mass to the system, the boundary layer thickness should not increase significantly. One of the main objectives of this proof of concept is to prove that this is the case for this active flow control system. The boundary layer thickness has an impact on pressure drag, as the effective area of the fuselage increases the bigger it is.

B.1 Practical application

A proof of concept of the results of table 5.3 is applied in a practical example in this section. It is intended to show the potential of this methodology to replicate flow control in larger scales and the benefits from the WT-ZMJ, provided its validity at big scales.

B.1.1 Baseline fuselage/ZMJ off

As part of the project DRAGY, a fuselage geometry was given to different partners to create a mesh and test the flow control devices on. It is an axisymmetric fuselage with no wings in order to show benefits mainly in the skin friction forces. The measurements are shown in

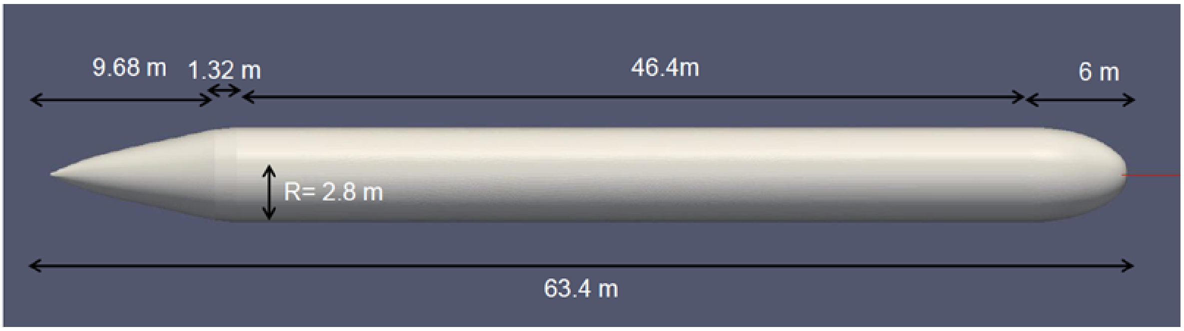

Figure B.1: Geometry of the fuselage with measurements.

figure B.1.

The flight conditions were specified by Airbus Group Innovations (AGI) in the project. The fuselage is in cruise altitude at 38 000 ft (11 582.4 m) flying at Mach number $M = 0.85$ and angle of attack of $\alpha = 2\,\mathrm{deg}$.

Using the International Standard Atmosphere (ISA), the stratosphere equations are used to obtain the conditions at that altitude:

$$T^* = T^*_{\mathrm{tpp}} = 1 + \frac{6.5 \times 10^{-3}\mathrm{K/m}}{T^*_0} h^*_{\mathrm{tpp}} T^*_0 \tag{B.1}$$

$$p^* = \frac{T^*_{\mathrm{tpp}}}{T^*_0} e^{g^* \frac{h-11000}{R^*_g T^*_{\mathrm{tpp}}}} p^*_0 \tag{B.2}$$

$$\rho^* = \frac{p^*}{p^*_0} / \frac{T^*}{T^*_0} \rho^*_0 \tag{B.3}$$

where $T^*_0 = 288.16\mathrm{K}$, $p^*_0 = 101325\mathrm{Pa}$ and $\rho^*_0 = 1.225\mathrm{kg/m}^3$ are the standard temperature, pressure and density at sea level, the subscript ttp denotes quantities at the tropopause, h^* is altitude in metres, $g^* = -9.81\mathrm{m/s}^2$ is gravity at standard sea level and $R^*_g = 287.04\mathrm{J/(kgK)}$ is the gas constant for air.

A multi-block structured mesh was generated using Pointwise with 5 980 608 cells as seen in figure B.2. This is the chosen mesh after the mesh sensitivity (Appendix C).

A symmetry boundary condition is set in the plane where the model of the half fuselage is. The boundary conditions at the inlet and far field are inflow conditions at $u^* = 250.66\mathrm{m/s}$, $v^* = 8.75\mathrm{m/s}$, $w = 0$, $p^* = 20645\mathrm{Pa}$ and $T^* = 216.7\mathrm{K}$ and the outlet conditions are set to a zero gauge pressure. The first cell height is ensured to be $y^+ < 1$ in order for S–A turbulence

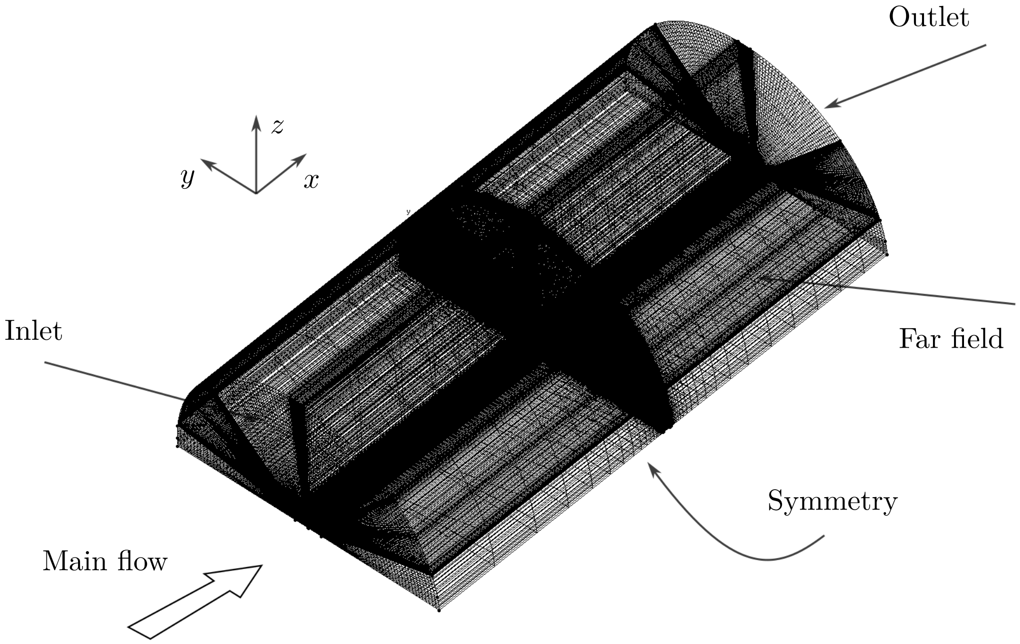

Figure B.2: Mesh overview.

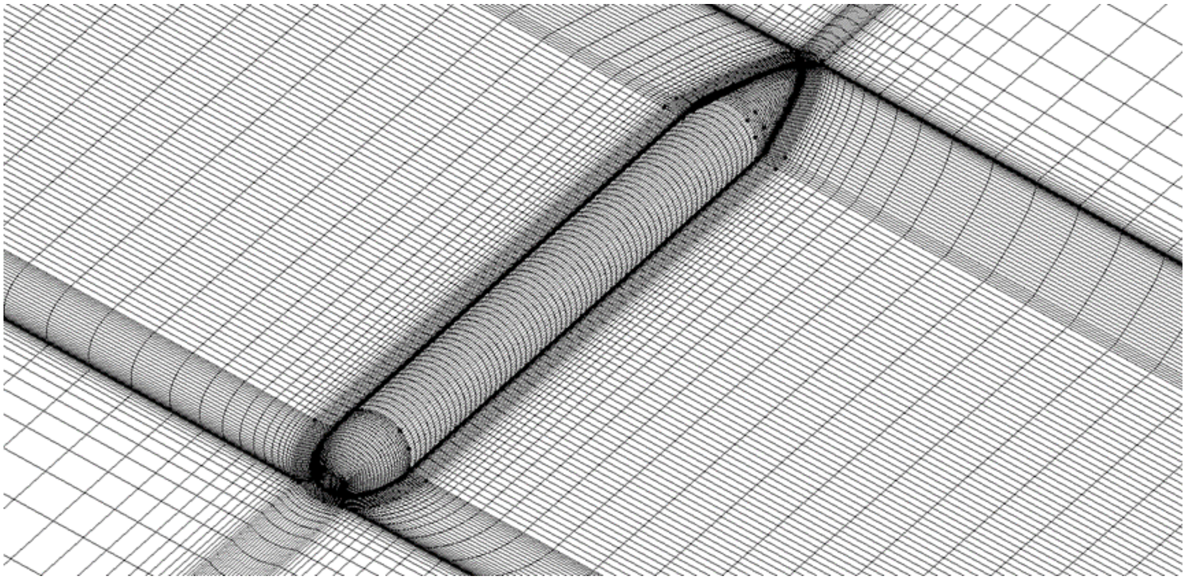

Figure B.3: Zoom of the fuselage mesh.

Friction drag (counts)	Pressure drag (counts)	Total drag (counts)	Friction drag (% of total)	Pressure drag (% of total)
16.42	6.26	22.68	72.4	27.6

Table B.1: Drag values expressed in drag counts (1 count = 10^{-4}).

model to be valid. The original parameters of the S–A turbulence model are used. A zoomed view of the fuselage mesh distribution and symmetry plane is shown in figure B.3.

The flow field around the fuselage is plotted in figure B.4 and the local skin friction coefficient in figure B.5. Two shock waves are identified near the junctions between the nose and cylinder, and the tail and cylinder. Since the fuselage is flying at an angle of attack of $\alpha = 2\,\text{deg}$, the flow is not symmetric with respect to y and the shock waves have different intensity at the nose and tail. It is specially appreciated at the windward side of the tail, where the shock wave is noticeably stronger and the local friction coefficient is the highest due to its high local velocity.

The results of skin friction and pressure forces in the direction of the flow is gathered in table B.1. Forces are scaled with $\frac{1}{2}\rho^* \boldsymbol{v}^{*2} S$ where $S = 512.38\text{m}^2$ is the area of the half fuselage.

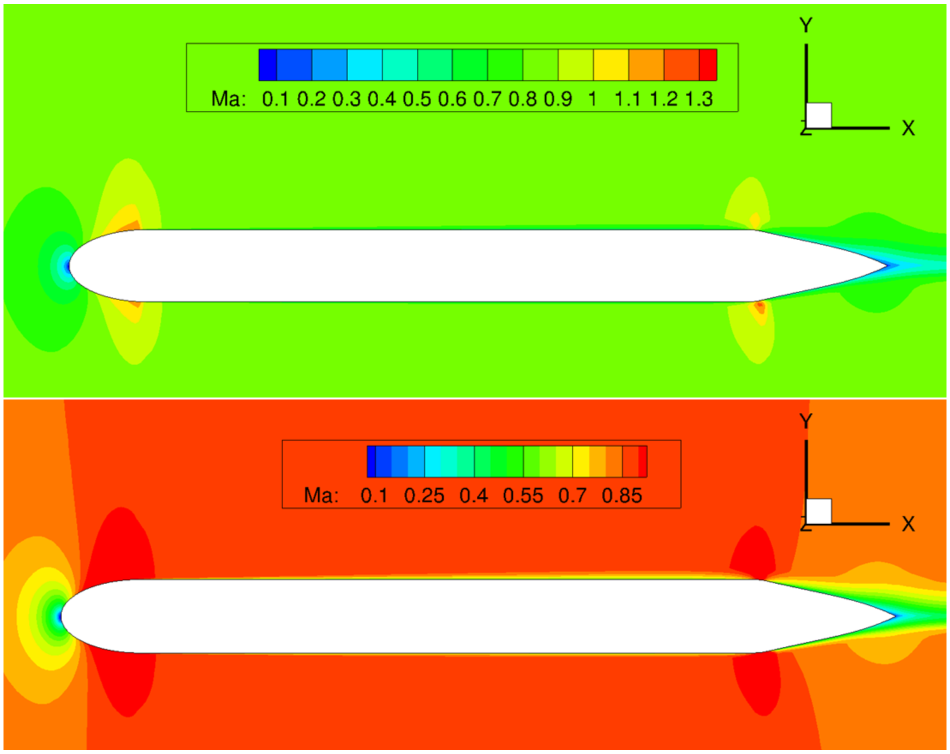

Figure B.4: Flow field around the fuselage at the symmetry plane showing the Mach number. Bottom figure shows the Mach number up to 0.9 in order to better show the boundary layer.

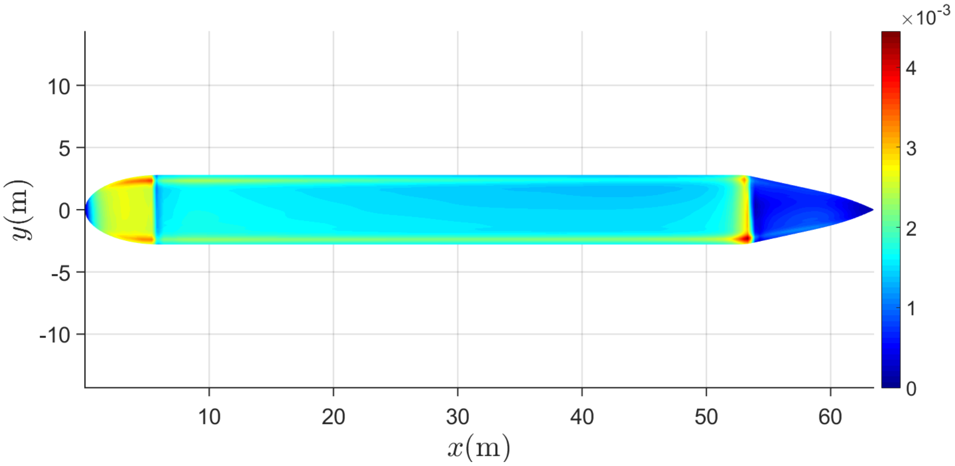

Figure B.5: Contour of skin friction of the fuselage.

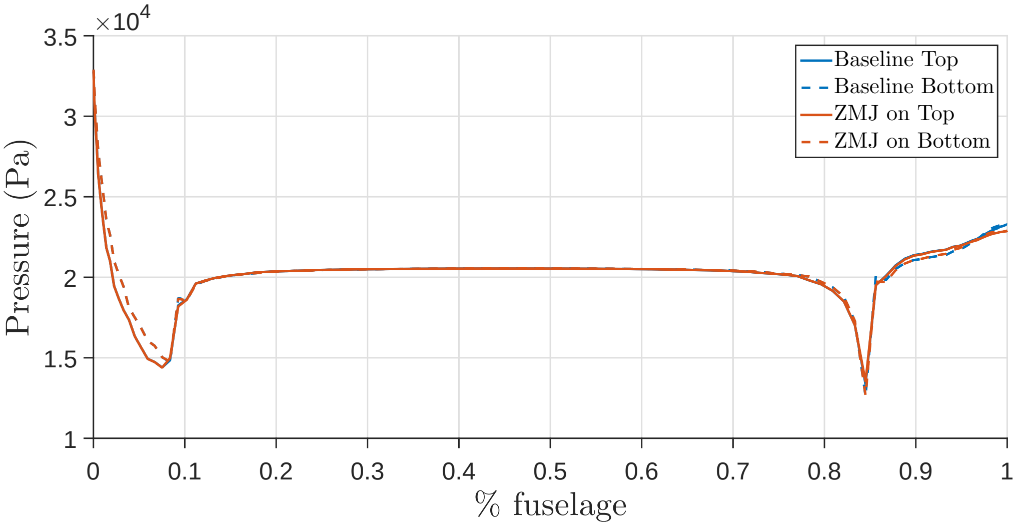

Figure B.6: Pressure distribution over the fuselage with and without control using S-A turbulence model modifications.

B.1.2 Application of the WT-ZMJ to the fuselage

The modifications of the S–A turbulence model from section 5.3 and 5.4 are applied in this section. The set of parameters from the baseline case of the WT-ZMJ are $(c_{\mathrm{v1}}, c_{\mathrm{b1}}) = (7.00, 0.068)$.

The pressure around the fuselage changes slightly due to flow control as shown in figure B.6, having the most impact around the tail area after the expansion wave. This contribution increases 0.08 drag counts from 6.26 to 6.34.

The most noticeable change comes from the skin friction drag shown in figure B.7, which is decreased from 16.42 to 14.25 counts. It shows that the skin fiction is decreased everywhere on the fuselage in various degrees. The skin friction is reduced most significantly in the areas on the upper side of the nose and the lower side of the tail of the fuselage.

From figure B.7 one could conclude that jets can be more effectively deployed in the regions of high skin friction areas. The skin friction along the x direction is plotted in figure B.8. It can be seen that the ZMJ effect throughout the entire fuselage except for the zones where the shock waves appear near the junctions between the nose and cylinder, and the cylinder and the tail.

With friction and pressure taken into consideration, the net reduction of drag counts is 2.09, although if only skin friction is taken into account, the reduction increases to 2.16 drag

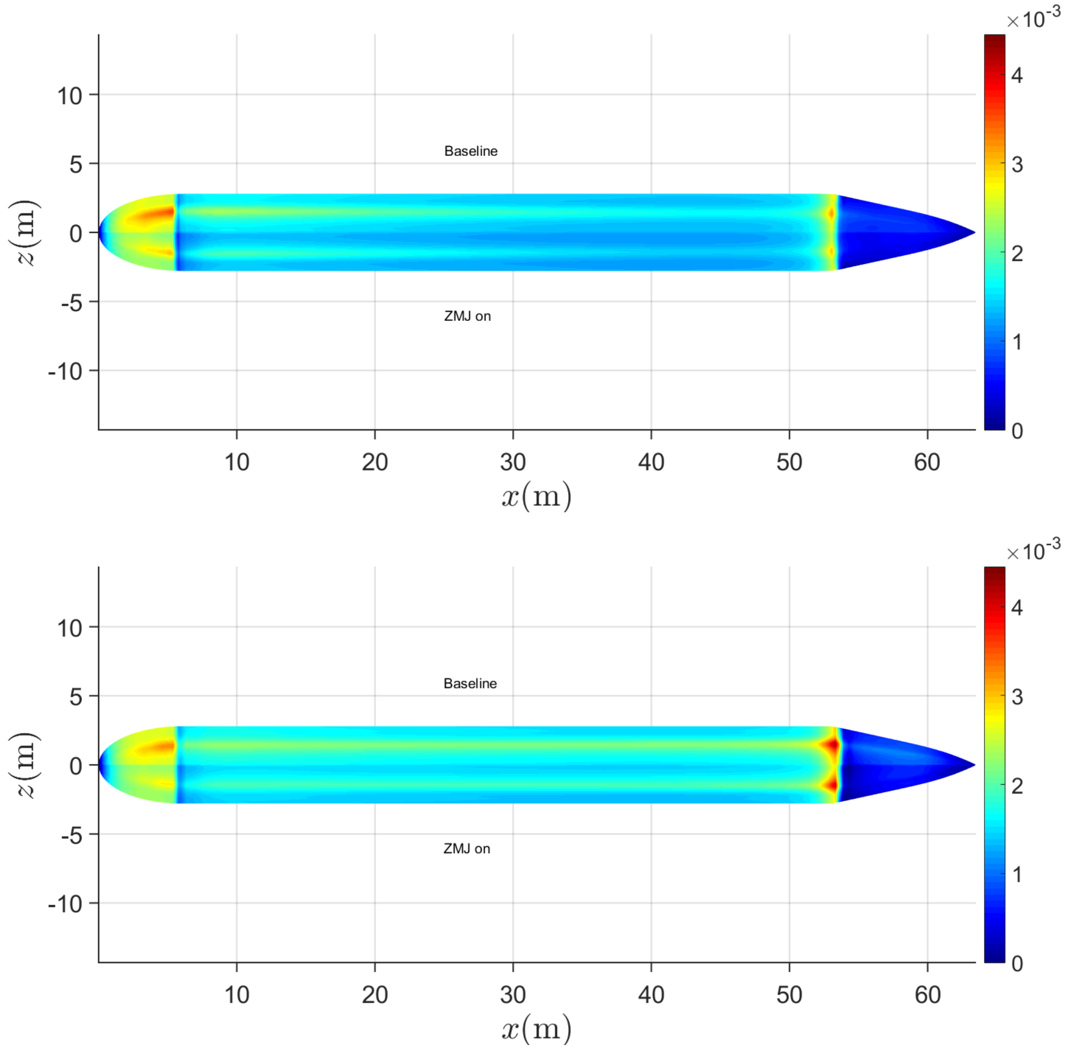

Figure B.7: Local skin friction coefficient on the fuselage from original S-A turbulence model (baseline) and modified S-A turbulence model (ZMJ on). Top figure corresponds to the leeward side of the fuselage and bottom figure to the windward side.

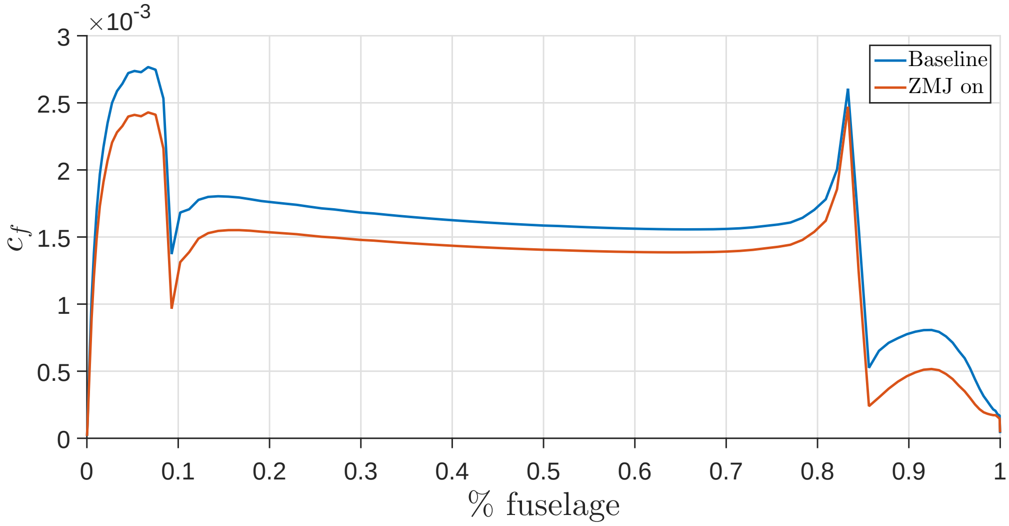

Figure B.8: Circumferentially integrated skin friction along the fuselage.

counts. This is a decrease of 13.2% of the original skin friction.

B.1.2.1 Boundary layer study

One of the desired features of the WT-ZMJ is that the boundary layer is not increased. As the turbulence model simulates the potential effects of the jets in the fuselage flow, the boundary layer can be assessed at different stations of the fuselage. The velocity profile of the leeward side of the fuselage with the jets off and on are shown in figure B.9 for two different stations.

Since the most noticeable modification from the baseline case is the decrease of c_{b1}, the slope of the end of the logarithmic region is twisted counter-clockwise. This fact is in agreement with the findings of section 5.3.1, as the Reynolds number based on the boundary layer (which is around $h^* \sim 0.5$ m at 30 m from the nose) of the fuselage is $Re = 10^6$. The effect of c_{v1} is also appreciated as the logarithmic region shifts downwards slightly. The boundary layer does not grow due to the ZMJ according to figure B.9, in fact it reduces, as the surrounding velocity is reached sooner than the baseline case. This fact can also be seen in figure B.10 with the cross section of two different stations.

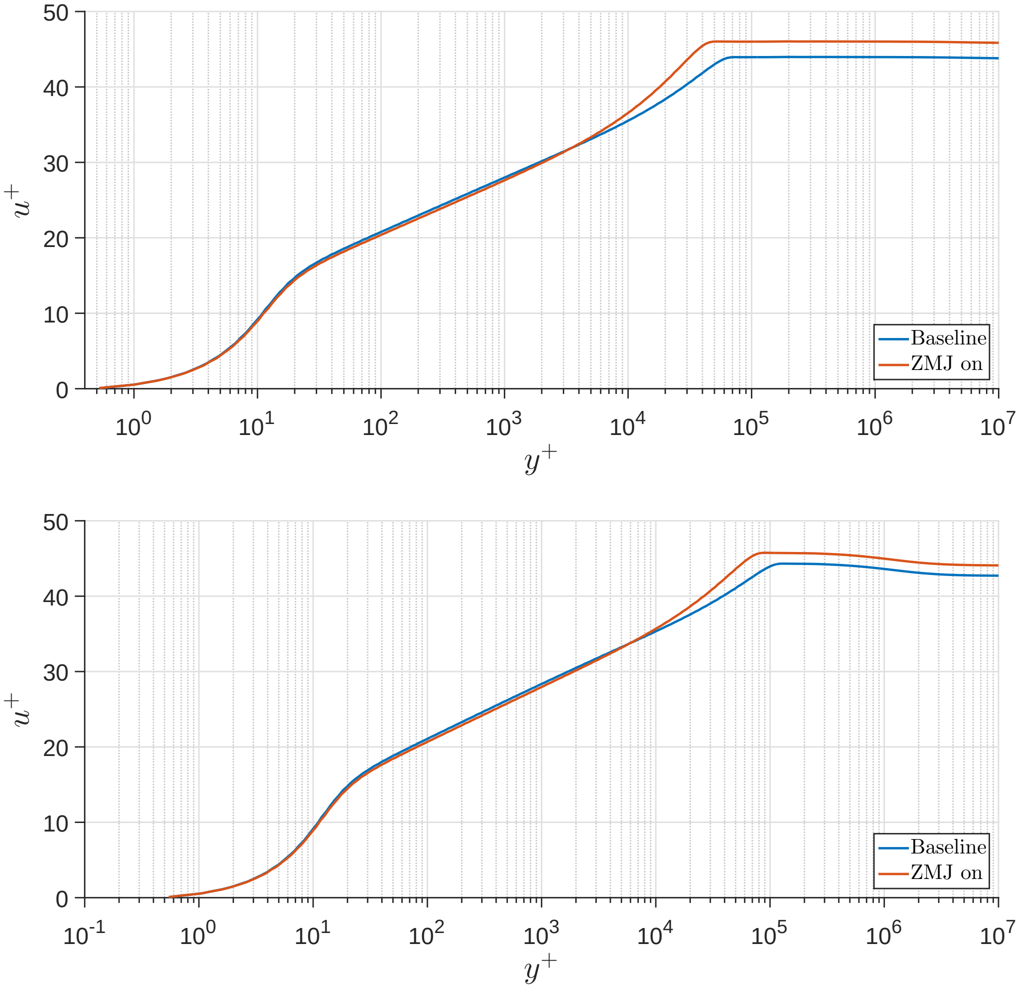

Figure B.9: Velocity profiles at 30m (top) and 50m (bottom) from the nose of the fuselage.

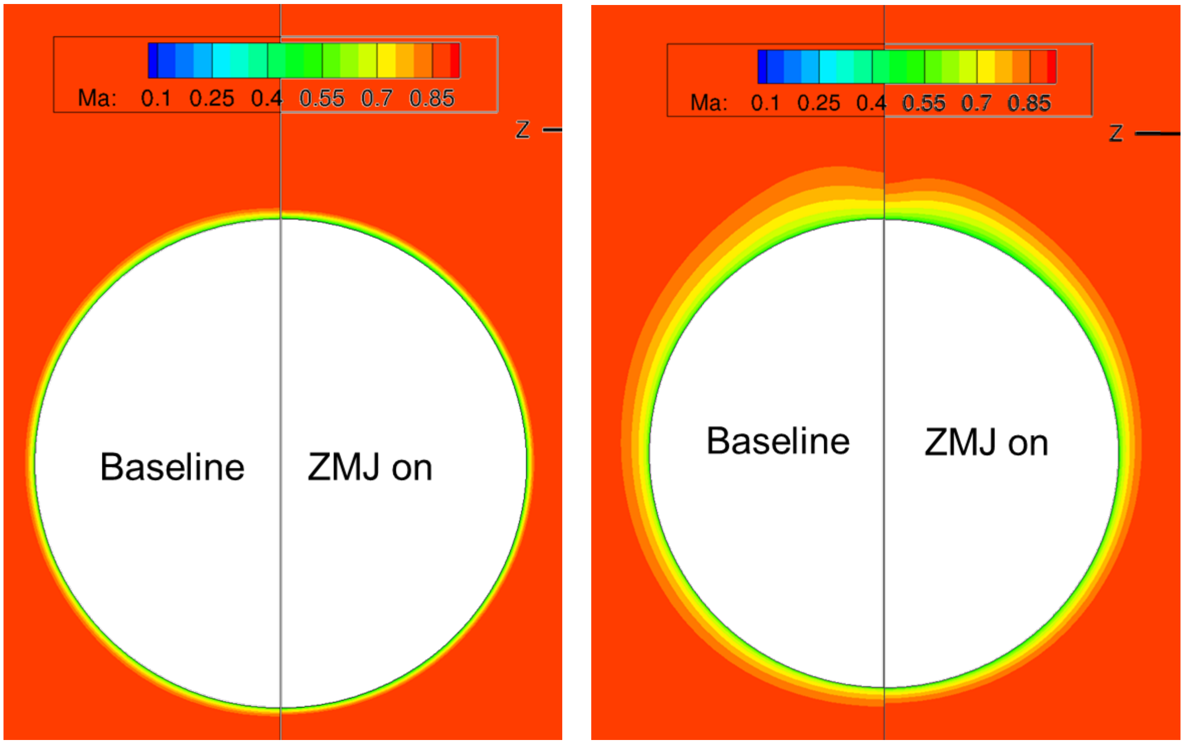

(a) 10 m from the nose.

(b) 50 m from the nose.

Figure B.10: Mach number contours of two stations of the fuselage.

B.2 Conclusions

This method shows the potential drag reduction by implementing the WT-ZMJ in the S–A model based on DNS data from the channel flow study.

Even though most of the skin friction reduction comes from the body of the fuselage as expected, calculations show that the skin friction is reduced significantly on the nose and tail of the fuselage as well.

The negative effect on the pressure drag is small due to the zero-mass and tangential features of the jets, limiting the increase of the boundary layer thickness along the fuselage.

One of the advantages of the WT-ZMJ lays on the zero net mass nature of the device. As it is not introducing mass to the system, the boundary layer does not grow. This is consistent with the results when the modified turbulence model is applied to the flow over a fuselage.

Appendix C

Fuselage mesh sensitivity

The sensitivity of the mesh of the flow around the fuselage is presented here. The conditions used are the same as reported in section B.1.1. The value of $y^+ < 1$ in all simulations and the grid points around the fuselage are varied. The results are gathered in table C.1. Forces are scaled with $\frac{1}{2}\rho^* \boldsymbol{v}^{*2} S$ where $S = 512.38\text{m}^2$ is the area of the half fuselage.

Mesh	Cells	Friction drag (counts)	Pressure drag (counts)	Total drag (counts)	% change
1	3 243 647	16.33	6.47	22.80	-
2	4 608 137	16.37	6.22	22.59	-0.93
3	5 980 608	16.42	6.26	22.68	+0.39
4	8 019 362	16.45	6.25	22.70	+0.08

Table C.1: Fuselage mesh parameters

The most sensitive value is the pressure drag for these simulations, as the skin friction drag is very similar in all meshes. The mesh number 3 is the one used in this thesis since the change percentage is less than 0.1%.